



# **Impact of stellar variability on the observational appearance of protoplanetary disks**

**MASTER THESIS**

in fulfillment of the requirements for the degree of

**Master of Science**

in Computational Science and Engineering with Physics  
submitted to the Faculty of Computer Science and Electrical Engineering,  
University of Rostock

Author: Alexandra Botnariuc

Advisor: Prof. Dr. S. Wolf, CAU Kiel

Co-advisor: Prof. Dr. R. Redmer, Universität Rostock

Rostock, 11 February 2019



# Abstract

A great number of young T Tauri type stars are surrounded by a flared, rotating disk of dense dust. The dust typically reaches temperatures of 300 – 1 500K in the close proximity of the star, and emits radiation in the near-infrared and mid-infrared regions.

The purpose of this thesis is to investigate how the changes in luminosity of the central star influence the observational appearance of the protoplanetary disks surrounding the star. Such faint, distant objects can only be observed in the K, L and N-bands with astronomical interferometers. The information extracted from the obtained interference pattern is contained in the *visibility*.

In order to achieve the stated purpose, the temperature, radius and luminosity of the central star and parameters of the circumstellar disk are varied. For each combination of parameters a radiative transfer simulation is run using the program *mol3d* to obtain the temperature distribution of the star and dust. From the temperature distribution, the total brightness distribution of the object for a certain wavelength is calculated, and the theoretical visibility measured by an astronomic interferometer is computed for that particular distribution. Finally, a variation in the observations of the visibility of the stellar object DR Tau is attempted to be fitted through luminosity variation.

It is found that stellar variability in the luminosity values investigated can cause changes in visibility of up to 48.1%. This variation can be observed with the existent instruments (VLTI/MATISSE), but its observability is highly dependent on the geometry of the object, in relation to the baseline and wavelength at which it is being observed. The variability of DR Tau could be explained by a change in luminosity, but no model could be fitted accurately for the original data.



# Contents

<b>1. Introduction</b>	<b>1</b>
<b>2. Theoretical basis</b>	<b>3</b>
2.1. Star Formation . . . . .	3
2.1.1. Star forming regions . . . . .	3
2.1.2. Star formation phases . . . . .	5
2.2. Radiation . . . . .	6
2.2.1. Absorption, emission and scattering . . . . .	7
2.2.2. Blackbody radiation . . . . .	8
2.2.3. Radiative Transfer . . . . .	10
2.3. Stellar properties . . . . .	14
2.3.1. Effective Temperature $T_e$ [K] . . . . .	14
2.3.2. Luminosity $L_*$ [ $L_\odot$ ] . . . . .	14
2.3.3. Stellar Mass $M_*$ [ $M_\odot$ ] . . . . .	15
2.3.4. T Tauri stars . . . . .	16
2.3.5. Variable Stars . . . . .	18
2.4. Circumstellar Disks . . . . .	19
2.4.1. Disk Model . . . . .	21
2.4.2. Interstellar Dust . . . . .	23
<b>3. Visibility</b>	<b>26</b>
3.1. Observations . . . . .	26
3.1.1. Long-baseline interferometry . . . . .	27
3.1.2. Van Cittert-Zernike Theorem . . . . .	30
3.1.3. Instruments . . . . .	32
3.2. Method . . . . .	35
3.3. Results . . . . .	37
3.3.1. Parameter space . . . . .	39
3.3.2. $R_{\text{in}}$ variation . . . . .	41

3.3.3. Temperature variation . . . . .	42
3.3.4. Temperature and luminosity variation . . . . .	45
3.3.5. Luminosity variation . . . . .	48
3.3.6. Near Infrared . . . . .	51
<b>4. DR Tau</b>	<b>53</b>
4.1. Introduction . . . . .	53
4.2. Data . . . . .	55
4.3. Model . . . . .	56
4.4. Results . . . . .	57
4.5. Discussion . . . . .	58
<b>5. Conclusion</b>	<b>59</b>
<b>A. Data and constants</b>	<b>61</b>
<b>B. Algorithm</b>	<b>64</b>
B.1. Code . . . . .	66
<b>C. Theoretical Suppliment</b>	<b>69</b>
C.1. Stellar Spectra . . . . .	69
C.2. T Tauri classification . . . . .	70
C.3. HR Diagram . . . . .	71
C.4. Variabile stars . . . . .	73
<b>Bibliography</b>	<b>77</b>

# Chapter 1.

## Introduction

*“The imagination of nature is far, far greater than the imagination of man”*

— Richard Feynman, *The Values of Science*, 1955

The Universe contains the entirety of space, time, matter, and energy. Its vastness lies beyond human comprehension.

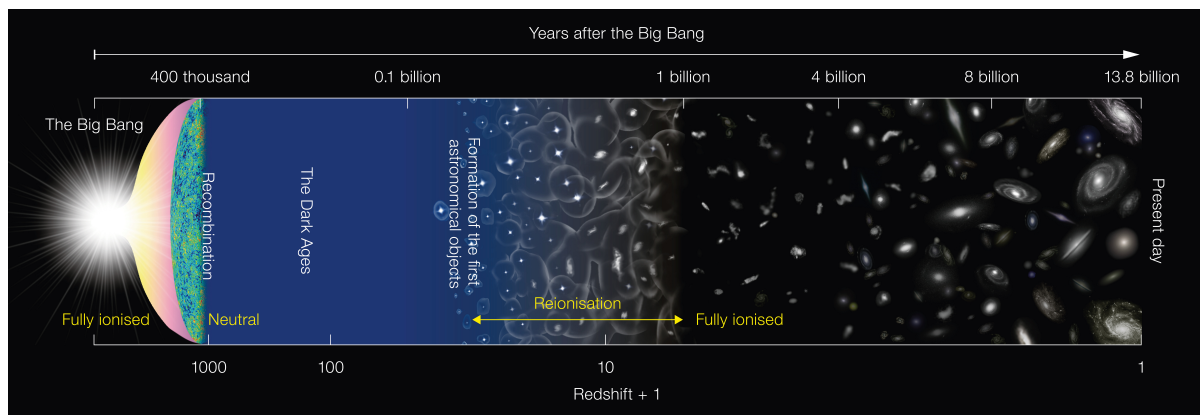


**Figure 1.1.:** Depiction of the evolution of the Universe according to the Big Bang theory over approximately 13.8 billion years, from the beginning to the present. This image is not to scale. **Credit:** ESO/NAOJ (<https://www.eso.org/public/images/eso1620a/>)

In the generally accepted Big Bang Theory (Figure 1.1), the early Universe could be described as an intensely hot plasma, in which particles could not form atoms. As space expanded, and the temperatures dropped, in approximately 300 000 years after the "birth" of the Universe, mostly hydrogen ( 76%) and helium ( 24%) atoms with

traces of lithium and deuterium formed. The remnant of the radiation emitted as the Universe became transparent, at about 3 000 K, is commonly called the Cosmic Microwave Background or CMB – it shows the wavelength dependence of a "blackbody" radiator at about 2.7 Kelvin [13]. In the next period, known as the Dark Ages, the Universe was filled with gas atoms, but there was no starlight. Over the course of hundreds of millions of years (100 – 300 Myr), the Universe continued to expand and cool, until gravity drove matter to collapse into clusters, stars and galaxies. This is the beginning of the current era of the Universe, called the Stellar Epoch.

The first stars that formed, were made of hydrogen and helium and were probably very large and very hot, possibly ending in hypernovae or even black holes. During their existence the stars have fused new elements: carbon, oxygen, silicon and iron. During their violent deaths heavier elements such as barium or lead were formed. The process of cosmos enrichment with new elements continued with the subsequent star generations. Nevertheless, the abundance of elements other than hydrogen and helium is less than 2%.

The low incidence of the elements essential for life is quite astonishing, even if the only life form known to man so far is the one on Earth. Given the size and variety in the Universe, the possibilities that other civilizations exist should be greater than null. One can calculate the number of civilisations in our Galaxy, with whom it would potentially be possible to communicate, to be as high as 900 [40].

It is therefore, if not interesting, at least important to study young solar systems with planet forming conditions in order to better understand nature and the origin of life. The first challenge is the size of the Universe, especially in the context of observations, and the investigation of this thesis is limited to a tiny piece of the universal puzzle, that of the influence of the variability of the central star on the observation of planet forming regions surrounding stars.

# Chapter 2.

## Theoretical basis

### 2.1. Star Formation

#### 2.1.1. Star forming regions

A great part of the matter in the universe exists in the form of rarefied (low-density) gas in galaxies and around them. The gas is mostly composed of hydrogen and helium atoms, mixed with other chemical elements and dust. Inside the galaxies the gas and dust form the *Interstellar Medium* or ISM. In terms of the baryonic mass, 99% of the ISM is made up of hydrogen and helium gas, while the rest of 1% is interstellar dust and other elements. The dust is mostly solid granules (0.01 to 0.1  $\mu\text{m}$ ) made out of carbon, silicates (silicon and oxygen compounds) or iron and can be covered with ice. The denser areas in the ISM are called interstellar clouds, nebulae or molecular clouds, which vary in size and composition type (Figure 2.1).

It is clear from both observations and theory that star formation takes place in the coolest and densest regions of the interstellar gas: molecular clouds are practically the site of all star formation in the Galaxy. The clouds show structure on a wide variety of length scales and are somewhat arbitrarily subdivided into clumps, with characteristic masses of  $10^3 - 10^4 M_{\odot}$ <sup>1</sup>, radii  $2 - 5 \text{ pc}^2$ , temperature 10 K, mean number density of  $H_2$  of  $10^2 - 10^3 \text{ cm}^{-3}$ . Random velocities, estimated at 2 – 3 km/s, are observed in the clumps. Embedded in the clumps are the higher-density cloud cores, whose masses can

---

<sup>1</sup>Appendix A, table A.3 contains the constant values in SI units

<sup>2</sup>pc = parsec, a unit of distance see Appendix A:figure A.1

range from 1 to 1 000  $M_{\odot}$ , with sizes of 0.05 – 0.1 pc, temperature 10 K, mean number density of  $H_2$  of  $10^4$  –  $10^5$  cm $^{-3}$  [9].



(a) Messier 78 Nebula <sup>3</sup>



(b) Barnard 59, part of the Pipe Nebula <sup>4</sup>

**Figure 2.1.:** The dark areas in the figures above are highly dense accumulation of gas, which absorb most of the visible light from the stars behind them. Inside them are so called "star-nurseries" or star forming regions. The blue regions visible in 2.1a are caused by reflection of starlight by a high concentration of interstellar dust. The red regions, also visible in 2.1a, are caused by emission of the heated ISM.

An overall, definitive theoretical calculation of star formation is not yet available, given that, apart from complex calculation, the initial conditions are unknown. Qualitatively, it is clear that even the relatively small-scale molecular cloud cores have far too much angular momentum to be able to collapse to stellar dimensions. This problem can be solved by various physical effects, such as:

1. Fragmentation of the core into a binary or multiple system
2. Collapse of the cloud into a central stellar object surrounded by an orbiting disk, which contains most of the angular momentum.

<sup>3</sup>Credit: ESO/Igor Chekalin <https://www.eso.org/public/images/eso1105a/>

<sup>4</sup>Credit: ESO <https://www.eso.org/public/images/eso1233a/>

## 2.1.2. Star formation phases

The temperatures in the ISM vary greatly and in the colder areas ( $\sim 10$  K) hydrogen (with some traces of other elements) exists in molecular form in giant molecular clouds. These objects are very inhomogenous, with the densest regions as much as a 1 000 times the density of the more rarefied regions (Figure 2.2a [17]). Inside molecular clouds, the gas pressures are higher than those in the surrounding interstellar medium, and almost all molecular clouds in our galaxy exhibit star formation [9].

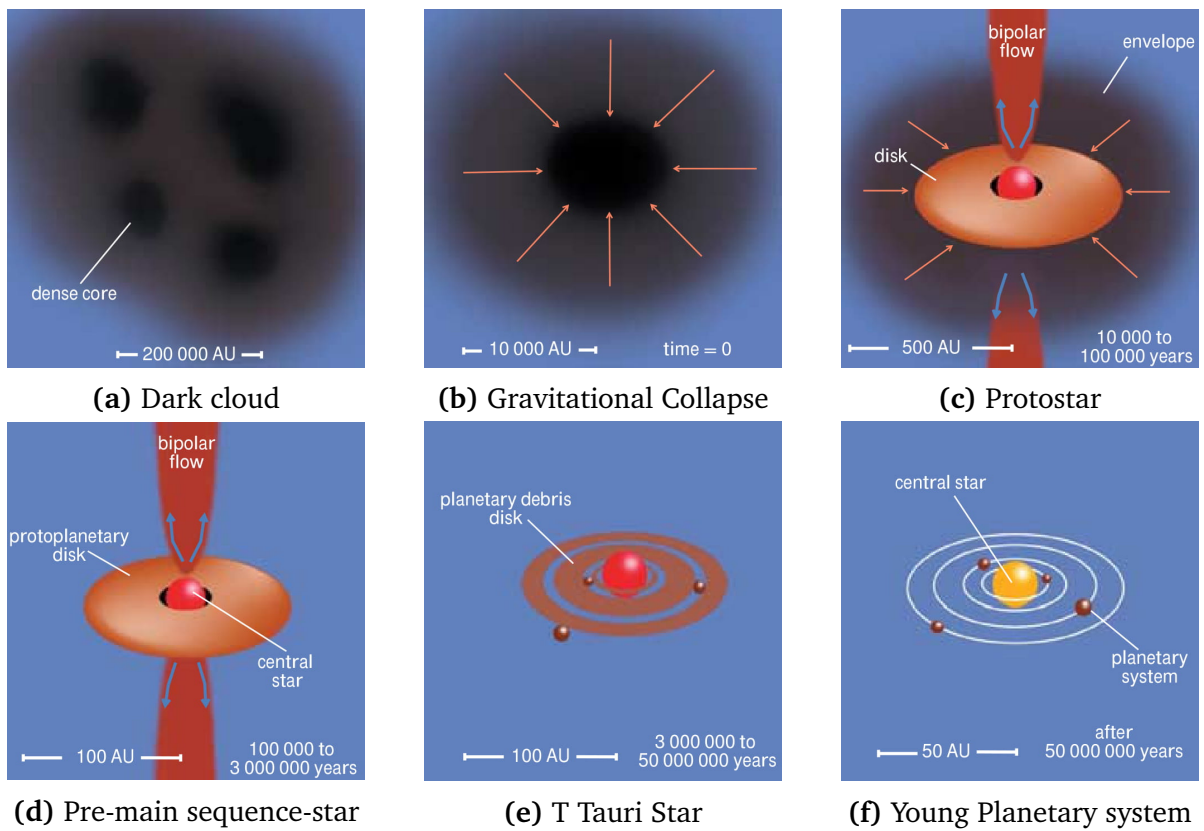


**Figure 2.2.:** The stages of formation of a Sun-like star.

Molecular clouds are usually supported against their weight by thermal pressure, turbulent gas motion and magnetic fields within. By various mechanisms the clouds become unstable and begin to collapse under their own weight (Figure 2.2b). This could be due to long time scale evolution of the cloud or a turbulence, such as supersonic turbulence, random shock interactions in the ISM, supernova shocks, stellar winds and so on [9]. At the centre of the collapsing cloud a protostar forms (Figure 2.2c). The protostar continues to rapidly accumulate mass from the surrounding envelope of gas and dust over the course of about 100 000 years. During its lifetime the

protostar progressively increases in density and shrinks in size, accreting the infalling material and shedding mass through bipolar jets. The infalling material, which had been rotating relatively slowly, speeds up as it approaches the protostar due to conservation of angular momentum. Most matter from the envelope disperses or eventually flows onto the protostar, but some of it falls into orbits of various size depending on its velocity, forming a circumstellar disk. As the accretion<sup>5</sup> process stops, the central globe of gas is no longer considered a protostar: it is now a pre-main sequence (or PMS) star (Figure 2.2d). Protostars and PMS stars are grouped under the term young stellar objects (YSO). The pre-main sequence phase of evolution lasts for tens of millions of years and its earliest phase, these objects are called T Tauri stars (derived from the archetypal star in the constellation Taurus). With no dusty envelopes, T Tauri stars are the youngest objects that can be observed with an optical telescope. They are surrounded by a disk of dust and gas – often called protoplanetary disk and can continue to eject material in their bipolar jets (Figure 2.2e). After a few million years, much of the dust and gas in the protoplanetary disk dissipates, leaving a bare PMS star in the centre, sometimes orbited by a few large bodies in a remnant debris disk. In tens of millions of years, the force of gravity eventually triumphs over the outward thermal pressure of the gas within the star and the temperature of the star's interior raises to about 10 million Kelvins – hot enough to fuse hydrogen into helium. This marks the arrival of the star on the main sequence phase of its evolution (Figure 2.2f). This period is extremely stable, and may last for billions of years. The Sun is an example of a main sequence star, which has been fusing hydrogen into Helium for 5 billions years, and is predicted to do so for 5 billion more.

## 2.2. Radiation

Before the properties of pre-main sequence stars and the surrounding circumstellar disks can be explored further, it is important to lay down the basics of radiative transfer and the underlying radiation mechanisms.

---

<sup>5</sup>accretion =<sup>def</sup> the growth or increase by the gradual accumulation of additional layers or matter

### 2.2.1. Absorption, emission and scattering

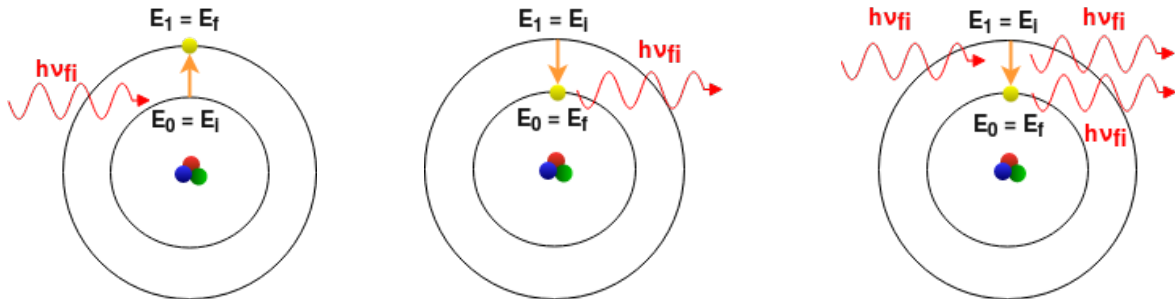
At atomic level, if the total energy decreases by  $\Delta E$  the atom emits a quantum of electromagnetic radiation called a *photon*, whose frequency  $\nu$  is determined by the equation [22]:

$$\Delta E = h\nu, \quad (2.1)$$

where  $h = 6.6256 \cdot 10^{-34} \text{ Js}$  is the *Planck constant*. Consequently, if the same atom absorbs a photon of frequency  $\nu$ , it gains energy  $\Delta E$ .

The energy levels of an electron in an atom are quantized, limiting the frequencies at which an atom can absorb or emit radiation, corresponding to the difference between the initial state  $i$  and final state  $f$  of the system:  $|E_f - E_i| = h\nu_{fi}$ . A transition from a lower energetic state to a higher energetic state by assimilation of a photon of frequency  $h\nu_{fi}$  is called **excitation** or **absorption** (Figure 2.3a). A typical lifetime for an excited state is  $10^{-8} \text{ s}$ , after which the atom may return to its lower state, radiating a photon, through the process of **spontaneous emission** (Figure 2.3b). Transitions to lower states (downward) can also be induced by another photon, whose frequency  $\nu_{\text{photon}} = \nu_{fi}$  corresponds to the downward transition, interacting and perturbing the excited state. This process is called **stimulated emission** (Figure 2.3c). While spontaneously emitted photons have randomly distributed phases and directions when leaving the atom, producing an incoherent radiation, the radiation produced through stimulated emission is coherent and propagates in the same direction as the induced radiation. **Scattering** is defined as a change in the direction of motion of a particle due to the interaction with the medium (collision with other particle). When referring to electromagnetic radiation, this process can be modelled as absorption of a photon, immediately followed by an instantaneous emission of the photon at the same wavelength, but in a different direction. On the macroscopic scale, the medium seems to reflect the radiation (e.g. atmospheric particles scatter blue light from the Sun).

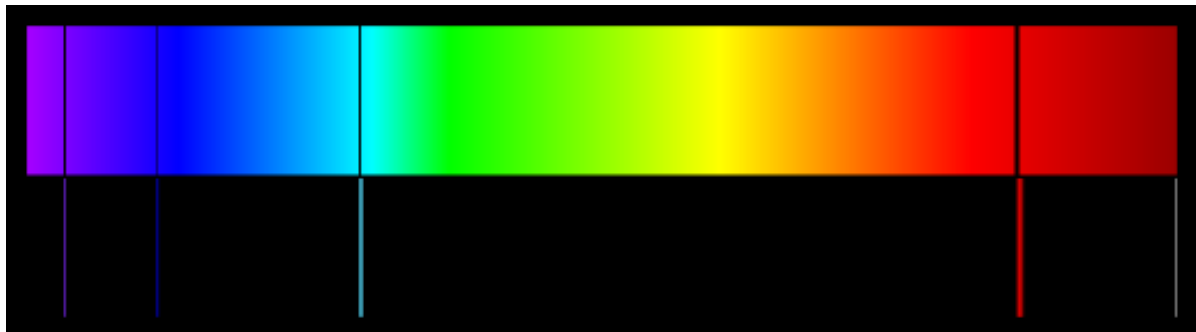
Through absorption, spontaneous emission and stimulated emission the system's energetic states can change (Figure 2.3), thus giving rise to an element-specific line spectrum (see 2.3d for Hydrogen). A hot gas under low pressures produces an emission spectrum of discrete lines. The same gas at a cooler temperature observed against



(a) **Absorption** occurs when a photon of frequency  $\nu_{\text{fi}}$  is absorbed and the system, initially in a low energy state, is excited to a higher energy state.

(b) **Spontaneous emission** is the opposite process to absorption, in the sense that the system emits a photon with the energy corresponding to  $\Delta E = h\nu_{\text{fi}} = h\nu_{\text{if}}$  as the system goes from the excited state to a lower energy state finally.

(c) **Stimulated emission** is the process in which emission occurs after a photon with exactly the same frequency as the emitted photon  $h\nu_{\text{fi}}$  interacts with the excited state.



(d) **Hydrogen Spectra:** absorption (top) lines can be seen as dark (missing) lines against the continuous spectra of light & emission (bottom) lines in colour are at the same frequency as the corresponding absorption between the same states.

Figure 2.3.: Spectral lines origin

a source of white light (continuous spectrum) shows dark absorption lines at the corresponding frequencies for the same transitions as the emission lines[22].

## 2.2.2. Blackbody radiation

A **blackbody** is a physically ideal object, which does not reflect or scatter radiation, but absorbs and re-emits radiation completely. Black holes are near-perfect blackbodies, as they absorb all the incident radiation, and although planets and stars are not perfect

blackbodies, blackbody radiation is a good first approximation for the thermal energy they emit. The wavelength distribution of the radiation follows *Planck's Law* and depends only on the temperature  $T$  of the blackbody. The intensity  $B$  of the radiation at frequency  $\nu$  is given by:

$$B_\nu(T) = \frac{2h\nu^3}{c^2} \frac{1}{e^{h\nu/kT} - 1}, \quad (2.2)$$

where  $h$  is *Planck's constant*,  $c$  is the *speed of light* ( $3 \cdot 10^8 \text{ ms}^{-1}$ ), and  $k$  is the *Boltzmann constant* ( $1.38 \cdot 10^{-23} \text{ JK}^{-1}$ ), giving the intensity  $B_\nu$  the dimension  $\text{Wm}^{-2}\text{Hz}^{-1}\text{sterad}^{-1}$ . The distribution can also be written as a function of wavelength:

$$B_\lambda(T) = \frac{2hc^2}{\lambda^5} \frac{1}{e^{hc/\lambda kT} - 1}, \quad (2.3)$$

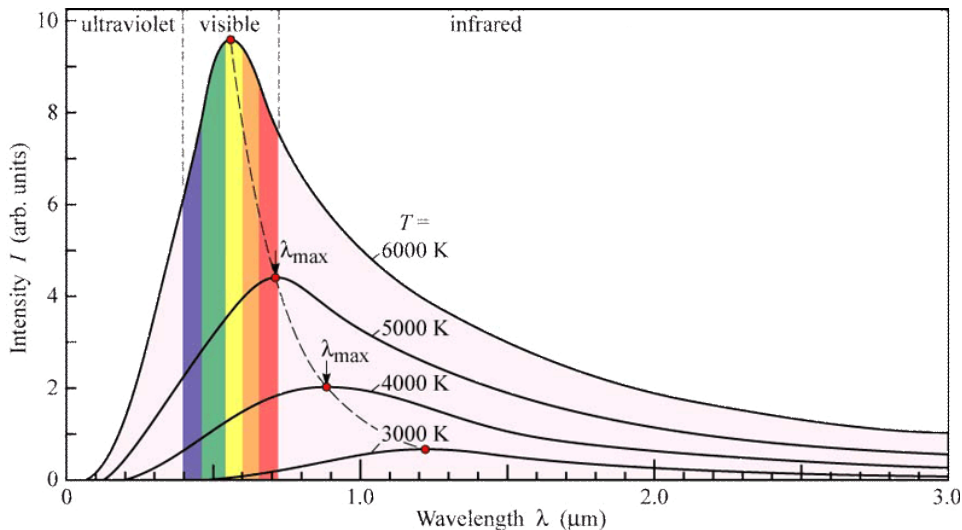


**Figure 2.4.:** Intensity distribution of blackbodies at different temperatures according to Planck's Law. The Sun, with a temperature of 5780K peaks in the area of the spectrum corresponding to visible light. [28]

The total intensity can be calculated by integrating over the spectrum:

$$B(T) = \int_0^\infty B_\lambda(T) d\lambda = \int_0^\infty B_\nu(T) d\nu \quad (2.4)$$

By replacing (2.2) into (2.4) and taking out the independent variables the following is obtained:

$$B(T) = \frac{2h}{c^2} \int_0^\infty \frac{\nu^3}{e^{h\nu/kT} - 1} d\nu \quad (2.5)$$

Integrating by substitution of the integration variable with  $x = h\nu/(kT)$ ,  $d\nu = kT dx/h$  in (2.5) the following is obtained:

$$B(T) = \frac{2h}{c^2} \frac{k^4}{h^4} T^4 \int_0^\infty \frac{x^3}{e^x - 1} dx = \frac{2k^4}{c^2 h^3} \frac{\pi^4}{15} T^4 \quad (2.6)$$

The integral in (2.6) is not easy to evaluate, but it can easily be seen that it is constant in value (independent of temperature). This can be used to express the flux density  $F = \pi B$  for isotropic radiation of intensity  $B$ , as

$$F = \sigma T^4. \quad (2.7)$$

Equation (2.7) is the *Stefan-Boltzmann Law*, with  $\sigma = 5.67 \cdot 10^{-8} \text{ W m}^{-2} \text{ K}^{-4}$ , the *Stefan-Boltzmann constant*.

### 2.2.3. Radiative Transfer

The mechanism through which energy is transferred via the propagation of radiation through a medium is called radiative transfer. The propagation of radiation through a medium is governed by the aforementioned phenomena of absorption, emission, and scattering, where absorption leads to a gain in energy, emission leads to a loss of energy and scattering represents the redistribution of energy. The equation of radiative transfer can be easily derived as explained further.

Assume a source, such as a star, which is radiating like a blackbody at temperature  $T$ , and a small area of space, in a form of a cylinder of area  $dA$ , and radius  $dr$ , at a distance  $d$  from the source, such that it spans the solid angle  $d\omega$ : Figure 2.5.

If the intensity changes by an amount  $dI_\nu$  going through the cylinder, then in the time interval  $dt$ , the energy changes by:

$$dE = dI_\nu dA d\nu d\omega dt \quad (2.8)$$

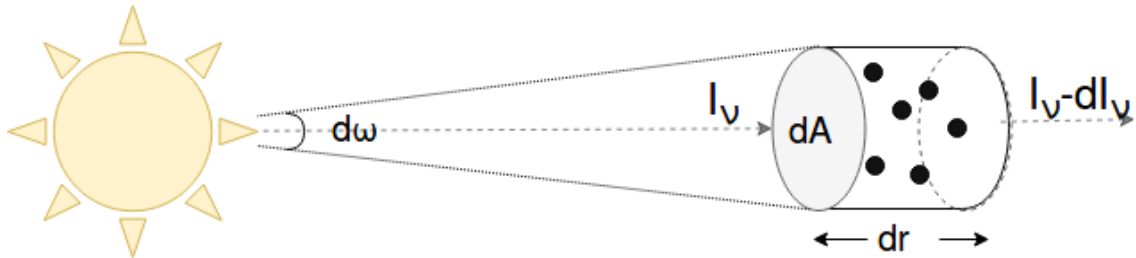


**Figure 2.5.:** Extinction and optical depth

This energy difference must be equal to the absorption minus the emission in the cylinder element. The fraction of absorbed energy depends on the opacity of the medium at the given frequency  $\nu$ :

$$dE_{\text{abs}} = \alpha_\nu I_\nu dr dA d\nu d\omega dt \quad (2.9)$$

Let the emission coefficient of the medium be  $j_\nu$ , describing the amount of energy emitted at frequency  $\nu$ , per Hertz, per unit time, into unit solid angle from unit volume. Then the energy emitted is

$$dE_{\text{em}} = j_\nu dr dA d\nu d\omega dt. \quad (2.10)$$

By replacing (2.8), (2.9), (2.10) into the equation for conservation of energy

$$dE = -dE_{\text{abs}} + dE_{\text{em}}, \quad (2.11)$$

one obtains:

$$dI_\nu = -\alpha_\nu I_\nu dr + j_\nu dr \quad (2.12)$$

or

$$\frac{dI_\nu}{\alpha_\nu dr} = -I_\nu + \frac{j_\nu}{\alpha_\nu}. \quad (2.13)$$

The **optical depth  $\tau$** , is in astrophysics a measure of the extinction coefficient or absorptivity of a medium at a certain frequency  $\nu$ . Therefore the total optical depth, expressing how much of the light will be absorbed by the medium through a certain

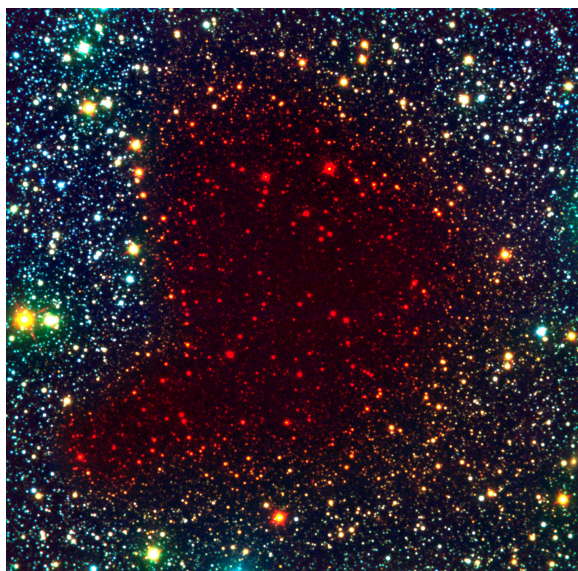
path is the integral sum of the extinction coefficient  $\alpha_\nu$  along that path:

$$\tau_\nu = \int_0^r \alpha_\nu dr = \sigma N, \quad (2.14)$$

and it can also be expressed in terms of the number density  $N$  and the absorption cross section  $\sigma$ . From the definition one can understand that an optically thick material, with a high value for the optical depth  $\tau$ , is highly obscuring and does not let much of the light pass through. Figure 2.6 exemplifies this with a real celestial object.



(a) Barnard 68 three-colour composite reproduced from one blue (B), one green-yellow (V) and one near-infrared (I) exposure<sup>6</sup>



(b) Barnard 68, false-colour composite based on a visible (here rendered as blue), a near-infrared (green) and an infrared (red) image<sup>7</sup>

**Figure 2.6.:** Comparing the two composite expositions of the same astronomical object, it can be clearly seen in 2.6a that the globule is optically thick for the visible spectrum, not letting any light from the stars behind pass through, while in 2.6b a multitude of stars appear behind the globule, coloured red in the image, making the globule optically thin in the infrared region of the spectrum.

The *source function*  $S_\nu$  is a measure of the emission to absorption coefficient in the case of no scattering, indicating how many photons are removed and replaced by new

<sup>6</sup>Credit: ESO, <https://www.eso.org/public/images/eso0102a/>

<sup>7</sup>Credit: ESO, <https://www.eso.org/public/images/eso0102b/>

ones as a beam of light passes through the material:

$$S_\nu = \frac{j_\nu}{\alpha_\nu} \quad (2.15)$$

By replacing the newly defined optical depth (2.14) and source function (2.15) into the derived equation (2.13) from the conservation of energy, the following is obtained:

$$\frac{dI_\nu}{d\tau_\nu} = -I_\nu + S_\nu \quad (2.16)$$

Equation (2.16) is the basic equation of radiative transfer. If the incident intensity is smaller than the source function,  $I_\nu < S_\nu$ , the intensity increases in the direction of propagation, meaning also that the medium is emitting more than it is absorbing for the given frequency  $\nu$ . Whereas, if the incident intensity is larger than the source function,  $I_\nu > S_\nu$ , then  $dI_\nu/d\tau < 0$  and the outgoing intensity will be smaller, meaning the medium is absorbent or optically thick at the given frequency. In equilibrium, the emitted and absorbed energies are equal,  $I_\nu = S_\nu$ , and the radiation of the medium is that of a blackbody, with the source function given by:

$$S_\nu = B_\nu(T) = \frac{2h\nu^3}{c^2} \frac{1}{e^{h\nu/kT} - 1} \quad (2.17)$$

A formal solution to the radiative transfer equation (2.16) for the outgoing intensity is made up of an exponential decay, with the exponent equal to the absorption coefficient, of the initial intensity ( $I_\nu(0)$ ), plus the emission of the medium at the given frequency:

$$I_\nu(\tau_\nu) = I_\nu(0)e^{-\tau_\nu} + \int_0^{\tau_\nu} e^{-(\tau_\nu-t)} S_\nu(t) dt \quad (2.18)$$

The solution is only formal, because  $S_\nu$  is usually unknown, and thus equation (2.18) must be solved simultaneously for the intensity and source function.

## 2.3. Stellar properties

### 2.3.1. Effective Temperature $T_e$ [K]

Temperatures in the Universe range from 0 to millions of degrees (K), and the measure of the temperature depends on the physical phenomena underlying the definition of temperature. The most useful way to obtain a temperature is by fitting it against a blackbody spectra. The *effective temperature*  $T_e$  refers to the surface of the star and is defined as the temperature of a blackbody which radiates with the same total flux density as the star. In other words, for a value of the  $T_e$  which ensures the Stefan-Boltzmann law gives the correct flux density  $F$  on the surface of the star, one finds the effective temperature. From (2.7), the flux density at the surface becomes then

$$F = \sigma T_e^4. \quad (2.19)$$

### 2.3.2. Luminosity $L_\star$ [L<sub>⊙</sub>]

The luminosity of a star is given by the total energy radiated per second from its surface. It can be calculated for a specific wavelength, or for all wavelengths (**Bolometric luminosity**). The brightness of the star as measured from Earth is called **Apparent Magnitude**<sup>8</sup> and it does not accurately describe the star's luminosity, as it is also dependent on the distance from the Earth to the star. Given that at a distance  $r$  from the source (star), the same amount of energy is spread to an area equal to the spherical surface  $4\pi r^2$ , the flux density  $F$  falls off proportionally to  $1/r^2$ , as represented in Figure 2.7. Assuming an isotropically radiating star of luminosity  $L$ , the flux  $F$  at a distance  $r$  from the star would be given by the relation [22]:

$$L = 4\pi r^2 F \quad (2.20)$$

By replacing  $F$  from (2.19) in equation (2.20) we obtain the relationship between the radius  $R_\star$ , temperature  $T_e$  and luminosity of a star  $L_\star$ .

$$L_\star = 4\pi\sigma R_\star^2 T_e^4 \quad (2.21)$$

---

<sup>8</sup>The **Absolute Magnitude** of a star is defined as the apparent magnitude at exactly 10 parsec from the star.

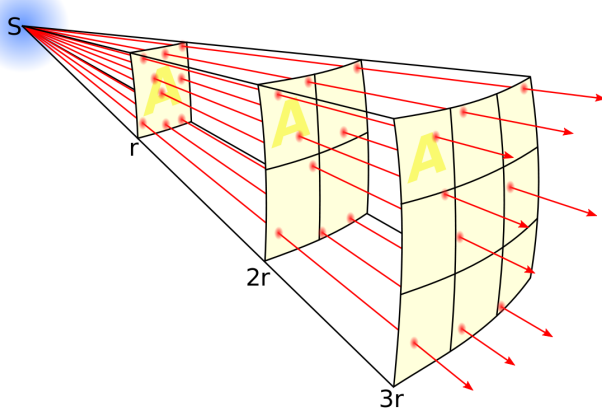


**Figure 2.7.:** Inverse square law <sup>9</sup>: As the radius increases from  $r$  to  $2r$ , the same radiation passes now through 4 times the surface area  $A$ , and as the radius increase to  $3r$ , the surface area increases to  $9A$ .

### 2.3.3. Stellar Mass $M_\star [M_\odot]$

Stars are massive gaseous bodies which generate energy through nuclear fusion in the core, and release it as radiation. The mass of the star  $M_\star$  (usually expressed in terms of the mass of the Sun  $M_\odot$ ) determines the star's properties (such as temperature, luminosity and size), but most importantly its evolution track. The pressure of the energy emitted from the core would cause the star to explode, were it not counteracted by the gravity of the surrounding material. When the sum of the gravitational and pressure forces acting on a volume element is zero (Figure 2.8), hydrostatic equilibrium is reached, and the star is stable.

When the balance changes, however, so does the state of the star. Stars can have masses in a relatively small interval: if the mass of a star is less than  $0.08 M_\odot$  or bigger than  $100 M_\odot$  the star becomes unstable [40]. The smallest stellar masses observed are about  $0.05 M_\odot$ , and the largest one could be up to  $150 M_\odot$  [22]. These values are however approximate as they are based on an empirical mass–luminosity relation, which can be used to estimate stellar masses:

$$L \propto M^{3.8} \quad (2.22)$$

---

<sup>9</sup>By Borb, CC BY-SA 3.0, <https://commons.wikimedia.org/w/index.php?curid=3816716>

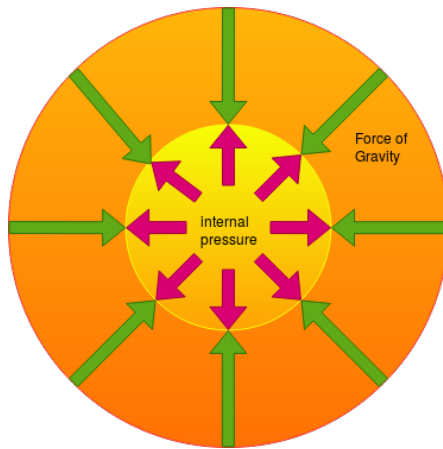


**Figure 2.8.:** Hydrostatic equilibrium in stellar interiors is achieved when the **gravitational force** matches the **internal pressure** at each point.

It is important to note that the relation is only approximate, and can be considered valid for main sequence stars. The only stars with accurately known masses are the ones found in binary systems, where the masses of the individual components can be determined by observing the motions of both components relative to the centre of mass. Less than half of all stars are single stars like the Sun, while more than 50 % belong to systems consisting of two or more members (which is binary at some level).

### 2.3.4. T Tauri stars

The largest group of pre-main sequence stars are the T Tauri stars [38]. They are young variable stars generally with masses lower than  $2 M_{\odot}$ , of spectral types F, G, K or M<sup>10</sup>. Their surface temperatures are similar to those of main sequence stars of the same mass, but they are significantly more luminous because of their larger radii. They are in the process of contracting towards the main sequence and can be subject to luminosity variabilities. The variability and the spectral peculiarities appear to be connected with vigorous stellar activity on their surface, which may be due to their rapid rotation (compared to the Sun), or, in some cases the effects of continued accretion of matter [38].

There are several T Tauri subtypes [38]: classical T Tauri stars (CTTS) with evidence of an accretion disk; weak-lined or 'naked' T Tauri stars (WTTS), which are

---

<sup>10</sup>See Appendix C, C.1 for more details on stellar spectra and C.2 for more information on T Tauri star classification

surrounded by a thin debris disk or no observable disk; FU Orionis stars, which are T Tauri stars exhibiting significant brightenings. Similar young pre-main sequence stars, are Herbig Ae/Be type stars, which have higher masses (between 2 and  $8 M_{\odot}$ ) and are hotter (of spectral type A or B). They may sometimes show significant brightness variability. Herbig Ae/Be stars are rare, as they quickly contract towards the main sequence, but, being bright, they are easier to observe [38]. As they are not in the main sequence yet, both stellar types (T Tauri and Herbig Ae/be) are not burning hydrogen, and are powered by gravitational energy released as the stars contract.

Typical parameter ranges for T Tauri stars are:

$M_{\star}$	$1 - 3 M_{\odot}$
$R_{\star}$	$2 - 6 R_{\odot}$
$L_{\star}$	$4 - 50 L_{\odot}$
age	$1 - 5 \cdot 10^6$ years

**Table 2.1.:** Typical T Tauri parameters [38] (p.286)

Considering the fainter luminosities observed in T Tauri stars in Table A.4 in Appendix A, and the higher limit for luminosities from Table 2.1, as well as temperatures ranging all the way up to the neighbouring limit between T Tauri and Herbig Ae/Be stars, the following parameter space is chosen for the investigation:

$T_{\text{eff}}$	$3\,500 - 9\,000$ K
$L_{\star}$	$0.6 - 50 L_{\odot}$

Through the combination of temperature and luminosity, the radius of the star is fixed, according to equation (2.21) and might be well outside the interval in Table 2.1. The mass of the star is set to the default value in *mol3d*,  $M_{\star} = 0.7 M_{\odot}$ , unless otherwise specified. This parameter is not expected to influence the result of the simulations with regard to the luminosity variability investigation.

### 2.3.5. Variable Stars

Stars with changing brightness (or absolute magnitudes) are called *variables* or *variable stars* (about 40 000 stars are known or suspected to be variable [22]). Flare stars are young stars which present flare outbursts on the surface at irregular intervals. Such a flare can cause a brightening by up to 4-5 magnitudes [22] and it is common for protostar and its accretion disc to cause jet-like flares as seen in Figure 2.9.



**Figure 2.9.:** Image of Herbig-Haro object (HH) 212, located in a dense star-forming region of the Horsehead Nebula with very large almost symmetric flares in orange. The central star is very young (thousands of years old) and it can be observed masked by the surrounding dusty disk (central dark region from which flares seem to originate), which is seen here edge-on. The star's pulses vary quite regularly, and over a short timescale (maybe even as short as 30 years). Further out from the centre, large bow shocks caused by ejected gas colliding with dust and gas at speeds of several hundred kilometres per second spread out into interstellar space. **Credit:** ESO/M. McCaughrean <https://www.eso.org/public/images/potw1541a/>

The **apparent magnitude** ( $m$ ) of an astronomical object is a measurea of its brightness as observed from Earth and is related to the flux by:

$$m_\lambda = -5 \log_{10} \left( \frac{F_\lambda}{F_{\lambda,0}} \right) = -2.5 \log_{10} \left( \frac{F_\lambda}{F_{\lambda,0}} \right) \quad (2.23)$$

where  $F_{\lambda,0}$  is a reference flux, and  $\lambda$  represents here a frequency band.

A difference of 1 in magnitude corresponds to a change in brightness by a factor of 2.512, to be more precise.

A flare lights up in a few seconds, and fades away in a few minutes, but the same star can flare up several times in one day. Newly formed stars, such as T Tauri stars, are contracting toward the main sequence. They may change brightness very rapidly and commonly have irregular brightness variations (*FU Orionis* brightened in 1937 by 6 magnitudes [38]). In 1969 *V1057 Cygni* brightened by six magnitudes, and had remained fairly constant since [38], [22]. Altough the process is not fully understood [22], according to a widely accepted picture, such objects are accreting material from a circumstellar disk, which can lead to outburst phenomena or violent infalls followed by shocks that cool by emitting a hot continuum, often called veiling[2]. Classical T Tauri stars vary on timescales of minutes to years, with ranges of up to several magnitudes and rarely show periodicities (are irregular) [39]. Many stars with masses between 0.6 and  $0.8M_\odot$  also have periods of a day or less, in which case nightly observations are inssufficient [44]. This can be counteracted by using a global telescope network, such as YETI, to monitor the objects continuuosly and determine if the variabilities are due to a transiting planet[35].

## 2.4. Circumstellar Disks

As seen in section 2.1, as clouds collapse into protostars, much of the the angular momentum of the collapsing cloud is transffered to the rotating circumstellar disk of gas and dust, which lasts 1–10 Myr before being photo-dissipated. It is thought that angular momentum is significantly reduced by magnetic coupling between the star and the disk and also through the outflow in the poles, which is strongest during the protostellar phase. A schematic of a typical circularly-symmetric disk can be seen in Figure 3.6. Even though the disks usually contain only a small percentage of the

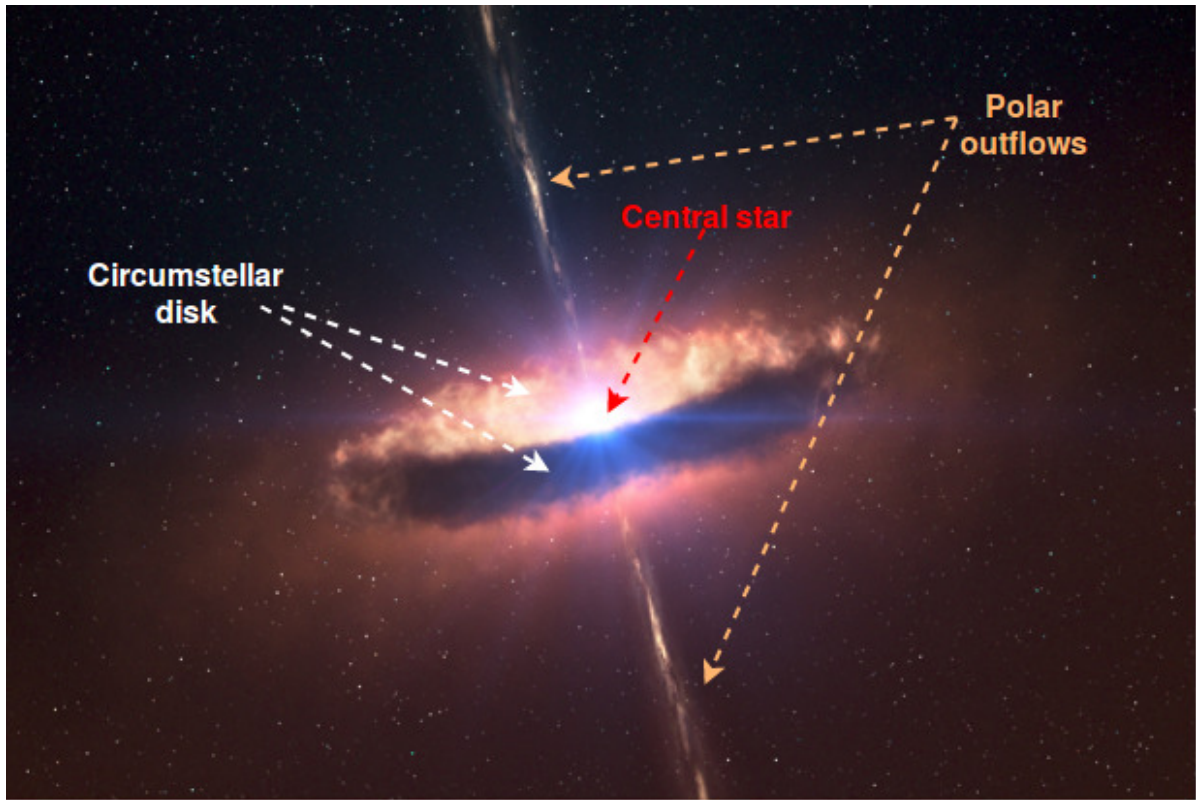


**Figure 2.10.:** Artist impression (with added annotations) of pre-main sequence star with disk. The disk extends to about 130AU, and has a mass similar to that of the central star. Jets can be observed at either pole of the star, spewing matter. **Credit:** ESO/L. Calçada/M. Kornmesser <https://www.eso.org/public/images/eso1029a/>

material going into a young star, they are of great interest to study, because they are the place where planets may form.

How common are circumstellar disks? Using data from the IRAS sky survey, two teams [11] and [47] discovered that approximately half of the T-Tauri stars observed have far infrared spectral energy distributions (SEDs), characteristic of heated dust and not of the photosphere. The relative low visual extinction (absorbed light from the star) suggested that the dust was in a flattened distribution. The first pictures of disks taken with the Hubble Space Telescope demonstrated clearly that the dust distribution followed the theoretical pattern of a disk [6]. Circumstellar disks (2.11a) are gently flared<sup>11</sup> in the outer region due to the warming of the matter, and have some edge at a distance from the star (called further inner radius of the disk  $R_{in}$ , as

<sup>11</sup>**flared** =<sup>def</sup> opening or spreading outward

per Figure 2.11b), and are heated mainly by radiation (as opposed to accretion). Most young disks are also accompanied by mass losses in columns around the polar axes.

The excess IR emission, sometimes amounting up to 2/3 of the observed flux [38], originates in the emission from the warm dust in the disk. Variability in the IR may arise in cool material in an accretion disk, in hot spots, as matter accretes onto the star at a variable rate, as well as from the rotation of hot and cold spots on the surface of the star [38]. One hypothesis about the brightness variability of T Tauri stars surrounded by particularly dense disks ( $M_{\text{disk}} \sim 10^{-4} M_{\odot}$ ) is that blobs in the accreted material produce outbursts [49].

### 2.4.1. Disk Model

When describing the disk in cartesian coordinates (Figure 2.11a), the  $z$  direction is considered to be the direction of the polar outflow (with no preference for the positive direction), or the direction perpendicular to the plane through the centre of the disk, which are identical in the considered model. In the  $xy$ -plane of the disk, the radius  $r$  is defined as the distance to the central star  $r = \sqrt{x^2 + y^2}$ . Because the disk is circularly symmetric in the  $xy$ -plane, cylindrical coordinates  $(r, \theta, z)$  are appropriate and sufficient for the model description, but cartesians will be used in figures.

The dust is in hydrostatic equilibrium throughout the disk in figure 2.11b. The system of equations describing the dust density in such a disk is given by the following equations:

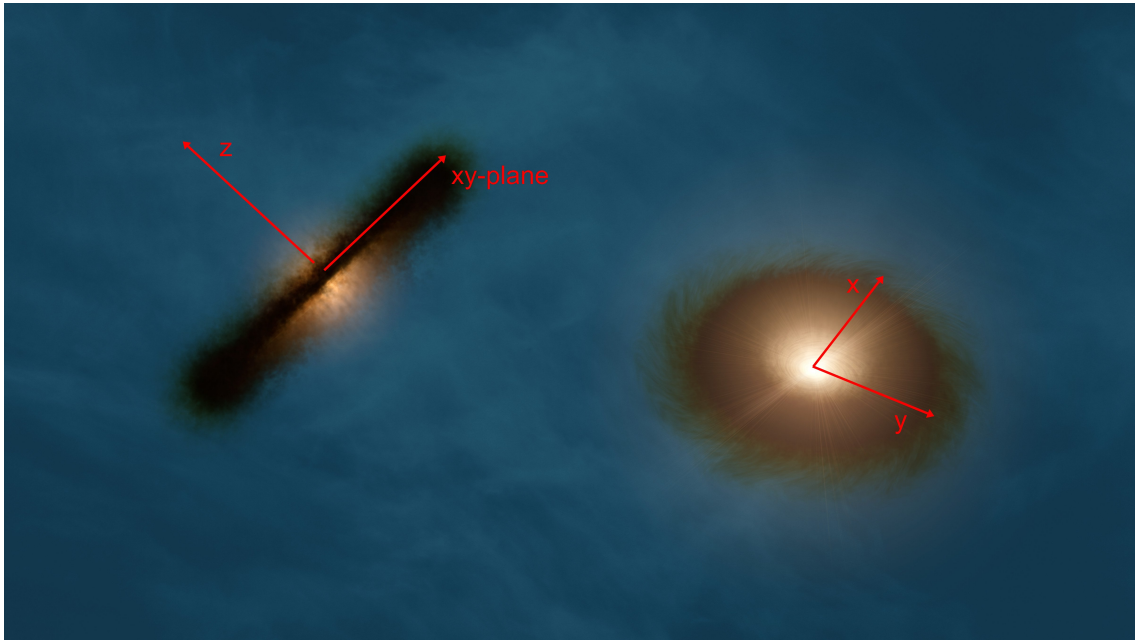
$$\begin{aligned} \rho(r, z)^{\text{Sh-Su}} &= \left( \frac{r}{100} \right)^{-\alpha} \exp \left( -\frac{1}{2} \frac{z^2}{h(r)^2} \right), \\ h(r) &= h_0 \left( \frac{r}{100} \right)^{\beta}, \quad \alpha = 2.625, \beta = 1.125, h_0 = 10 \text{ AU} \end{aligned} \quad (2.24)$$

$$\rho(r, z)^{\text{Ly-P}} = \rho(r, z)^{\text{Sh-Su}} \exp \left( \left( -\frac{r}{100} \right)^{(2+\beta-\alpha)} \right)$$

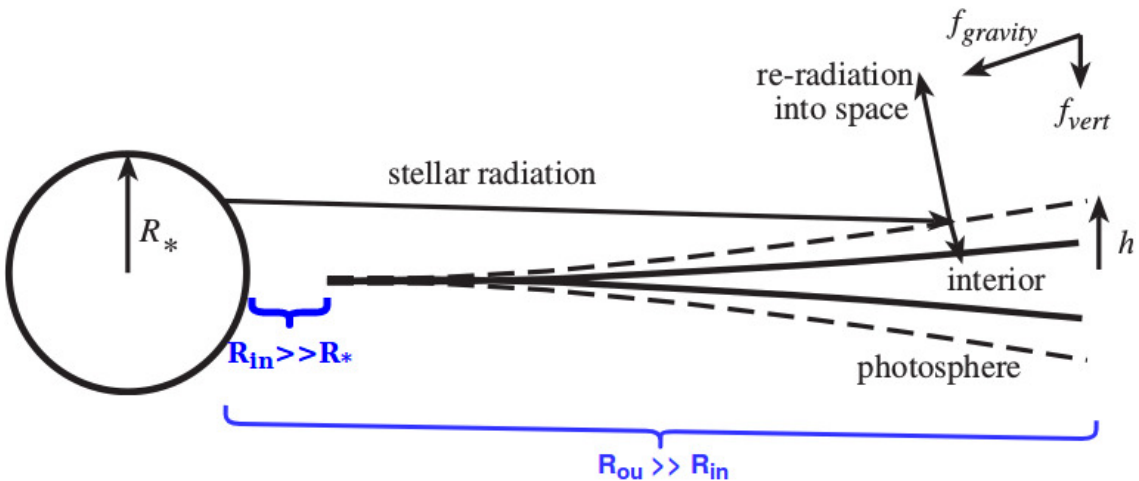
where Sh – Su stands for the Shakura and Sunyaev model[45], originally implemented in the chosen radiative transfer algorithm *mol3d*<sup>12</sup> [36], and Ly – P stands for the improved Lynden-Bell and Pringle model [31].

---

<sup>12</sup>See Appendix B for a more detailed description



(a) Artist impression of two circumstellar disks. The one on the left is seen edge on by the observer, while the disk on the right is almost face-on with a slight incline towards the observer. Cartesians coordinates as used in this thesis are added in red.



(b) Schematic of star with section through flared circumstellar disk. The radius of the star  $R_*$  is usually a few solar radii  $R_\odot$ , while the rim of the disk approaches the star usually at a couple of astronomical units. Between the star and the inner radius of the disk  $R_{in}$  all dust is considered to have been accreted, due to unstable orbits, or the temperatures are too high for the dust to exist, making the dust density in this area null. The disks outer radius is hard to distinguish as a low density, but non-zero distribution of dust may exist beyond the outer radius  $R_{out}$ , which is usually a couple of hundred astronomical units.

All the simulations are run with a modified version of *mol3d*, using the Lynden-Bell density function. Typical values used for the simulation are found in the following Table 2.2.

$\alpha$	2.625
$\beta$	1.125
$h_0$	10 AU
$R_{\text{in}}$	1 AU
$R_{\text{out}}$	200 AU
$M_{\text{disk}}$	$10^{-4} M_{\odot}$

**Table 2.2.:** Disk parameters

### 2.4.2. Interstellar Dust

Though originally thought as transparent, the interstellar medium is actually filled with dust, which also forms circumstellar disks. The dust was first observed when deducing that the apparent magnitude of stars is dimmed by some intervening material. Extinction due to dust varies with the direction of incident light, and is due to the particles having diameters near the wavelength of light ( $0.01 - 0.2 \mu\text{m}$ ) [1]. Such particles scatter light extremely efficiently. Gas can also cause extinction by scattering, but the efficiency per unit mass is much smaller.

Interstellar dust particles can cause extinction in two ways [22]

- Through absorption, the radiant energy is transformed into heat, which is then re-radiated at infrared wavelengths corresponding to the temperature of the dust particles.
- Through scattering, the direction of propagation is changed, which leads to a reduction of the intensity in the original direction of propagation.

For simplicity in calculating the coefficient of extinction  $C_{\text{ext}}$  (equation (2.25)) for dust particles, they are assumed to be spheres with the same radius  $a$ , and therefore

geometrical cross-section  $\pi a^2$ .

$$C_{\text{ext}} = Q_{\text{ext}} \pi a^2, \quad (2.25)$$

where  $Q_{\text{ext}}$  is the extinction efficiency factor. Consider (as before in section 2.2.3, figure 2.5) a volume element with cross section  $dA$ , incident to the radiation, and length  $dl$ . If the particle density is  $n$ , the total number of particles in a unit volume is  $N = ndAdl$ , while the fraction of the area covered by the particles will be  $C_{\text{ext}}/dA$ . On the basis of the previous equation (2.14), the optical depth over a path of length  $r$  can be expressed as a function of the extinction coefficient as:

$$\tau = N\sigma = \int_0^r n C_{\text{ext}} dl \approx C_{\text{ext}} \bar{n} r \approx Q_{\text{ext}} \pi a^2 \bar{n} r \quad (2.26)$$

where  $\bar{n}$  is the average density along the path.

The extinction factor  $Q_{\text{ext}} = Q_{\text{abs}} + Q_{\text{sca}}$  is the sum of the absorption and the scattering extinction factors, and can be calculated for a given frequency from the quantity  $x = 2\pi a/\lambda$ , where  $a$  is the radius of the dust particles, and  $m$  is the refractive index ( $Q_{\text{ext}} = Q_{\text{ext}}(x, m)$ ). When  $x \ll 1$ , the particle is much smaller than the wavelength so elastic or Rayleigh scattering occurs, whereas for  $x \geq 1$  Mie scattering occurs (Figure 2.12).

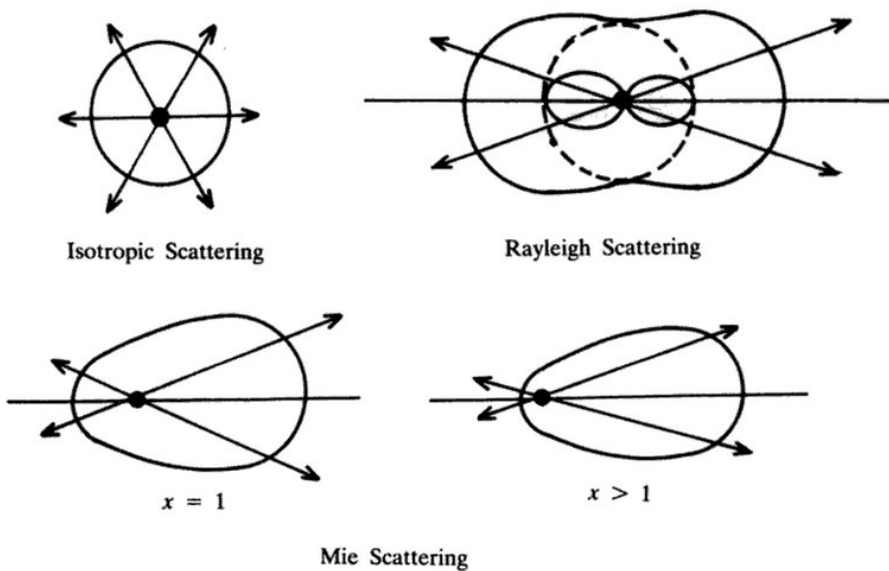


**Figure 2.12.:** Mie scattering as a function of direction versus other types of scattering [48]

An observable phenomena that happens because of dust is the **reddening** of stars due to the fact that extinction becomes larger for shorter wavelengths. This means that going from red to ultraviolet the extinction is roughly inversely proportional to wavelength. For this reason, the light of distant stars is redder than would be expected on the basis of their spectral class. At the same time, if a dust cloud is close to a bright star, it will reflect much of the light, more so in the blue end of the spectrum (like the Messier reflection nebula in 2.1a). Individual dust clouds can be observed as bright reflection nebulae.

Dust particles polarise light from the stars. Since this effect could not be produced by spherical particles, the interstellar dust particles must be non-spherical in shape. Through alignment by the interstellar magnetic field, dust particles will polarise radiation passing through a cloud. In addition to scattering radiation, dust also absorbs energy and re-radiate it at infrared wavelengths, corresponding to their temperature. For interstellar dust (including dark nebulae) at 10 – 20K, the corresponding peak according to Wien's displacement law:

$$\lambda_{\max} = \frac{2898}{T[K]} \mu m, \quad (2.27)$$

would be at  $300 - 150 \mu m$ , while for dust at the inner edge of a circumstellar disk, near a hot star, the temperatures may be  $300 - 1500 K$ [1] and the maximum emission is then at  $1 - 10 \mu m$ . Dust can be detected and observed in the infrared due to its strong thermal emission.

From the peaks in the extinction curves, it may be concluded that interstellar dust contains water ice and silicates, as well as graphite. A typical composition [50] is 63.5% astrosilicate combined with carbon in different polarisations. The sizes of the grains, deduced from their scattering properties are usually smaller than  $1 \mu m$ .

# Chapter 3.

## Visibility

### 3.1. Observations

The closest T Tauri stars are in the Taurus and  $\rho$ -Ophiuchus star-forming regions [29] located at a distance  $d = 140 \pm 10\text{ pc}$  [23]. In order to observe a circumstellar disk orbiting a T Tauri star, with an inner radius of  $R_{\text{in}} = 1\text{ AU}$ , one would need an angular resolution of  $\theta = R_{\text{in}}/d = 1/140\text{ arcsec} \approx 0.007\text{ arcsec}^{13}$ . According to the Rayleigh criterion:

$$\theta = 1.22 \frac{\lambda}{D} \quad (3.1)$$

the angular resolution,  $\theta$ , increases with wavelength  $\lambda$  and decreases with the diameter of the apparatus  $D$ . As such, in order to obtain an angular resolution of  $0.0071\text{arcsec}$  for a wavelength corresponding to very hot dust  $\lambda = 2\mu\text{m}$ , an apparatus of  $D = 70.89\text{ m}$  would be the minimum requirement.

The largest existing single mirror telescopes have diameters of  $8.2\text{ m}$ , while the largest segmented mirror at present has a diameter of  $10.4\text{ m}$ , and is in use at the Gran Telescopio Canarias on the Spanish island of La Palma. Three very large segmented mirror telescopes are planned to go online in the 2020s: **The Giant Magellan Telescope** ( $D = 25\text{ m}$ ) at Las Campana Observatory, Chile; **The European Extremely Large Telescope** ( $D = 39.3\text{ m}$ ), at Cerro Armazones, Chile; and the **Thirty Meter Telescope** ( $D = 30\text{ m}$ ), at Mauna Kea, Hawaii.

---

<sup>13</sup>See Appendix A, Figure A.1 as visual aid

None of the reflective telescopes, either existing or planned for the near future, would allow for the before calculated angular resolution  $\theta_\lambda$ . In order to observe hot or warm dust in the near-infrared or mid-infrared region with a resolution better than 1 AU at distances of 140 parsecs ( $\approx 450$  ly) a larger apparatus is needed. Such an observing feat is only possible today with long-baseline interferometry.

### 3.1.1. Long-baseline interferometry

Astronomic interferometers are arrays of separate telescopes, which work together to provide a higher resolution image by means of interferometry. In the simplest example (Figure 3.1) two telescopes simultaneously observing a source, situated at distance  $b$  from one another, known as the **baseline** of the interferometer, manage to mimic a larger telescope with diameter  $D = b$ . The main drawback of this method is that the

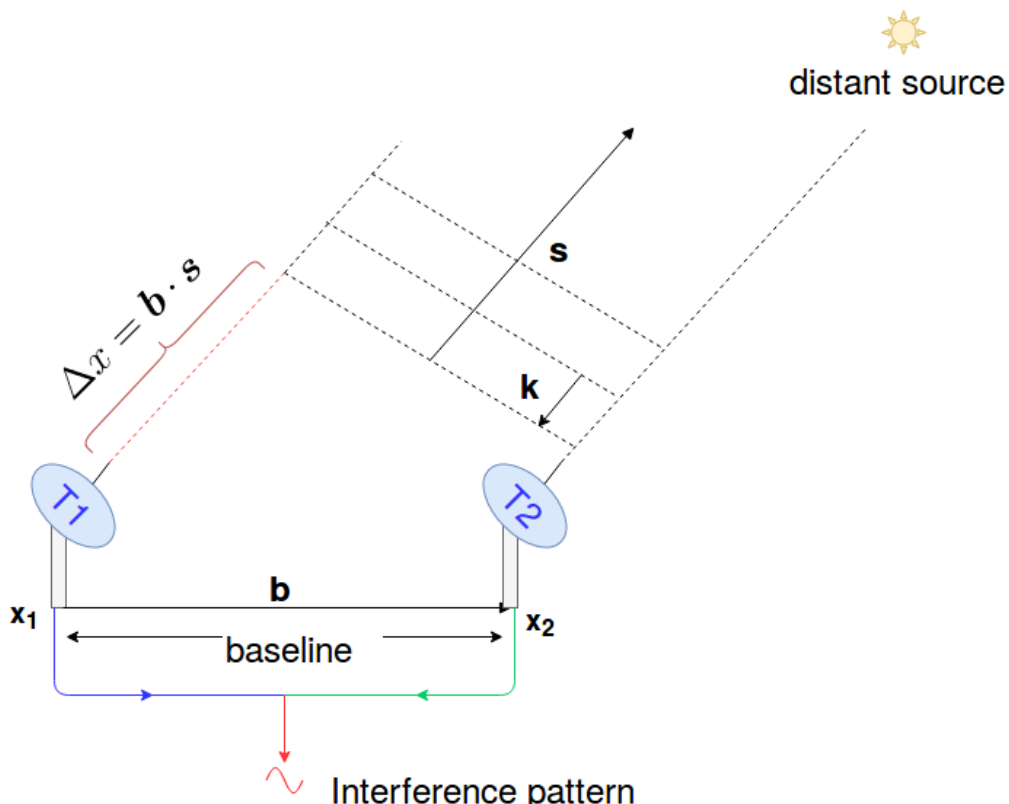


**Figure 3.1.:** Schematic of long-baseline interference. Assume telescopes  $T_1$  and  $T_2$  are located at a distance  $\mathbf{b}$  apart, called baseline. The signals received from a distant source, with relative position vector  $\mathbf{s}$ , will have a path difference  $\Delta x = \mathbf{b} \cdot \mathbf{s}$  and, when combined, will produce an interference pattern.

image is incomplete and the incident flux is dependent on the surface of the individual telescopes ( $\pi a^2/2$ , for two identical telescopes with circular collection area of diameter  $a$ ). Some additional delay path can be added artificially to one or both of the signals coming from either telescope by directing the wavefront through a longer path before the signals are combined, but will not be discussed further as it is of little significance. Consider the setup of Figure 3.1, where telescopes **T1** and **T2** are located at positions  $x_1$  and  $x_2$ , respectively such that  $b = x_2 - x_1$ . Both telescopes point at a distant source  $S$ , in the direction given by the unit vector  $s$ . For a sufficiently distant source it can be assumed that the source is monochromatic and coherent, with planar wavefronts [26]. Therefore the incident optical fields  $\Phi_1$  and  $\Phi_2$  at **T1** and **T2**, respectively, can be written as:

$$\Phi_1 = I_s e^{ik \cdot x_1} e^{-i\omega t} = I_s e^{-i(ks \cdot x_1 + \omega t)} \quad (3.2)$$

$$\Phi_2 = I_s e^{-i(k \cdot x_2 + \omega t)} = I_s e^{-i(ks \cdot x_1 + ks \cdot b + \omega t)}, \quad (3.3)$$

where  $k = \omega/c$  is the wave number of the planar wave, and  $k = kn = -ks$  is the corresponding wave vector. Without loss of generality, the common phase factor  $e^{-i(ks \cdot x_1)}$  can be absorbed into the normalisation of the optical fields and the direct combination of the wave fields results in a net field with phase given by:

$$\Phi_{\text{net}} = \Phi_1 + \Phi_2 \sim e^{-i\omega t} e^{-iks \cdot b}, \quad (3.4)$$

from which the resulting time-averaged detected power is:

$$P \propto \Phi_{\text{net}} \Phi_{\text{net}}^* \sim 2(1 + \cos(ks \cdot b)) \quad (3.5)$$

or, expressed in terms of the flux power  $F$ , the unit energy per unit time per unit area, and the total area of the collecting aperture  $2A = \pi a^2/2$ :

$$P = \pi a^2 F (1 + \cos(ks \cdot b)). \quad (3.6)$$

Equation 3.6 has the form of an infinite series of power oscillations or *interference fringes*. The fringe phase

$$\phi = \frac{2\pi b \cos(\theta)}{\lambda} \quad (3.7)$$

depends on  $\theta$ , the angle of observation, or the angle between  $s$  and  $b$ , as follows:

$$\frac{d\phi}{d\theta} = 2\pi \frac{b \sin(\theta)}{\lambda} \quad (3.8)$$

The fringe period ( $\Delta\phi = 2\pi$ ) corresponds to an angular change

$$\Delta\theta = \frac{\lambda}{B} \quad (3.9)$$

where  $B = b \sin(\theta)$  is the **projected baseline**, which is referred to simply as baseline as well, as it is the value used in calculating visibility for a given observation.

As seen in Figure 3.2, the angular resolution for an interference pattern of an extended source such as a star is  $\lambda/B$ , far better than that of a single telescope  $\lambda/a$ , where  $a$  is the diameter of the telescope.

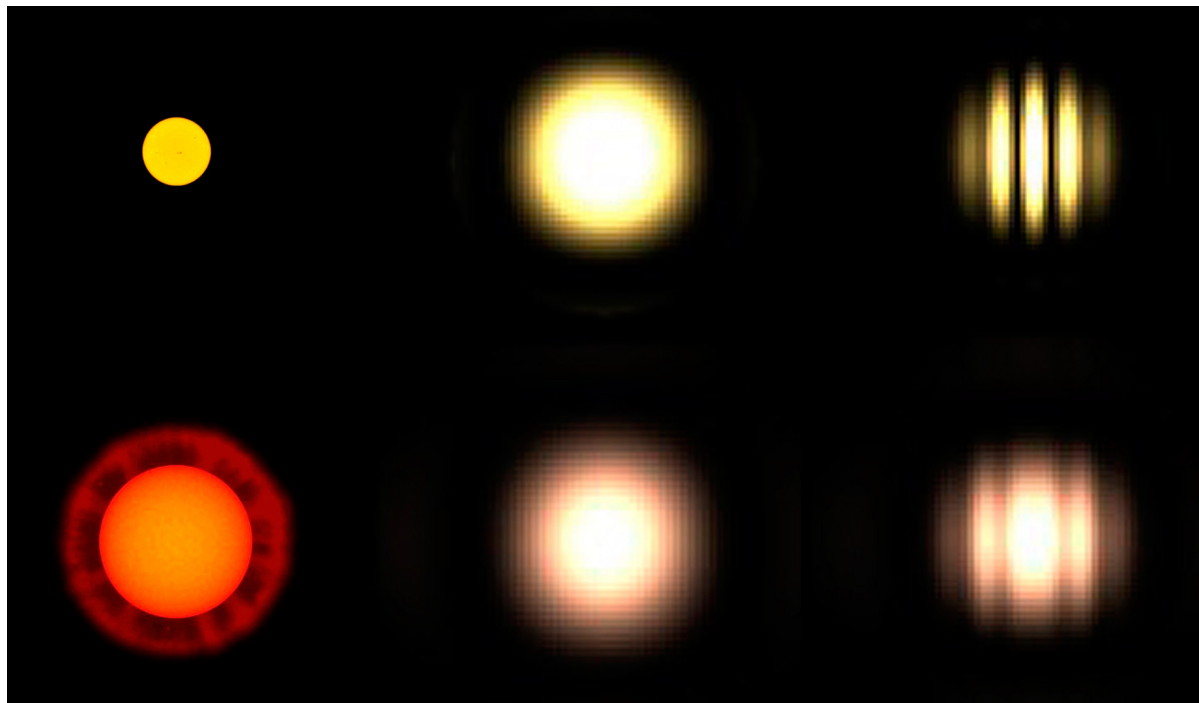


**Figure 3.2.:** Schematic of the images of two stars of different angular size (left) observed with a single telescope (middle) and with an interferometer like the VLTI (right).  
**Credit:** ESO <https://www.eso.org/public/images/eso0111d/>

### 3.1.2. Van Cittert-Zernike Theorem

The fringe pattern obtained with an interferometer as described in the section before, can be thought of similarly to the interference pattern given by a double slit experiment (Figure 3.3). The *fringe visibility* of a sinusoidal fringe pattern is defined by the intensities at the maximum and minimum of the fringe,  $I_{\max}$  and  $I_{\min}$ , respectively[15], and is given by:

$$V = \frac{I_{\max} - I_{\min}}{I_{\max} + I_{\min}} \quad (3.10)$$

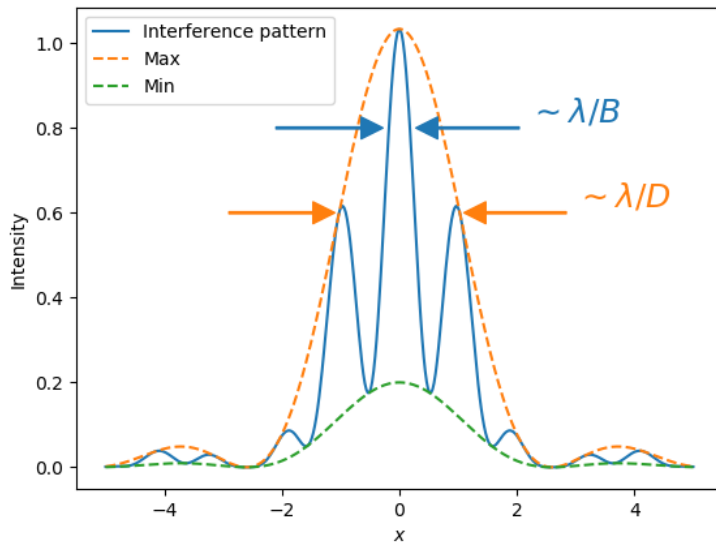


**Figure 3.3.:** Visibility in interferometer can be considered similar to that of the double-slit experiment. However the max and min are varying across the interference pattern in contrast to Michelson interference. The fringe width depends on  $\lambda/B$ , while the envelope (Max) depends on the diameter  $D$  of the telescope antenna ( $\lambda/D$ ). The example shows a visibility of 70% or 0.7 according to formula (3.10)

The visibility takes values between 0 and 1, taking a value of 1 for a large interference contrast, or a large relative coherence between beams and a value of 0 for no contrast or no coherence.

The wave patterns obtained in astronomical interferometry are more complex. Given that the extents of the observation region are much smaller than the distance

from the observer, and therefore only small angles are involved, the Van-Cittert-Zernike theorem can be applied ([15], [34]) to define the **complex visibility**  $\mu$ . The **Van-Cittert / Zernike theorem** states that the complex visibility  $\mu$ , for a non-coherent and almost monochromatic extended source is the normalised Fourier Transform ( $\mathcal{FT}$ ) of the brightness distribution ( $I(x, y)$ ):

$$\mu(\mathbf{b}, \lambda) = \frac{\mathcal{FT}(I(x, y))}{\iint I(x, y)} \quad (3.11)$$

In terms of the brightness distribution profile  $I(x, y)$  of the source, the complex visibility can be expressed in terms of spatial frequency as:

$$\mu(u, v) = \frac{\iint_{-\infty}^{\infty} I(x, y) e^{2\pi i(ux+vy)} dx dy}{\iint_{-\infty}^{\infty} I(x, y) dx dy}, \quad (3.12)$$

$$\text{where } u = \frac{b_x}{\lambda}, v = \frac{b_y}{\lambda}, b_x = b \cos(\theta), b_y = b \sin(\theta).^{14}$$

**Visibility** is given by the modulus of the complex value in equation (3.12):

$$V(u, v) = \|\mu(u, v)\|, \quad (3.13)$$

and the phase of the visibility is  $\phi(u, v) = \arg(\mu(u, v))$ . For a known intensity distribution one can calculate the corresponding visibility and phase. For simple cases this can be done analytically. In practice one observes the interference pattern, from which a visibility is calculated and, with sufficiently many probes in the  $uv$ -space the brightness distribution of the source can be deduced through inverse Fourier transforms. This implies the source should be probed over a large span of baselines or wavelengths.

Probing multiple baselines can be achieved by using multiple telescopes, by probing over a long period of time such that Earth's rotation causes a change in the observing angle  $\theta$  and the telescope coordinates describe an ellipse in the  $uv$ -plane, or by taking multiple observations from telescopes whose baselines are not fixed and have been changed between observations (Figure 3.4). The last category is however sensitive to changes in the observed object, given that observations cannot be done immediately for different baselines.

---

<sup>14</sup> $\theta$  is the position angle of the observation

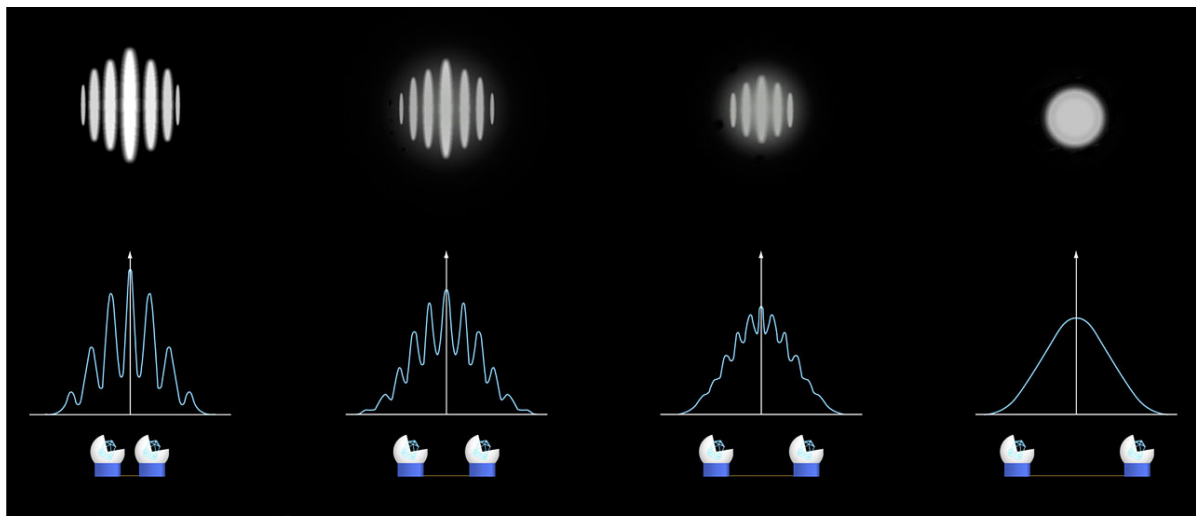


**Figure 3.4.:** Interferometric observations of a single star are shown, as the distance between the two telescopes is gradually increased. The observed pattern at the focal plane clearly changes, and the "fringes" disappear completely. As the fringes become less distinguishable (from left to right), the more the visibility  $V$  decreases, going to 0 in the last capture. **Credit:** ESO <https://www.eso.org/public/images/eso0111e/>

### 3.1.3. Instruments

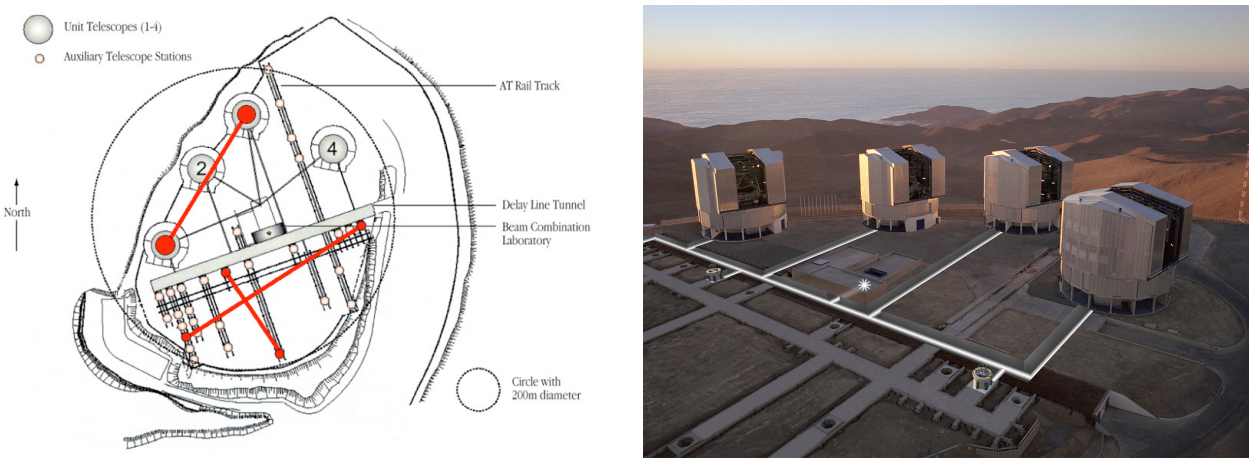
A number of observing instruments are available, a short summary of which is presented in Table 3.1. The instruments vary in baseline and wavelength capabilities, achieving a maximum baseline of 200 m (MATISSE and MIDI), and being able to probe in the near-IR and mid-IR, the regions where hot and warm dust, such as that present in circumstellar disks, emit. The VLTI instruments present the most interest, both in capabilities as well as in data availability.

Name	Number of Telescopes	Diameter [m]	Maximum baseline	$\lambda$
Keck I	2	10	85	NIR, MIR
VLTI/MIDI	2/2	8/1.8	130 / 200	MIR
VLTI/PIONIER	4	8/1.8	130 / 200	NIR
VLTI/MATISSE	4	8/1.8	200	NIR, MIR
VLTI/AMBER	3	8/1.8	140	NIR
ALMA	66	12	16 000	radio

**Table 3.1.:** List of interferometric instruments

## VLTI

The VLT (Very Large Telescope) is a European project and part of the ESO<sup>15</sup>, located at the Paranal Observatory, in Chile (Figure 3.5). The **Very Large Telescope Interferometer** (VLTI) consists of the coherent combination of all the available telescopes at the VLT: 4 unit telescopes (UT), with a diameter of 8 m, and 4 smaller telescopes, called auxiliary telescopes (AT) with a diameter of 1.8 m. The telescopes can all be arranged in different configurations to serve several instruments. The maximum distance between telescopes, and therefore the maximum baseline is 200 m.



(a) View of the Paranal platform with the three baselines used for the VLTI observations highlighted in red.<sup>16</sup>

(b) Aerial view, with the four UTs shown, and three of the ATs and paths of the light beams (white) superimposed on the photo.<sup>17</sup>

**Figure 3.5.:** VLT, Cerro Paranal, Atacama Desert, Chile

## MIDI

The MID-Infrared Interferometric instrument (MIDI) was an instrument at the VLTI for interferometric observations in the N band ( $8 - 13 \mu\text{m}$ ) with a spatial resolution of 20 milliarcsec, which has been in operation between 2002 and 2015 [27]. It could combine the optical paths from either two UTs or two ATs with each other. Due to its good resolution and the N band<sup>18</sup> sensitivity, which allows warm dust at about 300 K

<sup>15</sup>European Southern Observatory

<sup>16</sup>Credit: ESO <https://www.eso.org/public/images/eso0432b/>

<sup>17</sup>Credit: ESO <https://www.eso.org/public/images/eso0111f/>

<sup>18</sup>see Appendix A, table A.1, for a reference to the wavelengths included in all the mentioned bands

to be spotted, MIDI has allowed for the detection of Seyfert galaxies [12] and the detection of gaps in circumstellar disks [33], to name a few examples.

## MATISSE

The successor of MIDI, the Multi AperTure mid-Infrared SpectroScopic Experiment, in short MATISSE, combines, not just two, but four telescopes – meaning the visibility can be measured concurrently for six different baselines. In addition to the N band, with MATISSE, observations can be made simultaneously in the L and M band ( $2.8 - 4.0 \mu\text{m}$  and  $4.6 - 5.0 \mu\text{m}$ ). Besides the observed emission, the scattered radiation from the star can also be observed. The smaller wavelengths also lead to a better resolution: at  $2.8 \mu\text{m}$  it is about 2 milliarcsec, or at a distance of 140 pc, the resolution is about 0.3 AU.

Errors in absolute visibility for different setups with the instruments used by MATISSE [32] are presented in Table 3.2.

	R = 30				R = 500			
	UT		AT		UT		AT	
	-FT	+FT	-FT	+FT	-FT	+FT	-FT	+FT
<b>L band</b>	0.017	0.016	0.023	0.025	/	0.023	0.023	0.025
<b>M band</b>	0.013	0.011	0.015	0.017	/	0.029	0.016	0.017
<b>N band</b>	0.086	0.083	0.028	0.012	0.271	0.258	0.032	0.017

**Table 3.2.:** Calibrated measurement accuracies for the **Absolute Visibility** with MATISSE for a 20 Jy source. +FT = with Fringe Tracker, -FT= without Fringe Tracking technology, R = spectral resolution

### 3.2. Method

As discussed in the previous sections, the scenario to be reproduced is that of the visibility observations of a circularly symmetric dust disk, detected in the NIR and MIR. With long-baseline interferometry, an interference pattern is observed, from which a single value for the visibility is obtained. As the visibility is the Fourier Transform of the object, if sufficient visibilities are observed at different baselines and wavelengths, the Inverse Fourier Transform can be applied on the visibility function and the object can be reconstructed (see Figure 3.6).

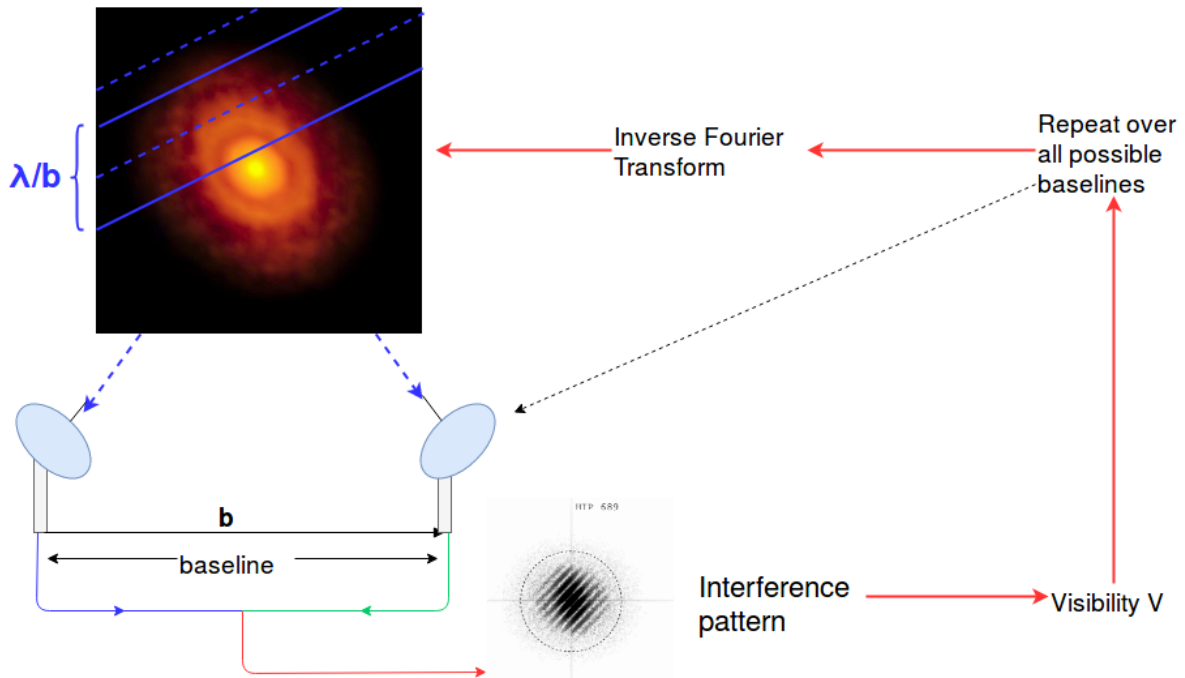
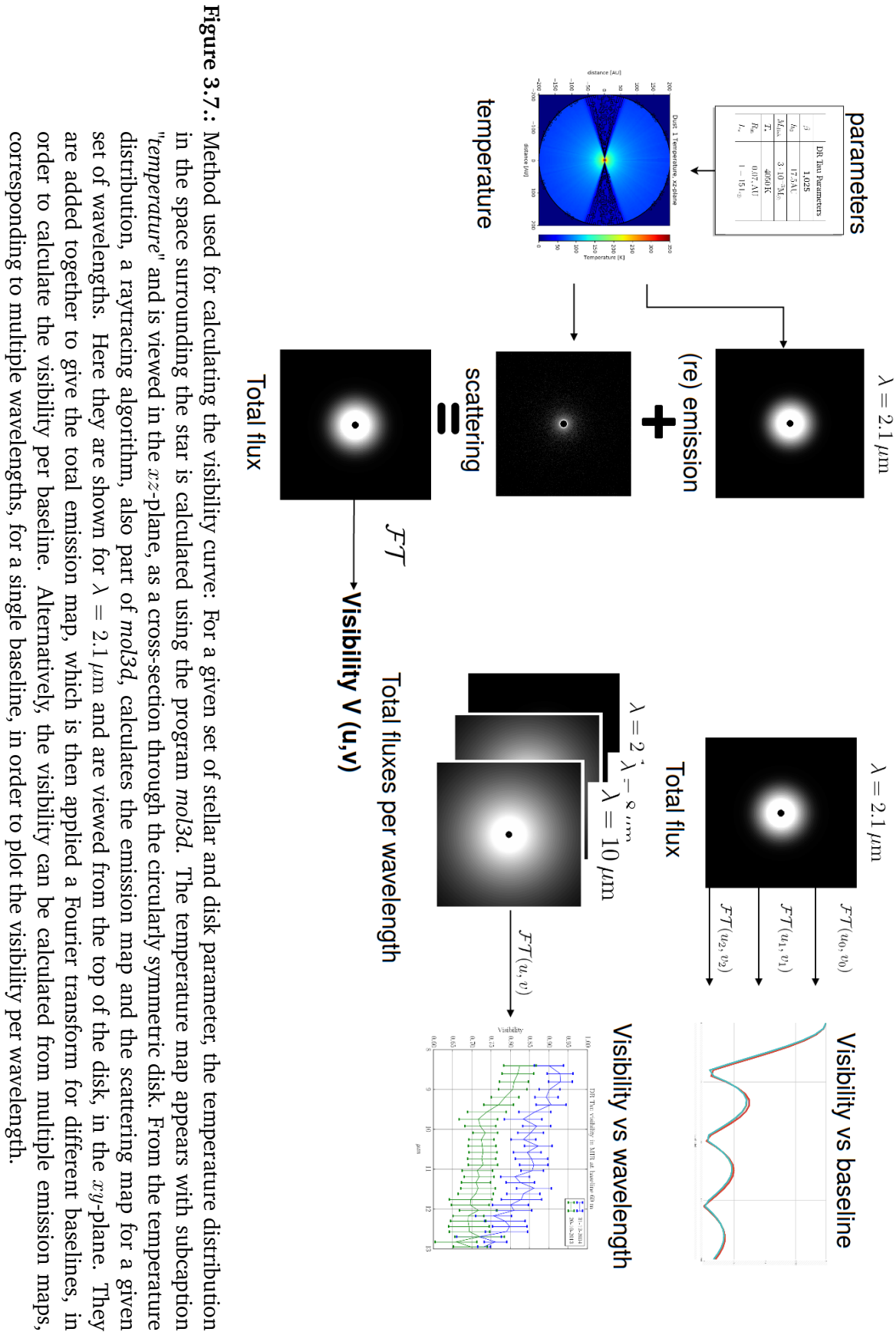


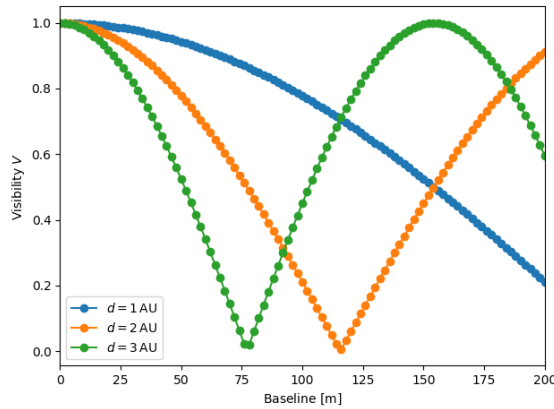
**Figure 3.6.:** Schematic: The observed object produces an interference pattern for one baseline and one wavelength. This interference pattern corresponds to one visibility value. By probing over the entire wavelength and baseline space, sufficient visibility values can be obtained in order to get a clear image of the original object through the inverse Fourier transform of the visibility. In reality, the baseline and wavelength domain which can be accessed by current telescopes are limited.

The method for calculating the visibility is schematically presented in Figure 3.7.

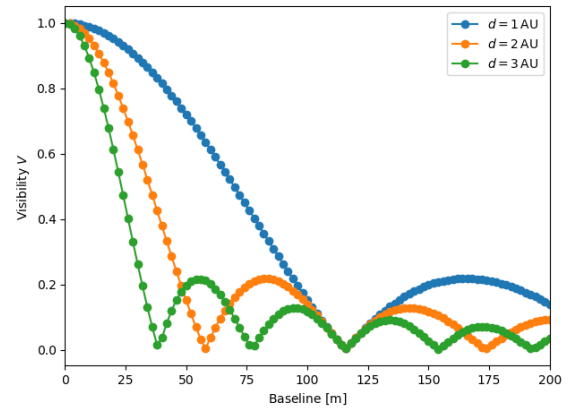


### 3.3. Results

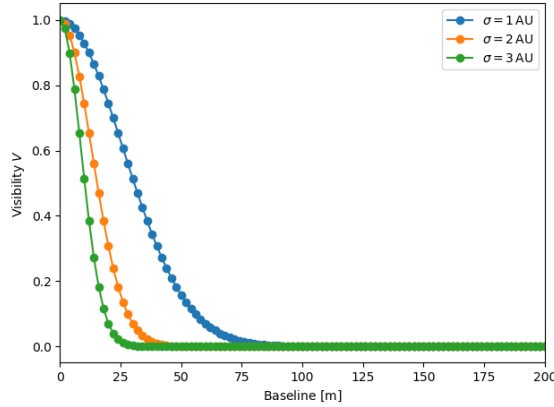
In this section the influence of various parameters on the visibility is investigated. First, the algorithm is tested against analytically deductible cases, presented in figure 3.8.



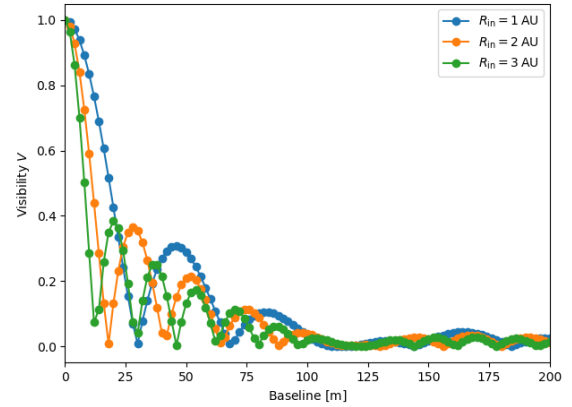
(a) Visibility for two point sources with equal brightness at distance  $d$  from one another.



(b) Visibility for a central box function (brightness is 1 inside the box and 0 elsewhere) for a central square box of side length  $a$ .



(c) Visibility for a central Gaussian brightness distribution with standard deviation  $\sigma$ .



(d) Visibility for a ring with inner radius  $R_{in}$  and a width of 1 AU.

**Figure 3.8.:** The Visibility curves calculated for different sources in a region of the sky corresponding to 0.3 arcsec at a distance of 140 pc for  $\lambda = 2 \mu\text{m}$ .

Consider the simple case of two point sources at distance  $d$  from one another, and set the origin of space at half of the distance between them, such that one source is located at  $-x_0 \propto -d/2$  and the second is located at  $x_0 \propto d/2$  ( $x_0$  is a transformation of  $d$  to a unit less coordinate). Assuming the sources have the same intensity, they can

then be expressed as delta functions  $\delta(-x_0)$  and  $\delta(x_0)$ , respectively. Using properties of the Fourier transform [21]

$$\mathcal{FT}[g + f] = \mathcal{FT}[g] + \mathcal{FT}[f] \quad (3.14)$$

the complex visibility is calculated to be

$$\mu(u) = \frac{\int e^{2\pi i u \delta(-x_0)} dx + \int e^{2\pi i u \delta(x_0)} dx}{2} = \frac{e^{-2\pi i ux_0} + e^{2\pi i ux_0}}{2} = \cos(2\pi ux_0) \quad (3.15)$$

$$V(u) = V(b, \lambda) = \left\| \cos \left( 2\pi \frac{b}{\lambda} x_0 \right) \right\| \quad (3.16)$$

The visibility then has the shape of the modulus of a cosine function. As the argument of the cosine is directly proportional to  $d$ , and inversely proportional to  $\lambda$ , the period (and the location of the first minimum) drops with an increase in  $d$  as observed in 3.8a and increases with an increase in  $\lambda$ .

The Fourier Transform of a box function is found to be proportional to a normalised *sinc* function, with similar behaviour in relation the the wavelength and the size  $a$  to the 2 point source, as seen in 3.8b.

For a Gaussian source, the visibility is also a Gaussian function, but with the new normal distribution proportional to  $\sigma^{-1}$  (equation (3.17)).

$$\mathcal{FT} \left[ e^{-\frac{x^2}{2\sigma^2}} \right] \propto e^{-\frac{x^2\sigma^2}{2}} \quad (3.17)$$

This implies the broader the distribution in space, the narrower it will appear in the visibility curves (3.8c).

For a simple disk

$$I(x, y) = I_0 \text{circ} \left( \frac{\sqrt{x^2 + y^2}}{R_{\text{disk}}} \right), \text{circ}(w < 1) = 1, \text{circ}(w > 1) = 0, \quad (3.18)$$

the visibility is a Bessel function of the first kind divided by the argument  $\propto J_1(u)/u$  [15], and for a ring a similar function is obtained 3.8d.

### 3.3.1. Parameter space

Having established what the visibility curves are expected to look like for different brightness distributions at a certain wavelength, the effect of various parameters on the curves is investigated. The parameter space investigated is presented in Table 3.3.

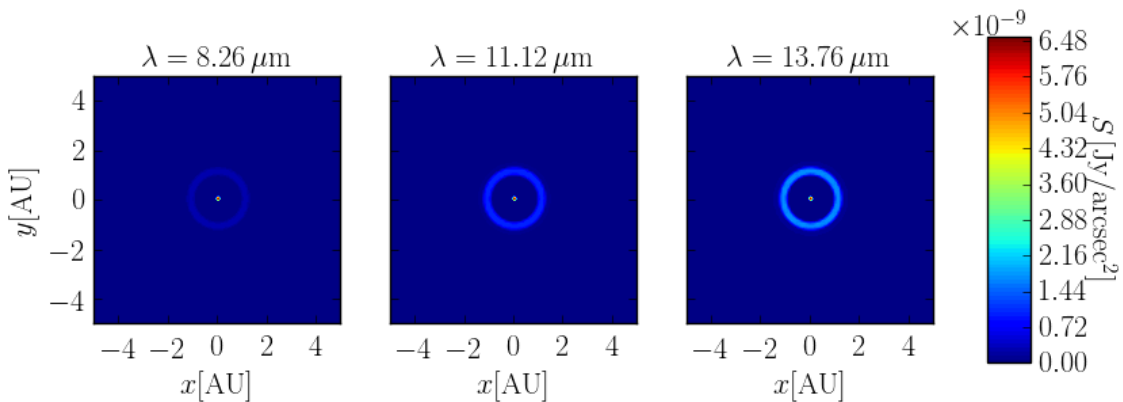
$\lambda$	2, 8 – 13 $\mu\text{m}$	$\Delta\lambda \approx 1 \mu\text{m}$
$R_{\text{in}}$	0.07, 0.5, 1 – 10 AU	$\Delta R_{\text{in}} = 1 \text{ AU}$
$T_{\text{eff}}$	3 500 – 9 000 K	$\Delta T = 500 \text{ K}$
$L_{\star}$	1 – 50 $L_{\odot}$	$\Delta L_{\star} = 5 L_{\odot}$

**Table 3.3.:** Parameter space

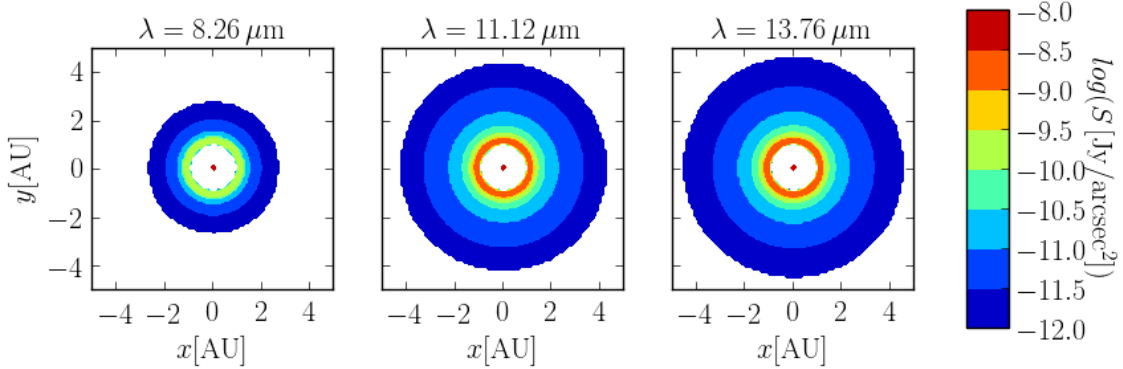
As the visibility curves are probed at different wavelengths for the same disk in the interval of 8 – 13  $\mu\text{m}$  the following things are expected:

- the first minimum point moves to a larger baseline as the wavelength increases;
- as the wavelength increases the ring becomes wider as the colder dust is located further away from the star than the hotter dust;
- because the ring is wider, the profile of the visibility is narrower for larger wavelengths in the interval;
- when probing at one baseline located before the first minimum the visibility appears to be increasing with wavelength.

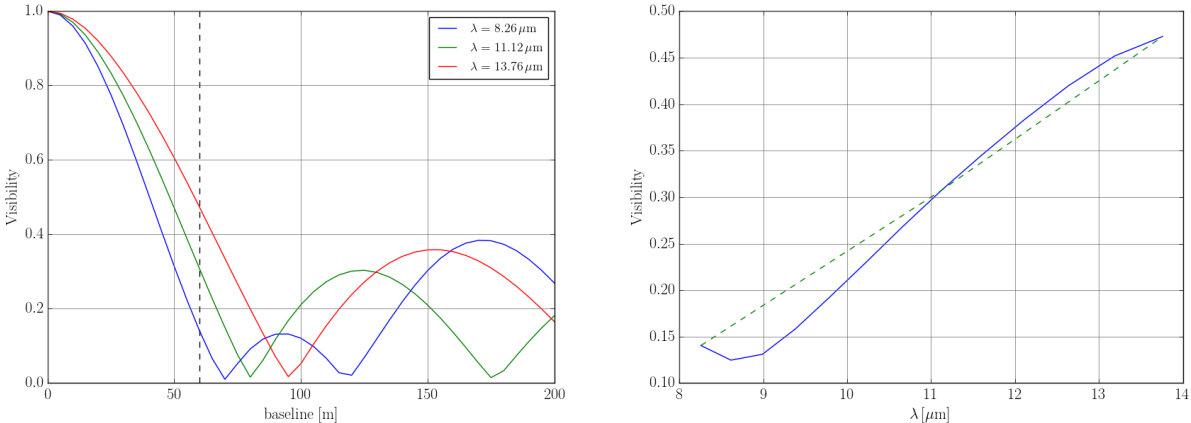
These effects are illustrated in Figure 3.9, where, for a star and circumstellar disk model at  $T_{\star} = 4500 \text{ K}$ ,  $L_{\star} = 1 L_{\odot}$ ,  $R_{\text{in}} = 3 \text{ AU}$ , the views corresponding to selected wavelengths in the N band are illustrated. Notable is that the central star is not visible in the logarithmic scale due the fact that it spreads over 1 pixel and the image is scaled down. In order to rectify this, the neighbouring pixels in each directions have been assigned the same value as the central one in the figures of 3.9b. Figure is a good reflection of the fact that knowing one distribution for a given wavelength does not directly infer the visibility at the immediately neighbouring wavelength.



(a) Brightness distribution for star with circumstellar disk at different wavelengths



(b) Brightness distribution from 3.9a in logarithmic scale, with a cut-off at  $10^{-13} \text{ Jy}/\text{arcsec}^2$ . The central star is a pixel and too faint to see.



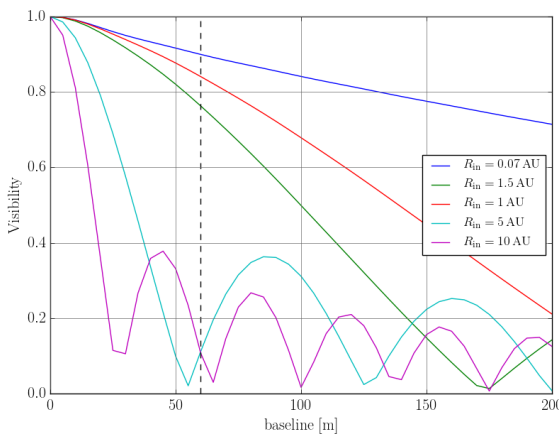
(c) Variation of visibility with baseline and wavelength. The dotted line marks the value for the baseline at  $b = 60\text{m}$

(d) Visibility corresponding to the same model plotted against the wavelength in the N band. The dotted green line represents the trendline given by the three probed values from 3.9c.

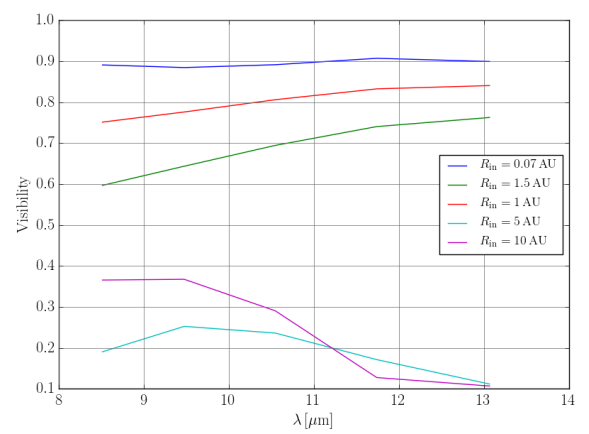
**Figure 3.9.:** Brightness distribution and visibility for circumstellar disk simulation with  $T_\star = 4500 \text{ K}$ ,  $L_\star = 1 L_\odot$ ,  $R_{\text{in}} = 3 \text{ AU}$

### 3.3.2. $R_{\text{in}}$ variation

As already presented at the beginning of the current section 3.3, and deduced in the previous section 3.1.2 through the Van-Cittert-Zernike theorem, the geometry of the brightness distribution and its size plays a definitive role in the final shape and values of the visibility curves. For a given frequency, the changes with  $R_{\text{in}}$  are predictable in terms of the visibility shape and the position of the first zeros (Figure 3.10a). When probing a single baseline however, the trend of the visibility in the frequency domain clearly depends on the trend in baseline domain at the given point. If the baseline value probed lies after the first minimum (in the baseline domain) or near the second, the visibility curve in the N band has a variation around low values, in which little information about the original object is contained. As seen in figure 3.10b probing a circumstellar disk of  $R_{\text{in}} = 5$  AU in the N band with an interferometer set at a baseline of 60 m will not allow for the object to be definitely identified, as the values are smaller than the error for MATISSE within this band for a resolution  $R = 300$ . Though this behaviour appears often, the value of the visibility in the N band is not always increasing with frequency for dense circularly symmetric disks. Appart from the geometry, circumstellar disks with large inner radii are significantly cooler and with only the dust closest to the rim contributing, emission in the MIR drops significantly, causing the visibility in this region to drop as well.



(a) Visibility against baseline for different inner radii for the disk at  $\lambda = 13 \mu\text{m}$ .



(b) Visibility against wavelength in the N band for different inner radii.

**Figure 3.10.:** Brightness distribution and visibility for circumstellar disk simulation with  $T_{\star} = 4000 \text{ K}$ ,  $L_{\star} = 5 L_{\odot}$

### 3.3.3. Temperature variation

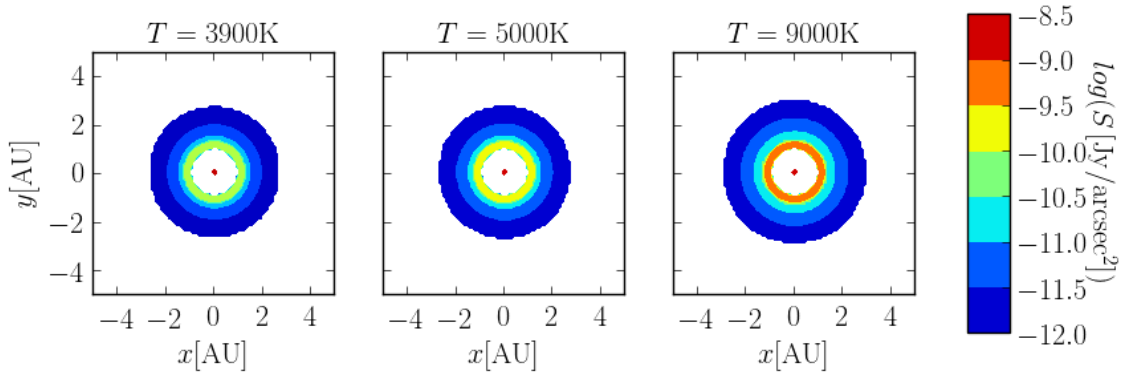
Changing the temperature of the central star would ultimately change the temperature distribution in a protoplanetary disk and the extent of emission for certain wavelengths through the disk. Given that protoplanetary disks are large ( $R_{\text{out}} \sim 200$  AU) and dense, it is expected for the hot dust near the star to show the most variability and become detectable in the J, H, K and L - bands, while the warm dust at  $T = 300$  K, would most likely extend the distance from the star at which its found, but would not change its visibility at  $10 - 13 \mu\text{m}$  by an observable amount.

In the following figures 3.11 and 3.12 the luminosity of the central star is kept constant, at  $L_* = 1.0 L_\odot$ , while the effective temperature is varied. This implies according to the equation (2.21) that the radius of the star is changed in order for the luminosity to remain the same.

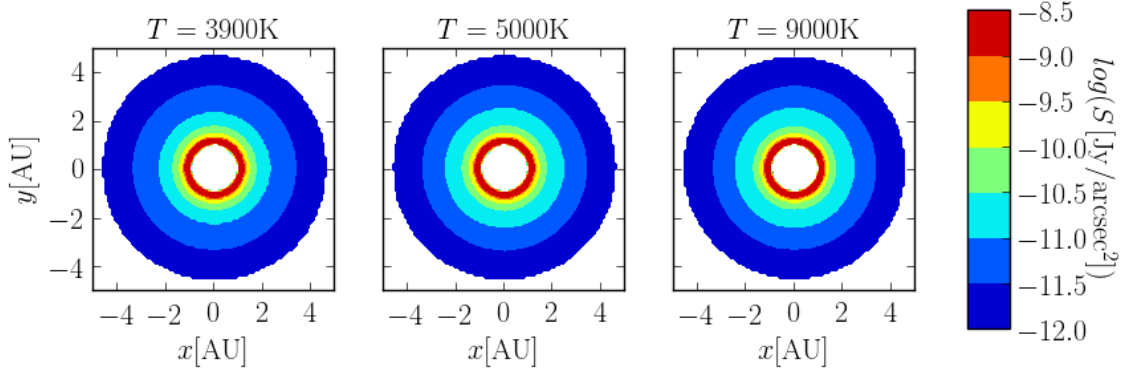
As expected, at the lower end of the N band ( $\sim 8 \mu\text{m}$ ) some changes are detectable with a dramatic increase in temperature (from 3 900 K to 9 000 K) as seen in Figure 3.11. This difference carries through to the visibility in Figure 3.12a, with the maximum change of 0.287 for a disk with inner radius  $R_{\text{in}} = 3$  AU at a baseline of 90 m, and a notable maximum change of 0.215 for a disk with inner radius  $R_{\text{in}} = 2$  AU at a baseline of 140 m. As the wavelengths increase (3.12c, 3.12e) the maximum of the absolute value variations in visibility with temperature are 0.063 at 120 m baseline,  $10.6 \mu\text{m}$  wavelength for  $R_{\text{in}} = 3$  AU and 0.018 at 195 m baseline,  $13.7 \mu\text{m}$  wavelength for  $R_{\text{in}} = 0.1$  AU.

The largest inner radius 3 AU has the highest variation for the smallest wavelength as the temperature difference influences the most this setup. The dust is heated to higher temperatures than possible with lower star temperatures, in contrary to a disk with inner radius 0.1 AU, which already had emission at this wavelength ( $\sim 8 \mu\text{m}$ ) from the hotter dust near the star.

The variations are generally lower than the measuring errors in the instruments and would not be detectable. The variation that could be detectable, at  $\sim 8 \mu\text{m}$ , is however a very unlikely case of an extreme change in temperature in a star, which would be more easily detected in the spectra of the star. All the changes show directly a change in the temperature distribution of the disk, through heating caused by the increase in energy of the central star.

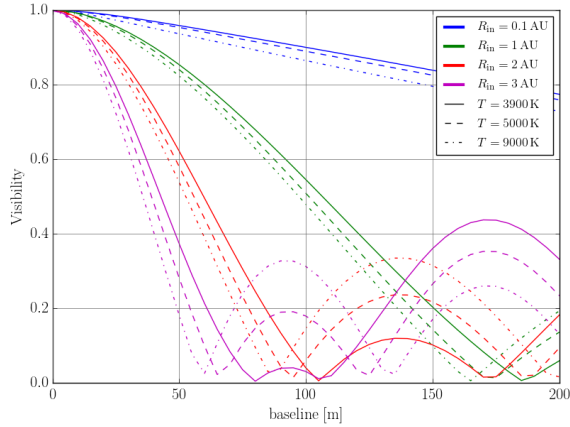


**(a)** Brightness distribution in logarithmic scale for circumstellar disks surrounding stars of different temperatures at  $\lambda = 8.2\mu\text{m}$ . The hot dust is more noticeable in the hottest star (right) as expected.

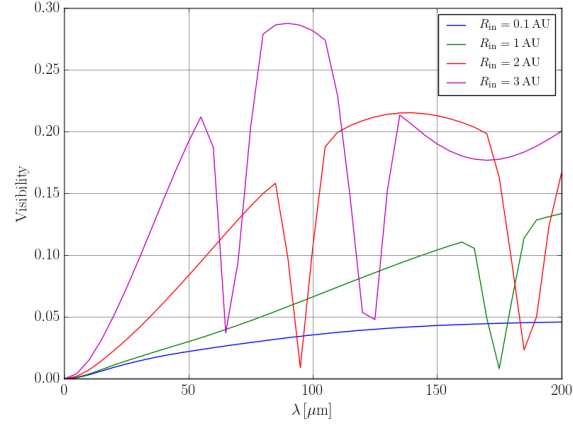


**(b)** Brightness distribution in logarithmic scale for circumstellar disks surrounding stars of different temperatures at  $\lambda = 13.76\mu\text{m}$ . At this frequency differences in the brightness distribution for different central star temperatures are indistinguishable.

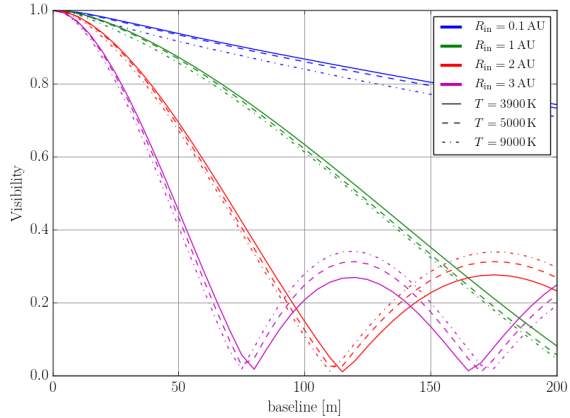
**Figure 3.11.:** Brightness distribution for stars with different temperatures ( $T = 3900\text{ K}$ ,  $T = 5000\text{ K}$ ,  $T = 9000\text{ K}$  from left to right) with luminosity  $L = 1L_\odot$  and a disk of inner radius  $R_{\text{disk}} = 1\text{ AU}$



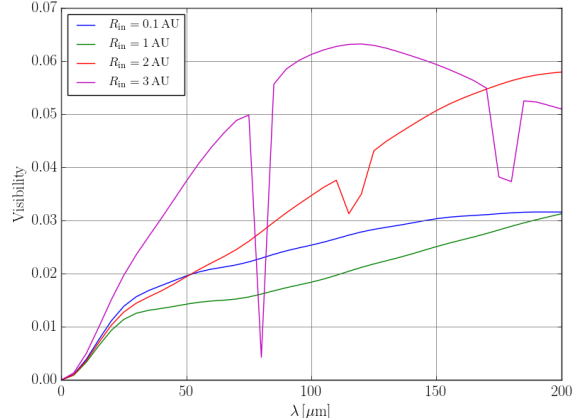
**(a)** Visibility against baseline at  $\lambda = 8.2 \mu\text{m}$ . Radii are differentiated through colour and temperatures through linestyle.



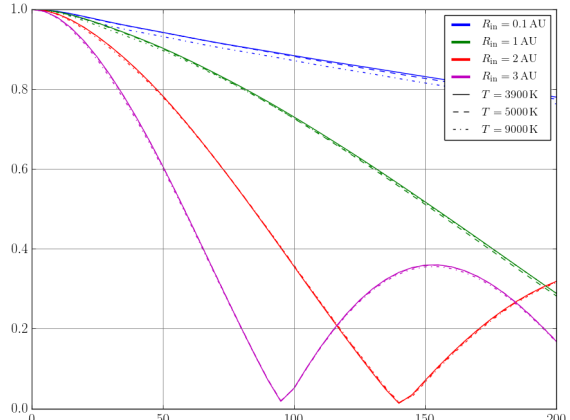
**(b)** Absolute visibility difference between  $T = 3900 \text{ K}$  and  $T = 9000 \text{ K}$  against baseline for each inner radius at  $\lambda = 8.36 \mu\text{m}$



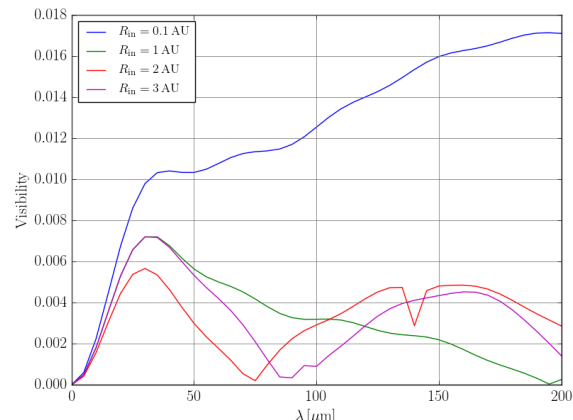
**(c)** Visibility against baseline at  $\lambda = 10.6 \mu\text{m}$ . Radii are differentiated through colour and temperatures through linestyle.



**(d)** Absolute visibility difference between  $T = 3900 \text{ K}$  and  $T = 9000 \text{ K}$  against baseline for each inner radius at  $\lambda = 10.6 \mu\text{m}$



**(e)** Visibility against baseline at  $\lambda = 13.7 \mu\text{m}$ . Radii are differentiated through colour and temperatures through linestyle.



**(f)** Absolute visibility difference between  $T = 3900 \text{ K}$  and  $T = 9000 \text{ K}$  against baseline for each inner radius at  $\lambda = 13.7 \mu\text{m}$

**Figure 3.12.:** Brightness distribution and visibility for circumstellar disk simulation with  $T_\star = 4000 \text{ K}$ ,  $L_\star = 5 L_\odot$

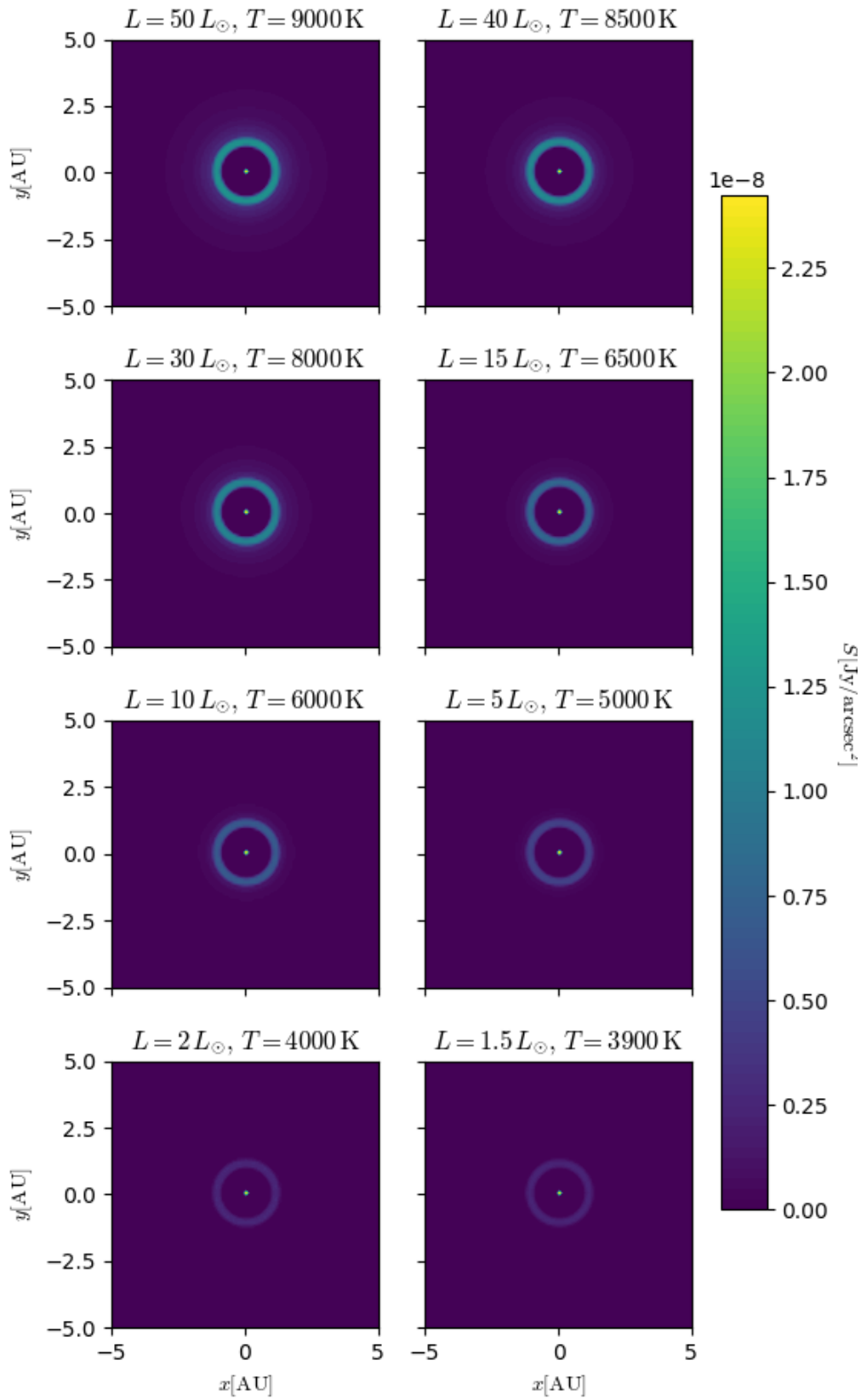
### 3.3.4. Temperature and luminosity variation

Consider a star with a fixed radius (with a small variation allowed:  $R_\star = 2.9 \pm 0.1 R_\odot$ ), whose temperature slowly decreases. In order for equation(2.21) to hold, the luminosity also decreases accordingly. The original star is set to the maximal parameters in the set considered:  $T_\star = 9\,000\text{ K}$  and  $L_\star = 50 L_\odot$ . Luminosity-temperature pairs are then formed from the available parameters such that the radius is constant within the aforementioned interval.

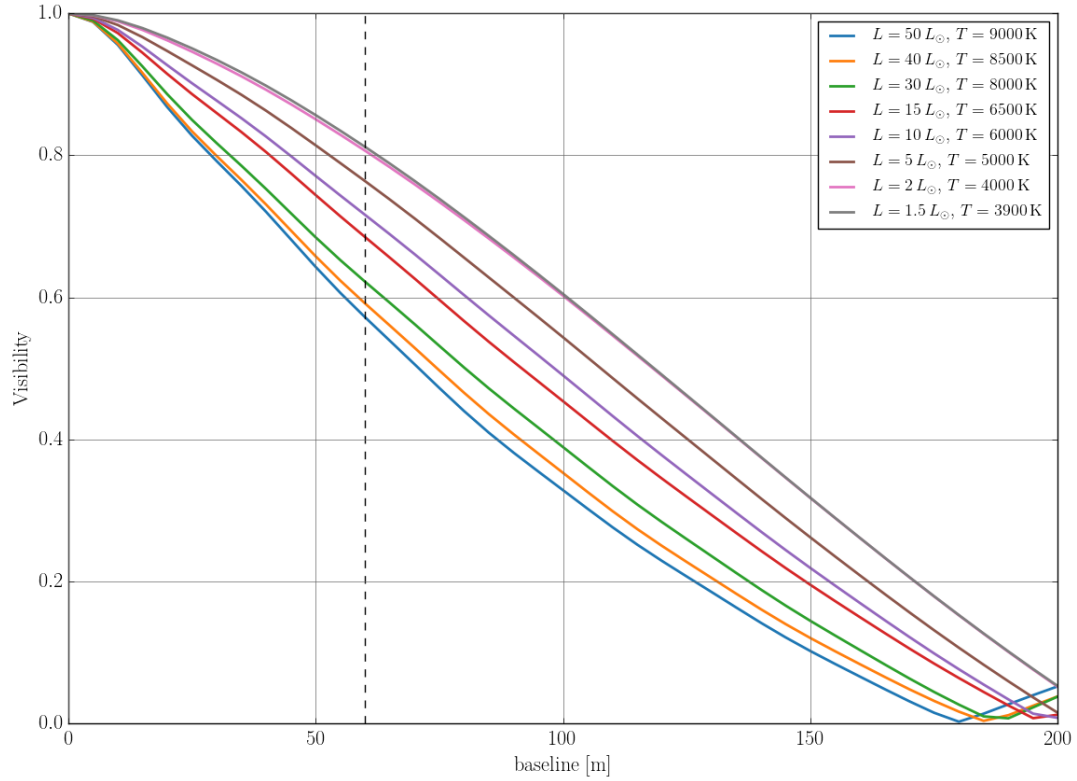
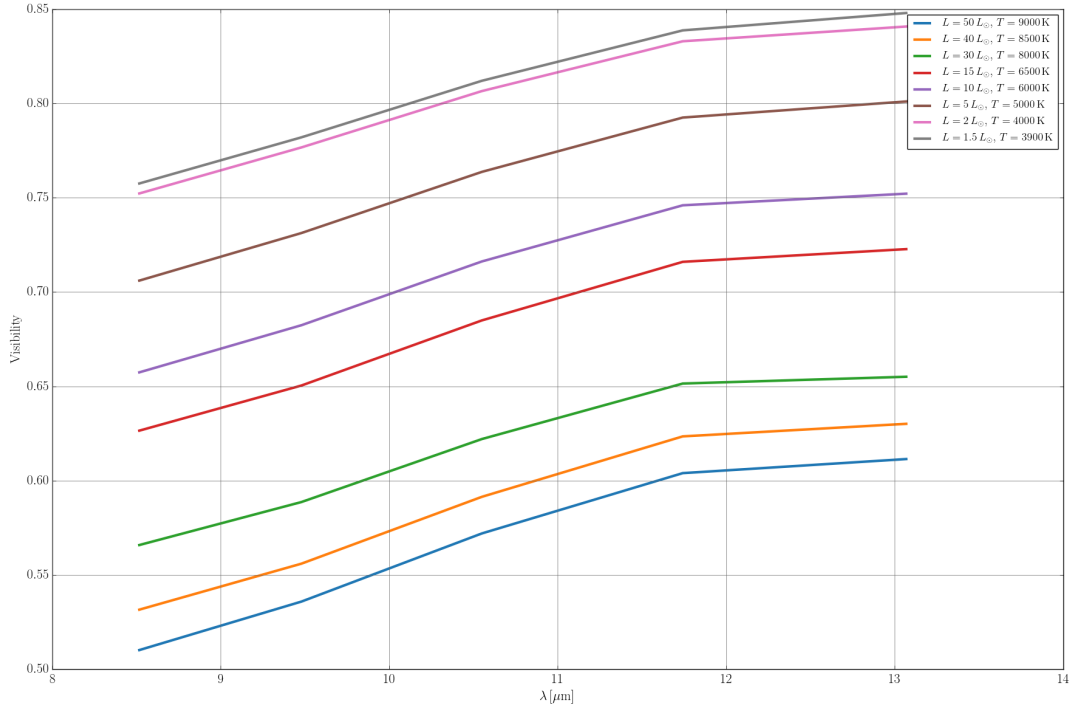
The variability of the visibility is noticeable even on the direct emission maps (Figure 3.16), as they clearly present larger maximum in the disk and a larger spread with larger temperatures and luminosities. With higher temperatures, the emission spectrum of the star contains high-energy photons which heat the dust, pushing the warm and cold dust further out than for lower temperatures of the star. With the increase in luminosity, the flux increases and the intensity of the light is able to counteract scattering more efficiently and reach greater optical depths in the disk.

This effect is reflected in the visibility curves, as they become wider with decreased luminosity and temperature (Figure 3.16a). The maximum absolute variation in visibility is 0.3 for a baseline of 105 m at  $\lambda = 13.1\text{ }\mu\text{m}$  between the two most extreme cases ( $T = 3\,900\text{ K}, L = 1.5 L_\odot$  to  $T = 9\,000\text{ K}, L = 50 L_\odot$ ). The average maximum variation in visibility between these cases across all wavelengths in Figure 3.16b is 0.28, while the average variation between them is 0.19.

While variations are measurable for the considered instruments, a large variation in temperature is an atypical physical model. Moreover the effect is visible at  $\sim 8\text{ }\mu\text{m}$  just as well as at  $13\text{ }\mu\text{m}$ , which was not found with the temperature variation alone. This is because, while the temperature heats the disk and increases the emission at lower frequencies, the luminosity increases re-emission at lower by penetrating further into the disk.



**Figure 3.13.:** Variation of brightness with luminosity and temperature at  $\lambda = 10.6 \mu\text{m}$ , for a disk with  $R_{\text{in}} = 1 \text{ AU}$ , and a star with  $R_* = 2.9 \pm 0.1 R_\odot$

(a) Visibility against baseline at  $\lambda = 10.6 \mu\text{m}$ 

(b) Visibility against wavelength

**Figure 3.14.:** Variation of visibility with luminosity and temperature for a disk with  $R_{\text{in}} = 1 \text{ AU}$ , and a star with  $R_{\star} = 2.9 \pm 0.1 R_{\odot}$

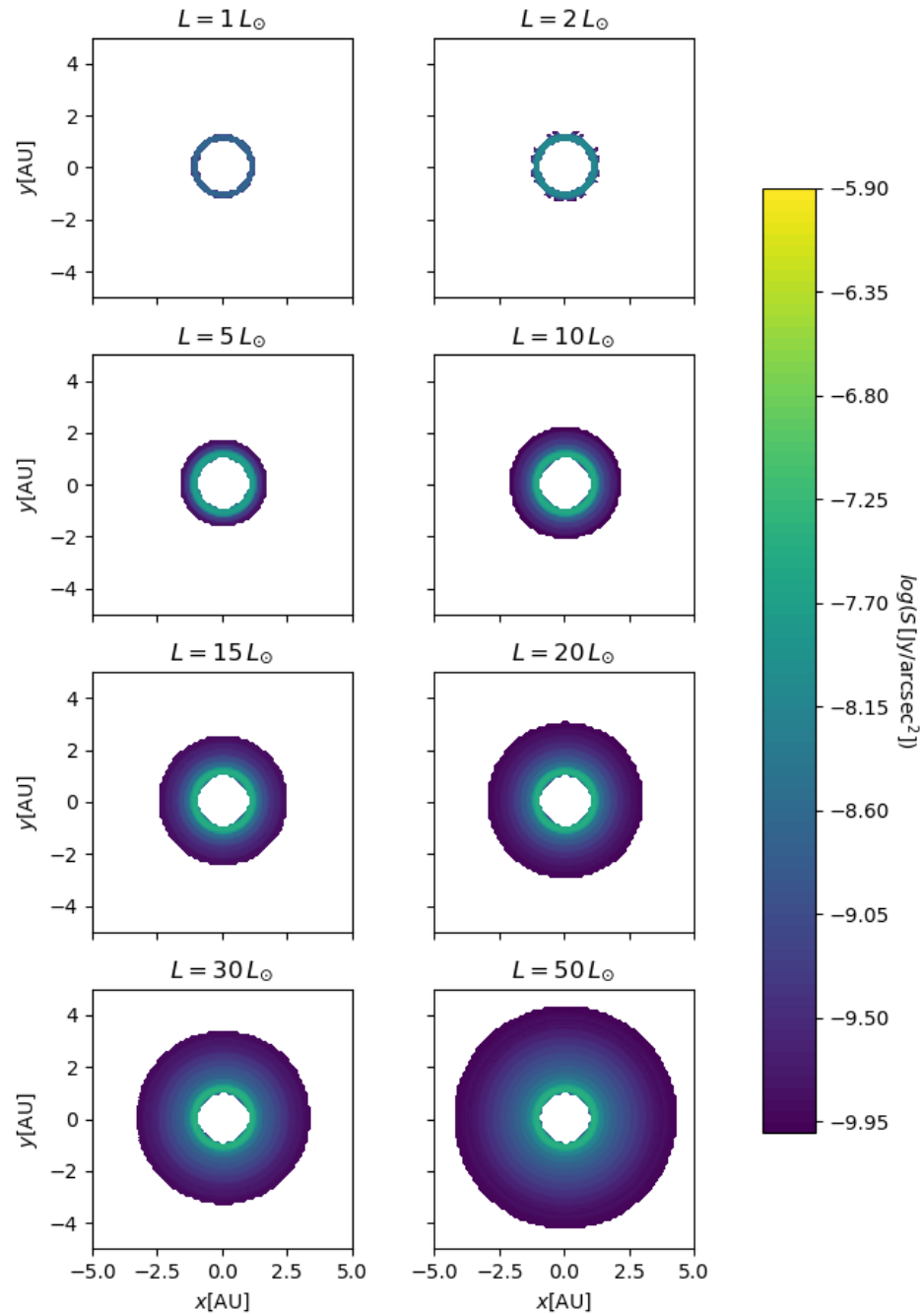
### 3.3.5. Luminosity variation

In the previous sections luminosity and temperature variations showed significant changes in the visibility values and visibility curves. While some similarly high variation was noticeable with temperature alone at a disk with the same inner radius ( $R_{\text{in}} = 1 \text{ AU}$ ), this was not uniform across the N band. The influence of the luminosity alone will now be investigated in the total variation in visibility. For this purpose, the temperature is kept constant, and the luminosity is modelled to vary as a consequence of the expansion of outer layers of the star, which keep their temperature, to a new outer radius. The expected effects are that, for a small inner radius, this change might be a significant enough distance reduction to the stellar surface to cause a temperature increase for the dust in the inner rim. The overall flux increases, causing a wider emission disk around the star, and consequently a narrower visibility curve.

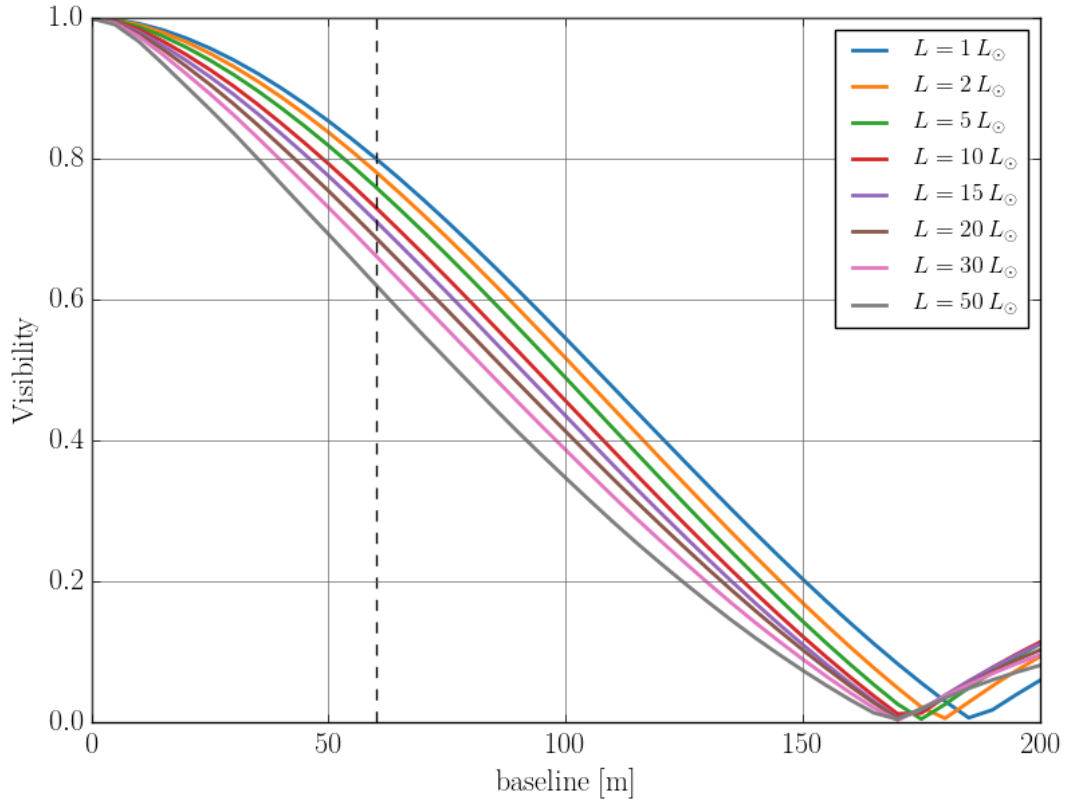
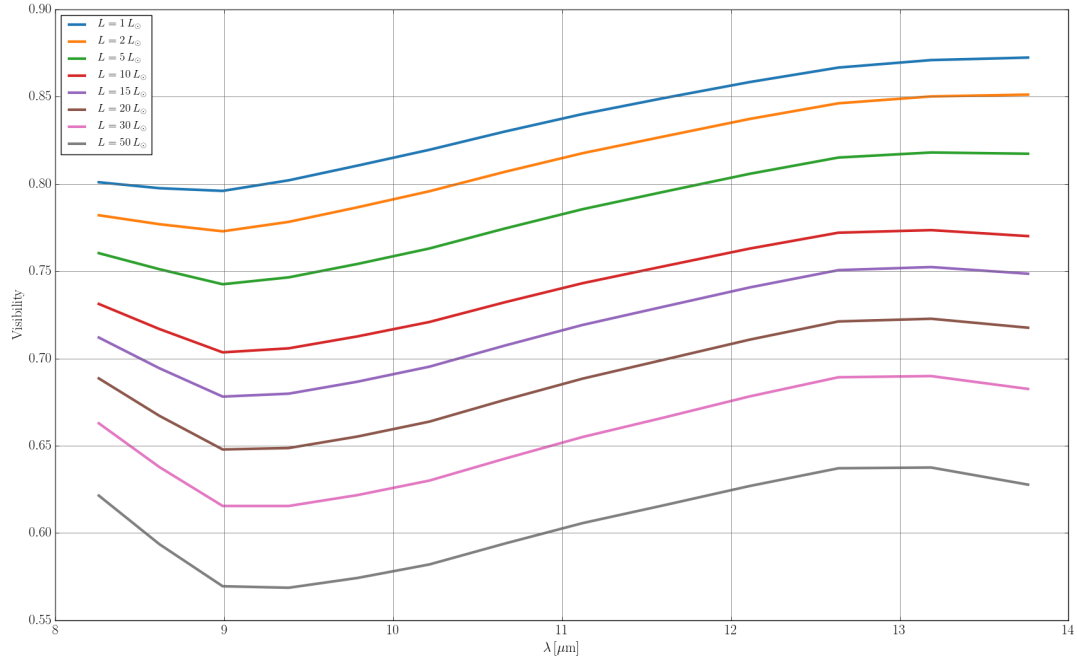
By setting a cut-off flux for the emission at different luminosities, the widening of the emission ring with luminosity is clearly noticeable in Figure 3.16 for  $8 \mu\text{m}$ . The other MIR wavelengths produce similar effects on the brightness distributions and are not included to avoid useless duplicates. This effect is seen as expected in narrowing of the shape of the visibility curve as presented in Figure 3.16a. An increase in luminosity, regardless the initial temperature of the star, will allow more photons to go further optical depths, by outnumbering scattering events, producing a broader emission area and narrowing the visibility in the Fourier domain (Figure

The actual values of the visibility variation depend on the pairing of baseline with the observed object. Considering all baselines and MIR wavelengths used in the simulations, as well as a subspace of the temperature and inner radii parameters an average and maximum variation are extracted in Table 3.4. The largest variation in the simulations run on the parameter space considered is that of 0.481 or 48.1% for a circumstellar disk with  $T_* = 5000 \text{ K}$ ,  $R_{\text{in}} = 0.1 \text{ AU}$  at  $\lambda = 13.76 \mu\text{m}$  with a fifty time luminosity increase. This phenomena is plausible, and definitely observable. Its observability depends however on the luminosity increase and the relation between the inner radius of the disk and the baseline and wavelength at which it is observed.

If the visibility is faint or the baseline is chosen poorly, the variation becomes non-observable.



**Figure 3.15.:** Variation of brightness with luminosity at  $\lambda = 8.2 \mu\text{m}$ , for a disk with  $R_{\text{in}} = 1 \text{ AU}$ , and a star with  $T_* = 3900 \text{ K}$ , cut-off value of  $5 \cdot 10^{-11} \text{ Jy/arcsec}^2$

(a) Visibility against baseline at  $\lambda = 10.5 \mu\text{m}$ (b) Visibility against wavelength at  $b = 60 \text{ m}$ 

**Figure 3.16.:** Variation of visibility with luminosity for a disk with  $R_{\text{in}} = 1 \text{ AU}$ , and a star with  $T_{\star} = 3900 \text{ K}$

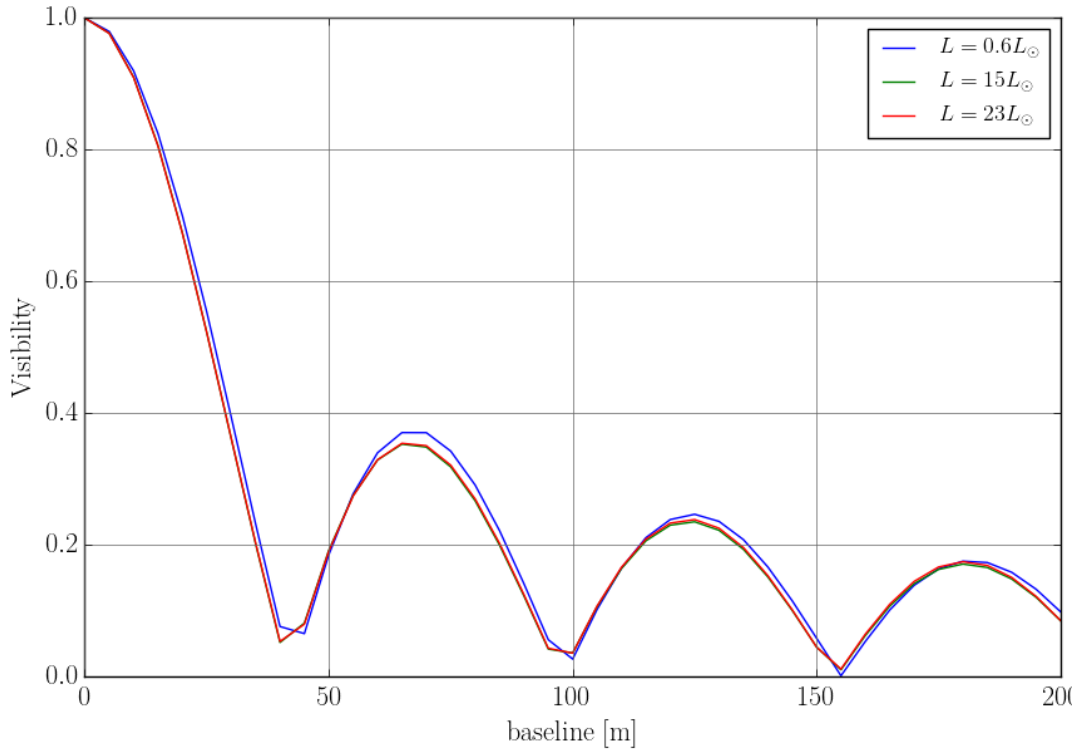
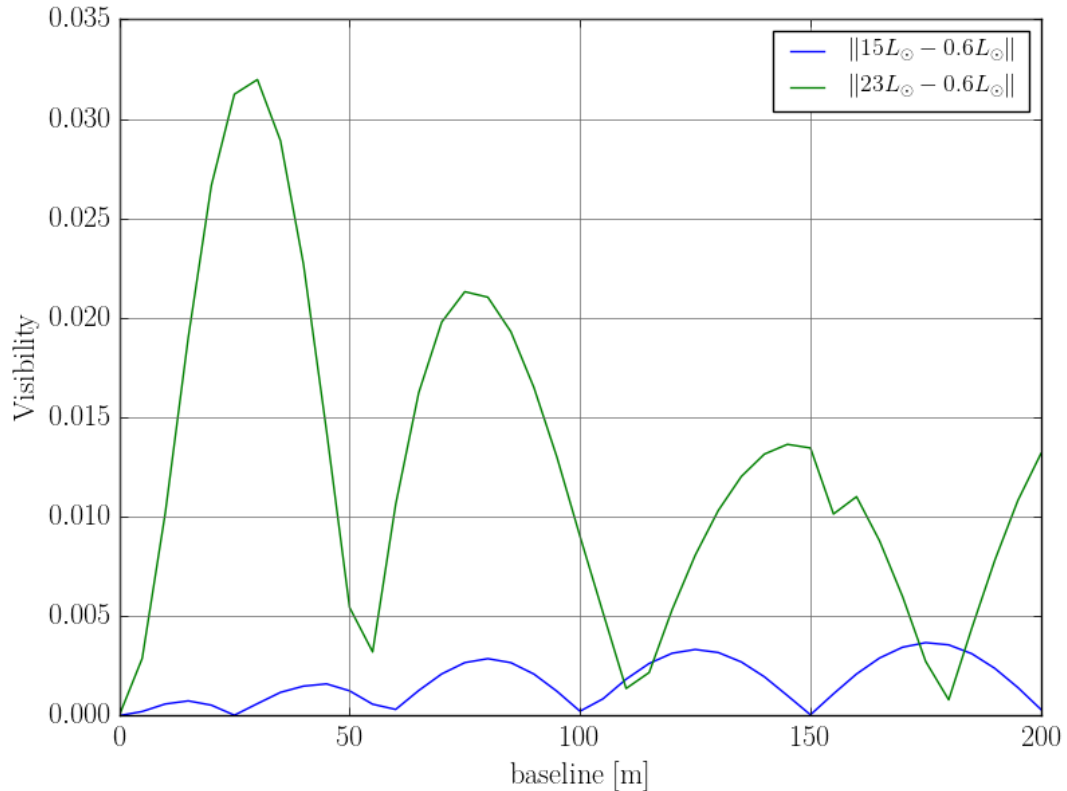
		$R_{\text{in}} = 0.1 \text{ AU}$	$R_{\text{in}} = 1 \text{ AU}$	$R_{\text{in}} = 2 \text{ AU}$	$R_{\text{in}} = 3 \text{ AU}$
$T = 3900 \text{ K}$	<b>avg</b>	0.415	0.268	0.189	0.154
	<b>max</b>	0.467	0.327	0.226	0.216
$T = 4500 \text{ K}$	<b>avg</b>	0.431	0.274	0.186	0.144
	<b>max</b>	0.469	0.324	0.222	0.166
$T = 5000 \text{ K}$	<b>avg</b>	0.436	0.268	0.179	0.147
	<b>max</b>	0.481	0.320	0.222	0.165
$T = 7000 \text{ K}$	<b>avg</b>	0.445	0.272	0.179	0.129
	<b>max</b>	0.466	0.327	0.221	0.160
$T = 9000 \text{ K}$	<b>avg</b>	0.437	0.271	0.167	0.118
	<b>max</b>	0.469	0.325	0.211	0.150

**Table 3.4.:** Visibility variation over the MIR (avg=average and max=maximum) for baselines in [0, 200] m for different temperatures and inner radii

### 3.3.6. Near Infrared

By successfully demonstrating an observable variability of the visibility of a circumstellar disk with the luminosity of the central star across the MIR range, one can wonder if this is observable for hotter dust in the NIR. The question arises as the instruments use can often make measurements in the NIR as well. For this an average T Tauri star is considered from the data table A.4 in Appendix A, with  $T_{\star} = 6300 \text{ K}$  and  $R_{\text{in}} = 1 \text{ AU}$ . A minimum, maximum and an in-between luminosity from the values in the data set are picked ( $L_{\text{min}} = 0.6 L_{\odot}$ ,  $L = 15 L_{\odot}$ ,  $L_{\text{max}} = 23 L_{\odot}$ ).

The resulting visibility at  $\lambda = 2.12 \mu\text{m}$  (Figure 3.17a) presents a slight variation for the 38.3 times increase in luminosity, and is indistinguishable for a smaller luminosity increase. The maximum variability of the visibility is 0.0382 in the most extreme case (between  $L_{\text{max}}$  and  $L_{\text{min}}$ ) and its average variability with baseline is in this case 0.004. This effect is not measurable, even with the small instrumental error in this band. Though scattering is stronger at this wavelength (than in the MIR), emission still dominates in the visibility calculations. The increase in luminosity changes the spread of the emission, but it is not as efficient against scattering.

(a) Visibility against baseline at  $\lambda = 2.12 \mu\text{m}$ (b) Difference in absolute visibility at  $\lambda = 2.12 \mu\text{m}$ 

**Figure 3.17.:** Variation of visibility with luminosity for a disk with  $R_{\text{in}} = 1 \text{ AU}$ , and a central star with  $T_{\star} = 6300 \text{ K}$

# Chapter 4.

## DR Tau

In this chapter an attempt is made to apply the methods and findings from chapter 3 to real observational data of a T Tauri object surrounded by a circumstellar disk. The candidate, DR Tau, shows a drop in visibility in measurements taken 9 years apart with the VLTI/MIDI instrument [10] for a baseline of  $\sim 60$  m. A circumstellar disk model was fitted for the data in the first epoch of observation [10], and the possibility of the visibility variation in the second epoch being caused by a change in luminosity is explored.

### 4.1. Introduction

DR Tau (Figure 4.1) is a classical T Tauri star located in the Taurus-Auriga complex, at a distance of about 140 pc ( $\alpha$  (J2000) = 04 : 47 : 06.2,  $\delta$  (J2000) = 16 : 58 : 43.05 [41]), which has been observed to be part of a 2-component system with a circumstellar disk.

DR Tau shows a high degree of variability, photometrically as well as spectroscopically ([24], [30]). Possible explanations include star spots, both hotter and cooler than the effective solar surface temperature, locally heating the circumstellar disk and causing an asymmetry in the brightness distribution coupled with the star rotation ([10]). Another common phenomena for YSO is the accretion of material from a circumstellar disk, which, through rapid and intermittent accretion events, generate thermal instabilities in the disk itself and, eventually, outburst phenomena [18].

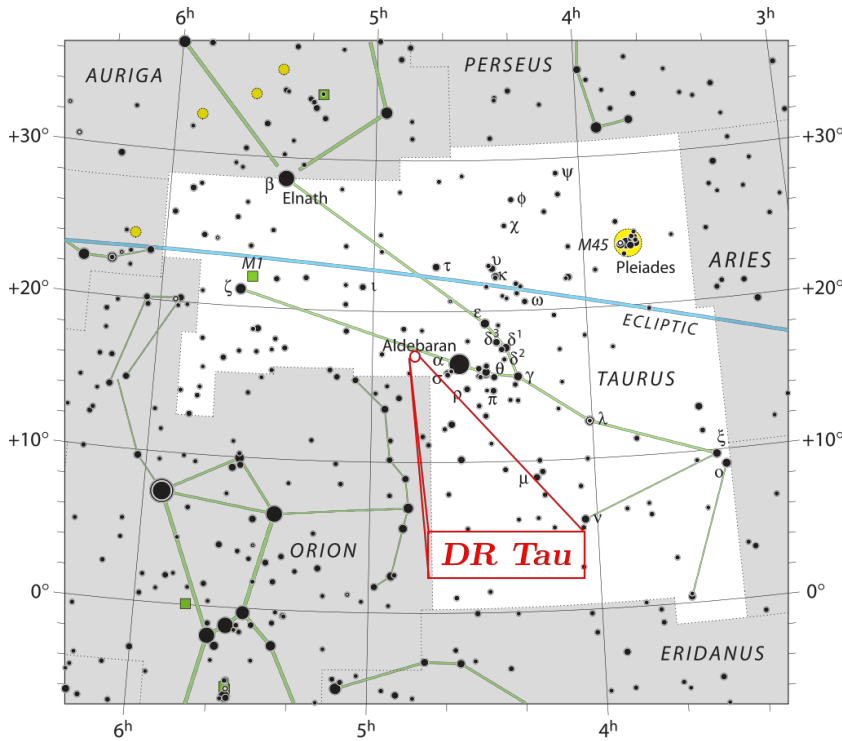


**Figure 4.1.:** Approximate position of DR Tau superposed on a starmap of the Taurus constellation. **Credit:** IAU and Sky & Telescope magazine

The multiple values for the parameters of the DR Tau-system suggested by the literature and gathered in table 4.1 may also be considered indication of the high variability of this system.

Parameter	Values	References
$T_\star$	3 917 K, 4 050 K, 4 060 K	[14], [10], [41]
$L_\star$	$1.09 L_\odot$ , $1.54 L_\odot$ , $2.5 L_\odot$ , $1.05 - 5 L_\odot$	[41], [43], [14], [41]
$R_\star$	$2.1 R_\odot$ , $3.44 R_\odot$	[41], [14]
$M_\star$	$0.75 M_\odot$ , $0.8 M_\odot$	[14], [41], [43], [41]
$M_{\text{disk}}$	$2 - 32 M_J$ , $19 M_J$ , $25.3 \pm 5.2 M_J^1$	[16], [2] [43]
$R_{\text{in}}$	0.065 AU, 3 AU	[10], [42]
$R_{\text{out}}$	75 – 275 AU	[41]

**Table 4.1.:** Properties of DR Tau from literature

## 4.2. Data

DR Tau was observed in three different epochs with the interferometric instrument MIDI at the VLTI. Out of these 2 observations at 9 years apart are considered: E1: *January 2005* and E3: *October 2013*. They have been picked because the observation baseline and angle are almost identical: E1 : baseline 60.7 m, 105.9°, E3 : baseline 60.6 m, 115.2°. The difference of just of 0.1 m in baseline and 9.3° in position angle for the observation angle should produce measurements for the visibility within the instrument error [10], however a drop in visibility of 0.15 or 15% on average is observed between the two epochs (Figure 4.2).

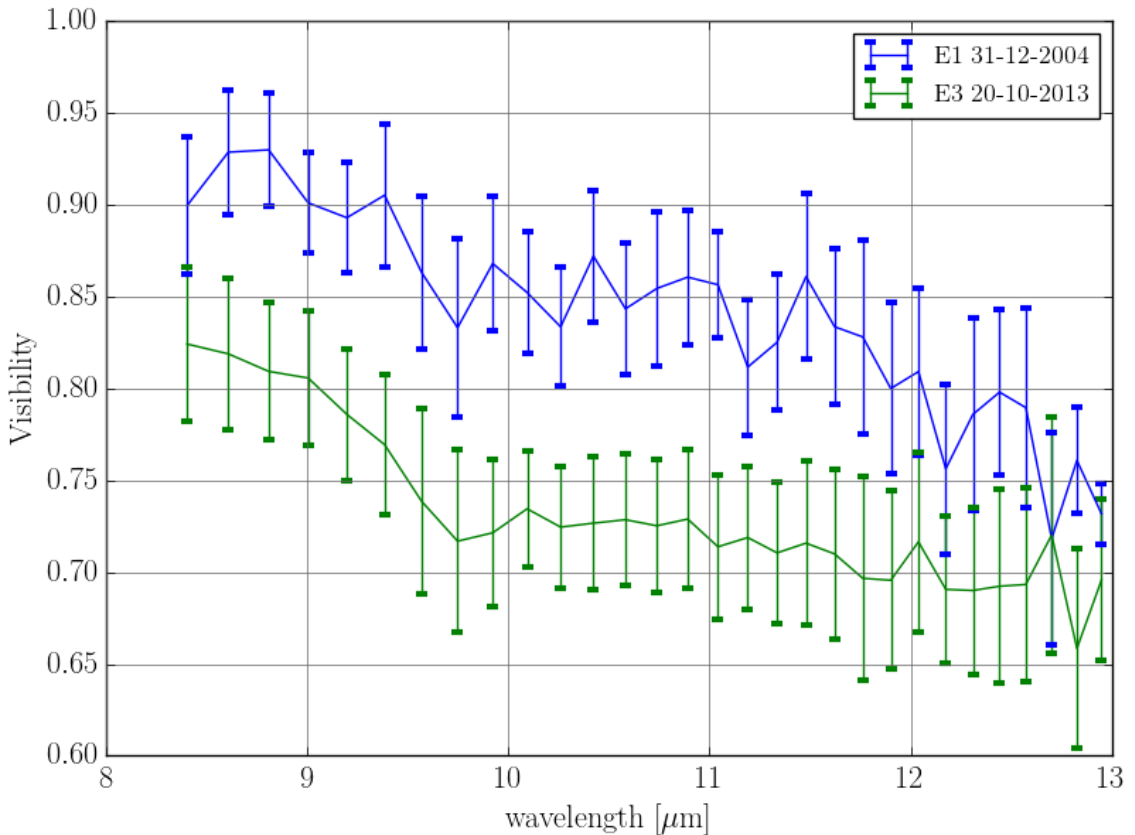


**Figure 4.2.:** Visibility of DR Tau in the MIR for 2 epochs 9 years apart with error bars

### 4.3. Model

Two models were suggested and implemented using *mc3d* [51]<sup>19</sup>, in [10] to account for the visibility observations in the two epochs investigated here: Model A for epoch E1, Model B for epoch E3 in Table 4.2. Model C is added as an alternative fit. As the base algorithm is the same, the result is expected to be obtainable with the method used in the previous chapter for calculating visibility. For each model the parameters are changed in the simulation code source (and an accretion source is added). The resulting temperature profile is calculated, and then the total emission maps for each wavelength are produced, from which the luminosity is computed for the baseline at 60 m. The luminosity is then varied for each of these models and a new simulation is produced in an attempt to best fit the data in Figure 4.2.

Parameter	Model A	Model B	Model C	Units
$L_\star$	0.9	0.9	1	$L_\odot$
$T_\star$	4050	4050	3900	K
$L_{\text{accr}}$	1.0	1.0	/	$L_\odot$
$T_{\text{accr}}$	8000	8000	/	K
$M_{\text{disk}}$	$3 \cdot 10^{-3}$	$3 \cdot 10^{-3}$	$1 \cdot 10^{-5}$	$M_\odot$
$R_{\text{in}}$	0.065	0.065	0.1	AU
$R_{\text{out}}$	90	350	200	AU
$h_0$	17.5	10	10	AU
$\alpha$	1.605	1.605	2.625	/
$\beta$	1.025	1.025	1.125	/
inclination $i$	44	15	1	°
orientation $\Phi$	75	15	0	°

**Table 4.2.:** Models for DR Tau fit as continuous flared circumstellar disk

---

<sup>19</sup>*mc3d* is a precursor of the programm used here, *mol3d*, which is based on the same principles of radiative transfer

## 4.4. Results

The results are presented in Figure 4.3. No model is found to fit the actual observed data within error. Model C is chosen to reflect the overall drop in visibility for increased luminosity, having an average drop of 0.159 and a maximum one of 0.178 at  $\lambda = 9.38 \mu\text{m}$ . This is the closest of the three to the average drop of 0.15 in the data for DR Tau. Furthermore the overall shape of the curve is preserved with the drop in visibility, which can also be seen in the data, even if the shapes are in essence different. Model A is the second closest, with an average drop of 0.138. Model B has the worst fit, despite the similar slope with the original data, while Model A, with an increase in luminosity from  $0.9 L_\odot$  to  $4 L_\odot$  presents the best fit as seen in Table 4.3.

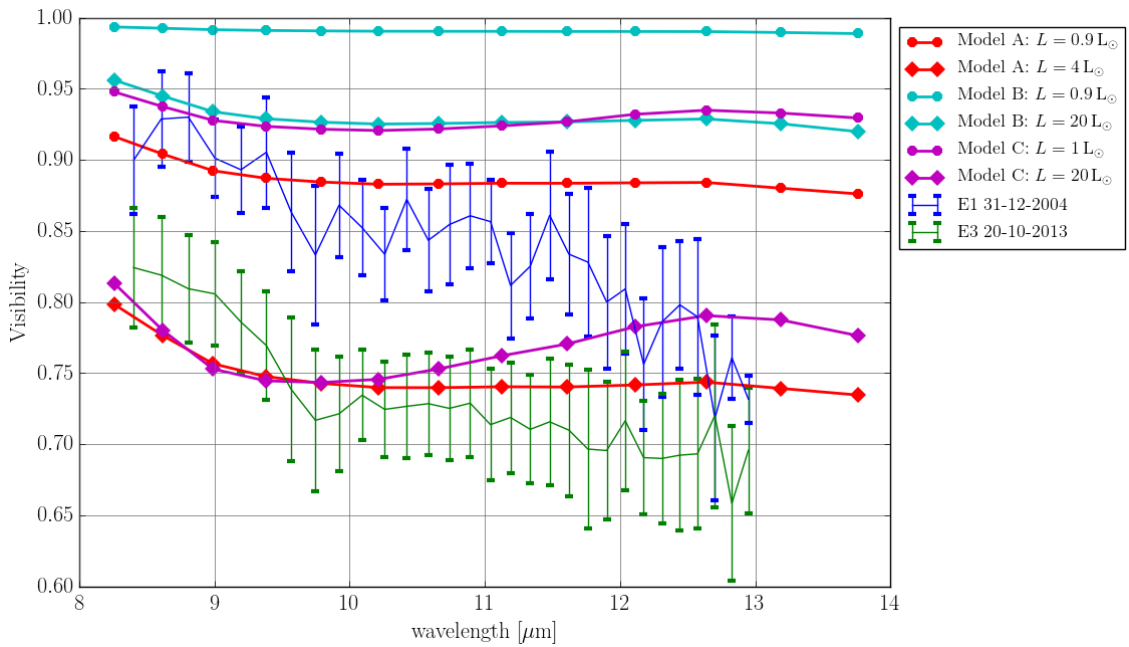
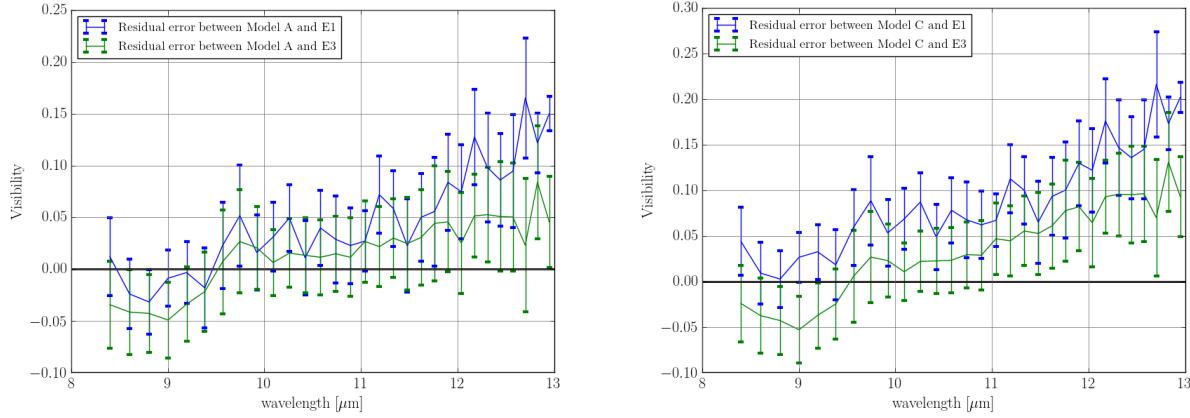


**Figure 4.3.:** Visibility against wavelength for DR Tau data and models. The errorbars for the observational epochs are included, the lower luminosity is marked with circles, and the higher luminosity with diamonds for each model.

Epoch	Model A	Model B	Model C
E1 31-12-2004	0.0049	0.0264	0.0113
E3 20-10-2013	0.0013	0.0412	0.0036

**Table 4.3.:** Mean squared error



**(a)** Residual in visibility for Model A against both E1 and E3

**(b)** Residual in visibility for Model C against both E1 and E3

**Figure 4.4.: Residual errors**

## 4.5. Discussion

If a better fit (within error) for the observational data in epoch E1 was found, an increase in luminosity of less than  $1 - 2$  magnitudes (in the interval  $1 L_{\odot}$  to  $50 L_{\odot}$ ) is sufficient to explain the change in visibility for epoch E3, while keeping more or less the overall shape of the visibility curve. Without running the simulations for such a model this cannot be proved.

Other parameters could intrinsically explain the change in visibility, such as dust size composition and porosity. The disk model itself could prove to be not necessarily a circularly symmetric dense disk, without any holes, blobs or other irregularities.

# Chapter 5.

## Conclusion

The stellar variability in luminosity and even temperature is found to influence the observational appearance of protoplanetary disks by changing the values of the observed visibilitites. The change in luminosity in the parameter space explored [ $1 - 50L_{\odot}$ ] is found to be of greatest influence in the MIR, and have little to no consequence in the NIR, where the maximum variance observed is of 3.82%. The maximum variance caused by a change in luminosity is of 48.1% for a circumstellar disk with  $T_{\star} = 5\,000\text{ K}$ ,  $R_{\text{in}} = 0.1\text{ AU}$  at  $\lambda = 13.76\text{ }\mu\text{m}$  with a fifty time luminosity increase. The most important results are found in Table 3.4, reflecting the maximum and average variance with maximum luminosity variability. The results also reflect that the variance is dependent on the geometry of the disk, in particular the inner radius  $R_{\text{in}}$ .

Knowing the inner radius of the disk  $R_{\text{in}}$ , one could, with sufficient simulation results collected in the inner radius - luminosity space, determine (with a certain inaccuracy) the luminosity change required for a given average drop in the visibility in the MIR. The smaller the inner radius, the larger the impact on the visibility, as it is the Fourier Space representation of the object.

Considering a star fixed in radius and varying the luminosity by means of temperature proves efficient in variations of the observable appearance of disks, with a maximum variation in visibility of 30%. The maximum variance obtained with temperature alone is of 28.5%. Variations in the effective temperature of a pre-main-sequence are estimated from observations to the range 7 – 11% [20], and so are highly unlikely to result in a considerable variance in the visibility.

Though unable to fit the data for DR Tau, the results are promising in showing the same change in visibility. Model A [10] is an approximate fit, which shows a similar

drop in visibility with a change in luminosity of 1,62 magnitudes, having a summed mean error of 0.08 for both data sets. The luminosity variability of the central star can be considered as an candidate to explain the changes in visibility of the system they form with their protoplanetary disks.

The baselines investigated are always 0 – 200 m as this is the maximum baseline achieved by the instruments of interest at present. All results outside this baseline, though interesting, are unable to be observed and were not considered for investigation.

Depending on the geometry of the object, the baseline of the interferometer, the wavelength observed and the magnitude of the luminosity change, the latter can be observed and measured through the variations in visibility, taking into account the measuring error of present instruments (VLTI/MATISSE).

# Appendix A.

## Data and constants

**Table A.1.: Infra red bands**

Band	$\lambda [\mu\text{m}]$
J	1.1 – 1.4
H	1.5 – 1.8
K	2.0 – 2.4
L	3.0 – 4.0
M	4.6 – 5.0
N	7.5 – 14.5

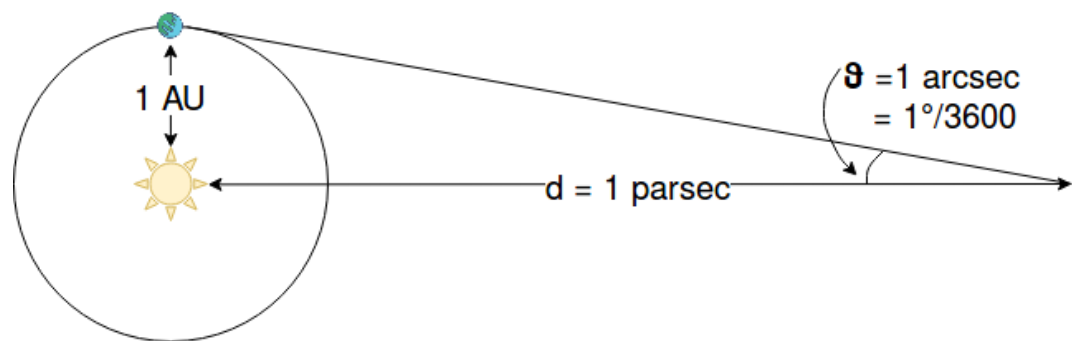


**Figure A.1.:** A parsec [pc] is defined as distance at which the angle subtended by  $x = 1 \text{ AU}$  is an arcsec.  $1 \text{ arcsec} = \frac{1}{3600}^\circ = \frac{2\pi}{1296000} \text{ rad}$ .  $1 \text{ pc} = 3.26 \text{ ly} = 206264.8 \text{ AU} \approx 3 \cdot 10^{16} \text{ m}$

**Table A.2.:** Astrophysical constants

Constant	Name	Value
$M_{\odot}$	Solar Mass	$1.989 \times 10^{30}$ kg
$R_{\odot}$	Solar radius	$6.96 \times 10^8$ m
$L_{\odot}$	Solar luminosity	$3.827 \times 10^{26}$ J s <sup>-1</sup>
$M_{\oplus}$	Earth Mass	$5.976 \times 10^{24}$ kg
1 ly	light year	$9.461 \times 10^{15}$ m
1 AU	Astronomical Unit	$1.496 \times 10^{11}$ m
1 pc	Parsec	$3.086 \times 10^{16}$ m
c	Speed of light in vacuo	$2.998 \times 10^8$ m s <sup>-1</sup>
1 Jy	Jansky	$10^{-26}$ W m <sup>-2</sup> · Hz <sup>-1</sup>
h	Planck's constant	$6.626 \times 10^{-34}$ J s
k	Boltzmann's constant	$1.381 \times 10^{-23}$ J K <sup>-1</sup>
$\sigma$	Stefan-Boltzmann constant	$5.670 \times 10^{-8}$ J m <sup>-2</sup> K <sup>-4</sup> s <sup>-1</sup>

**Table A.3.:** Acronyms

AT	Auxiliary Telescope
CTTS	Classical T Tauri Stars
ESO	European Southern Observatory
HAEBE	Herbig Ae/Be
IR	infrared
ISM	Interstellar medium
MIR	mid infrared
NIR	near infrared
PMS	pre-main sequence
TT	T Tauri
UT	Unit Telescope
VLT	Very Large Telescope
VLTI	Very Large Telescope interferometer
WTTS	Weak-lined T Tauri Stars
YETI	The Young Exoplanet Transit Initiative
YSO	Young stellar object

**Table A.4.:** T Tauri typical parameters extracted from Table 1 in [33]

Star name	Type	distance $d$ [pc]	$T_{\text{eff}}$ [K]	$L$ [ $L_{\odot}$ ]	$L_{\text{min}}$ [ $L_{\odot}$ ]	$L_{\text{max}}$ [ $L_{\odot}$ ]
LkHalpha330	T Tauri	250	5800	11	7	16
RYTau	T Tauri\Herbig Ae/Be	142	6310	15	9	23
LkCa16	T Tauri	142	4350	0.8	0.6	1
DRTau	T Tauri	142	4060	1.1	0.9	1.3
GMAur	T Tauri	142	4730	1.2	0.8	1.6
SU Aur	T Tauri\Herbig Ae/Be	146	5860	11	3	19
CRCha	T Tauri	160	4900	3	2.3	3.8
DICha	T Tauri	160	5860	9.5	7.3	11.7
HPCha	T Tauri	160	4205	3.2	1.7	7.7
FMCha	T Tauri	160	4350	5.8	3.5	6.9
WWCha	T Tauri	160	4350	6.5	4.2	10.2
CVCha	T Tauri	160	5410	4.6	3.6	5.7
TCha	T Tauri	108	5890	1.2	0.5	3.1
HD142560	T Tauri	150	4000	3.7	2.2	5.6
HD143006	T Tauri	145	5884	3.4	2.7	4.2
V2246OPH	T Tauri	120	5248	7.5	6.3	9.5
HBC639	T Tauri	120	5250	8.1	4.8	11.8
ELIAS2-24	T Tauri	120	4266	1.8	1.1	2
ELIAS2-28	T Tauri	120	4169	0.3	0.2	0.6
ELIAS2-30	T Tauri	120	5950	6.3	3.3	11.9
V2129OPH	T Tauri	120	3981	1.3	0.8	1.7
V2062OPH	T Tauri	120	4900	1.5	1	2.1

# Appendix B.

## Algorithm

*mol3d* is in essence a Monte Carlo Radiative Transfer simulation programme. It requires first the exact geometry, position and parameter values for any sources and the density and distribution of surrounding dust or molecules. It then initializes a number  $N_{\text{ph}}$  of photon packets from each source (in this case the central star and, if needed, an additional accretion source). The energy of the source is distributed equally to all the photon packets and the setup is assumed to be in thermal equilibrium. As a photon packet is initialised, it is assigned a frequency such that the distribution of frequencies in the end matches the Planck distribution corresponding to the effective temperature of the star,  $T_*$ . Next, the photon packet is assigned, through random number sampling, an optical depth,  $\tau_\nu$ , which it should penetrate, and a random direction of travel. The photon packet is assumed to travel in the direction of travel until the optical depth is reached. Here an interaction must occur: scattering or absorption (followed by immediate re-emission by the dust in the cell, according to the new temperature profile reached through absorption).

This concludes one step and after scattering or absorption the photon packet is assigned a new frequency, optical depth and direction to travel. The photon packet is terminated if: the maximum number of interactions ( $N_{i,\text{max}}$ ) is reached or if the edge of the model space is reached. When a photon packet is terminated a new photon packet from the source is initialized until all the photon packets  $N_{\text{ph}}$  have been terminated. At the end of the simulation the temperature map of the system is obtained.

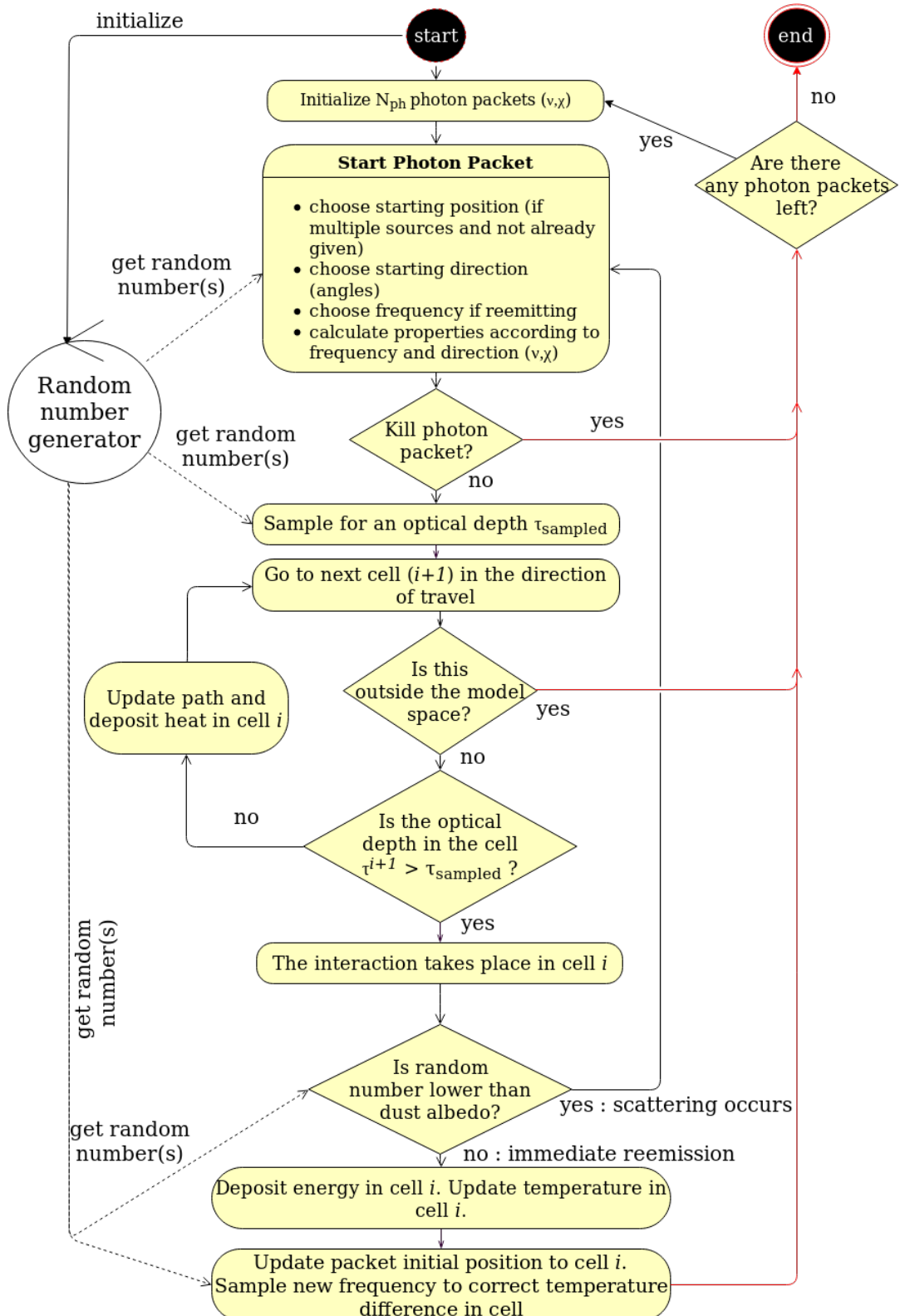


Figure B.1.: Code Implementation Diagram

## B.1. Code

In order to reproduce the simulations, *mol3d*, which can be found at <https://github.com/florianober/Mol3D> [36], needs to be downloaded and compiled. To use the density distribution (or change density distributions parameters) the file *src/model\_mod.f90*, line 71 was modified according to equation (2.24). The program needs to be compiled after modification (the visibility calculation function includes the numpy library Fast Fourier Transform).

For the purpose of running the simulations and analysing the data a small library of functions was written, out of which the most important are included below:

```
#util/common.py
from util.constants import *
import util.util as u
import matplotlib.pyplot as plt
import numpy as np
import os
import math as m
import shutil
from astropy.io import fits

def run_simulation(
    star_name,
    star_temperature,
    star_radius,
    star_distance,
    simulation_name,
    run_temperature=True,
    run_rm=True,
    run_visibility=True,
    i_wlen=wavelengths_index,
    wlen=wavelengths,
    params={}
):
    star_input = root_dir + 'input/input_' + simulation_name + '.dat'
```

```
shutil.copyfile(input_file, star_input)
project_name = simulation_name + '_temp_n'

if run_temperature:
    # Temperature simulation
    u.replace(star_input, 'proname', project_name)
    u.replace(star_input, 'T_star', star_temperature)
    u.replace(star_input, 'R_star', star_radius)
    u.replace(star_input, 'distance', star_distance)
    for key, value in params.items():
        u.replace(star_input, key, value)
    os.system(root_dir + "mol3d " + star_input)

if run_rm:
    # Continuum simulation
    u.replace(star_input, 'proname', simulation_name + '_mono')
    u.replace(star_input, 'old_model', 'T')
    u.replace(star_input, 'do_MC_temperature', 'F')
    u.replace(star_input, 'old_proname', project_name)
    u.replace(star_input, 'do_continuum_mono', 'T')
    u.replace(star_input, 'do_continuum_raytrace', 'T')
    os.system(root_dir + "mol3d " + star_input)

if run_visibility:
    # Calculate visibility
    r_ou = 20 #with zoom =10
    map_rad = np.arctan((r_ou * m.pi)/(star_distance * 648000))
    calculate_visibility(simulation_name, i_wlen, wlen, star_name,
    os.system('rm ' + star_input)

def calculate_visibility(simulation_name, i_wlen, wlen, star_name, map_
# Visibility calculation
mono_file = fits.open(results_dir + simulation_name +
    '_mono_continuum_map_mono.fits.gz')
```

```

raytrace_file = fits.open(results_dir + simulation_name +
                          '_mono_continuum_map_raytrace.fits.gz')
data_mono = mono_file[0].data[0][i_wlen]
data_raytrace = raytrace_file[0].data[0][i_wlen]
mono_file.close()
raytrace_file.close()

data = data_mono + data_raytrace
if (not os.path.isfile(results_dir + simulation_name +
                      '_mono_continuum_map_total.fits.gz')):
    hdu = fits.PrimaryHDU(data)
    hdul = fits.HDUList([hdu])
    hdul.writeto(results_dir + simulation_name +
                 '_mono_continuum_map_total.fits.gz')

del data_raytrace
del data_mono

dir = u.make_dir(visibility_dir, star_name)

filename = dir + 'visibilities_' + simulation_name + star_name + '.csv'
with open(filename, 'w') as fd:
    writer = csv.writer(fd, delimiter=",", lineterminator='\n')
    writer.writerow(np.concatenate([[['baseline']], wlen]))
    writer.writerow(np.concatenate([[0], [1] * len(wlen)]))
    for i in range(5, 205, 5):
        visibility, phases, maps = it.get_visibility_2D(
            np.array([0]),
            np.array([i]),
            wlen,
            data,
            map_rad
        )
        writer.writerow(np.concatenate([[i], visibility[:, 0]]))

del data

```

# Appendix C.

## Theoretical Supplement

### C.1. Stellar Spectra

Most of the important information about the physical properties of stars come from studies of their spectra [22]. By means of dispersing the incoming light from stars we can observe their spectra and compare it to the spectra of known elements (e.g. that of hydrogen in Figure 2.3d).

The spectral classification scheme used at present is called the Harvard classification, as it was developed at the Harvard Observatory at the beginning of the 20<sup>th</sup> century by Annie Jump Cannon, and published in the Henry Draper Catalogue. The classification is based on lines that are mainly sensitive to the stellar temperature, such as the hydrogen Balmer lines, the lines of neutral helium, the iron lines and others mentioned in Table C.1.

The spectral types were denoted alphabetically with a capital letter. Subsequently, in order of decreasing temperature, the classification became

$$\begin{array}{c} \text{C} \\ \text{O-B-A-F-G-K-M-L-T} \\ \text{S} \end{array}$$

with some additional notations (Q for novae, P for planetary nebulae and W for Wolf-Rayet stars). The spectral classes C and S represent parallel branches to types G–M, differing in their surface chemical composition. The most recent addition are the spectral classes L and T continuing the sequence beyond M, representing brown

dwarfs. The spectral classes are divided into subclasses denoted by the numbers  $\overline{0..9}$ , with decimals sometimes being used.

Type	Prominent Spectral Lines	Colour	Temperature
O	$\text{He}^+$ , He, H, $\text{O}^{2+}$ , $\text{N}^{2+}$ , $\text{C}^{2+}$ , $\text{Si}^{2+}$	Blue	 $\sim 30\,000 \text{ K}$
B	He, H, $\text{C}^+$ , $\text{O}^+$ , $\text{N}^+$ , $\text{Fe}^{2+}$ , $\text{Mg}^{2+}$	Blue-white	 $15\,000 \text{ K}$
A	He, ionised metals	White	 $9\,000 \text{ K}$
F	H, $\text{Ca}^+$ , $\text{Ti}^+$ , $\text{Fe}^+$	Yellow-white	 $7\,000 \text{ K}$
G	$\text{Ca}^+$ , Fe, Ti, Mg, H, some molecular bands	Yellow	 $5\,500 \text{ K}$
K	$\text{Ca}^+$ , H, molecular bands	Orange	 $4\,000 \text{ K}$
M	TiO, Ca, molecular bands	Red	 $\sim 3\,000 \text{ K}$

**Table C.1.:** Spectral stellar types

An alternative to the Harvard classification, which only takes into account the effect of temperature on the spectrum, is the Yerkes or MKK classification, which takes into account the luminosity of the stars (even for the same effective temperature), determined from spectral lines that strongly depend on the stellar surface gravity, which is closely related to the luminosity. Six different luminosity classes are distinguished, denoted by Roman numerals (the Sun is G2 V):

- Ia most luminous supergiants
- Ib less luminous supergiants
- II luminous giants
- III normal giants
- IV subgiants
- V main sequence stars (dwarfs)

## C.2. T Tauri classification

T Tauri stars are defined by the appearance of their spectrum [38]:

- the Balmer and Ca II H and K lines in emission;
- Fe  $\lambda 4063$  and  $4132$  in emission;
- forbidden S II  $\lambda 4068$  and  $4076$  lines, usually in emission;

- Li $\lambda$ 6707 strong.

Some of these features are associated with the star's youth and others with accretion and the activity of the star. The presence of Li lines in the spectrum, indicate an abundance at least 100 times of that in the Sun – an indicator of youth, as circulations currents in a fusing star mix the lithium to deeper layers [38].

### C.3. HR Diagram

The relation between the stellar properties of luminosity, effective temperature (or spectral type) and radius were studied by the physicists Ejnar Hertzsprung and Henry Russell at the beginning of the 20<sup>th</sup> century. Their studies produced a very important aid in studies of stellar evolution, the Hertzsprung-Russell Diagram, or simply HR diagram (Figure C.1). One might have expected a uniform distribution of temperatures and luminosities, but it is found that most stars lie on the Main Sequence – the diagonal going from upper left to lower right. On the other diagonal, from lower left to upper right, the radii of the star increase (in accordance to equation 2.21). It is notable as well that the yellow and red stars (spectral types G–K–M) appear to be clustered into either the dwarf stars of the main sequence or the giants. The supergiants have an almost horizontal sequence, while the red giant branch rises from the main sequence around the temperature mark of the Sun. Below the main sequence, there is the group of white dwarfs, which are quite faint and difficult to observe.

Protostars enter the main sequence as their radius decreases and their temperature increases. In the main sequence stars are most stable, but they will eventually exhaust all the hydrogen. When this happens, the star leaves the main sequence and, depending on their mass, they have various destinies. Low mass stars ( $\sim 0.5M_{\odot}$ ) will not have sufficient gravity to heat the core to high enough temperatures and pressures for fusing helium. They will cool down and become Red Dwarfs, like *AB Doradus C* in Figure C.1. *AB Dor C* has a temperature of about 3000K and a luminosity which is 0.2% that of the Sun and it will never leave the main sequence. Stars similar to the Sun will expand and shed their exterior layers, as they run out of hydrogen, they will then collapse again before burning their Helium reserves and become a Red Giant before collapsing again into a White Dwarf. Bigger stars will expand to Super Giants, fusing more heavy elements. They will end their lives most spectacularly with a supernova,

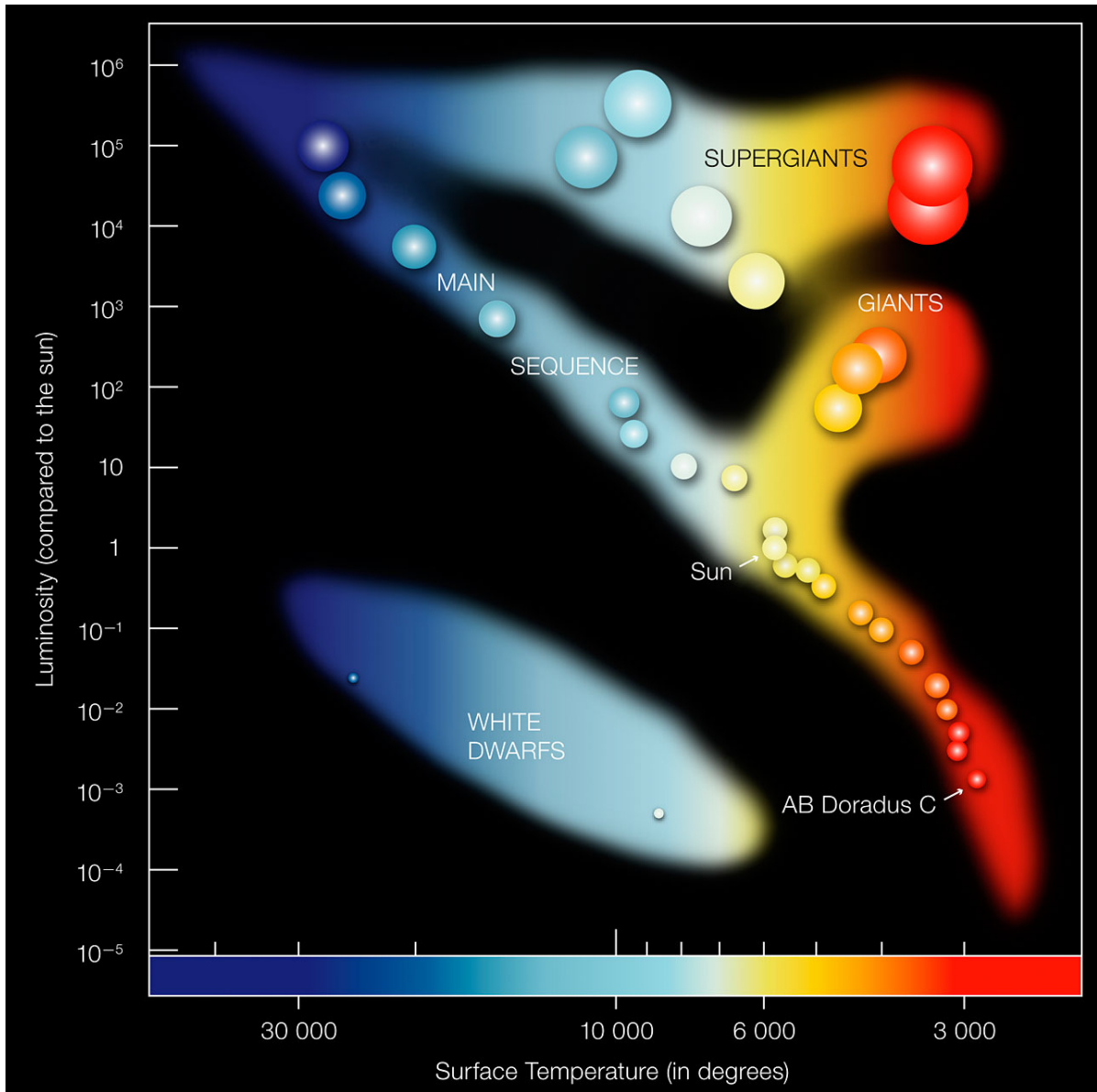


**Figure C.1.: Herzsprung-Russell Diagram:** In the Hertzprung-Russell diagram the temperatures of stars are plotted against their luminosities. The position of a star in the diagram provides information about its present stage and its mass. Stars that burn hydrogen into helium lie on the diagonal main sequence. The Sun is situated about the middle of the main sequence. **Credit:**ESO

which will leave behind a neutron star for a star with more than  $1.4M_{\odot}$  or a black hole for stars with a mass of more than  $3M_{\odot}$  [40].

## C.4. Variabile stars

Technically, all stars are variable, given that their structure and brightness change as they evolve. Although the changes are usually slow, some evolutionary phases can be extremely rapid, or may present periodic variations, for example pulsations of the outer layers of a star. Small variations in stellar brightness are also caused by dark or light spots on a star's surface, as it rotates about its axis. The magnitude variation as a function of time is called the lightcurve of a star (Figure C.2). From this the amplitude and period of the variation can be determined, if periodic.

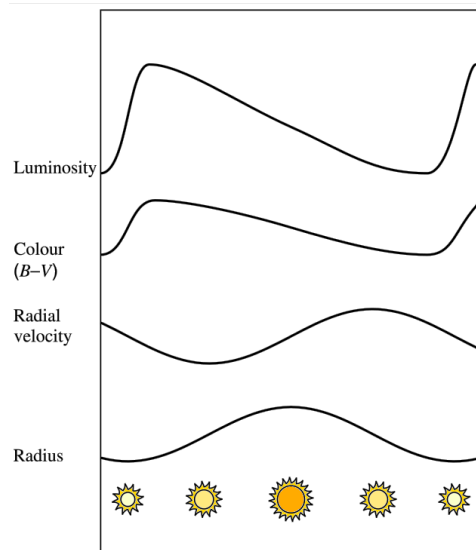


**Figure C.2.:** Variation of brightness, colour and size of a Cepheid<sup>20</sup> during its pulsation. The uppermost curve, describing luminosity is called the lightcurve. **Credit:** Adapted from [22]

Variables are classified based on the shape of their lightcurve, the spectral class and the observed motions in mainly three categories: pulsating, eruptive and eclipsing variables. A pulsating variable is an intrinsic variable, whose exterior layers are dilating and contracting, trying to reach an equilibrium between the gravitational force pushing inwards and the gas pressure pushing outwards. In the case of many pulsating variables (including Cepheid<sup>20</sup>) the period of variation of the star is proportional to its luminosity. The diameter may double during the pulsation, but usually the main cause of light variation is the periodic variation of surface temperature. As seen in equation

<sup>20</sup>Among the most important pulsating variables are the **cepheids**, named after  $\delta$  *Cephei*. They are supergiants of spectral class F–K, with periods of 1–50 days and amplitudes of 0.1–2.5 magnitudes in their variability

(2.21)  $L \propto T_e^4$  and a small change in effective temperature leads to a large brightness variation. Stars with surface temperatures of 6000–9000 K are liable to this instability and the corresponding section of the HR diagram is called the Cepheid instability strip. There are various pulsating variable stars with periods up to 500 days.

The eruptive variables exhibit instead of a regular pulsation a sudden outburst in which material is ejected into space. These star are usually surrounded by a gas shell or interstellar matter.

The third category is the eclipsing variables. As the name suggests, these are usually binary systems in which the components periodically pass in front of each other. The variability is not related to any physical change in the star, and is apparent. In addition, a few rotating variables with an uneven distribution of temperature on the surface are known. They have periods of about 1 to 25 days and the changes are small, less than 0.1 magnitudes.





# Bibliography

- 1 ALEXANDER, C. ; BOSS, A. ; KELLER, L. ; NUTH, J. ; WEINBERGER, A. : Astronomical and meteoritic evidence for the nature of interstellar dust and its processing in protoplanetary disks. In: *Protostars and planets V* (2007), S. 801–813
- 2 ANDREWS, S. M. ; WILLIAMS, J. P.: Circumstellar Dust Disks in Taurus-Auriga: The Submillimeter Perspective. In: *The Astrophysical Journal* 631 (2005), oct, Nr. 2, 1134–1160. <http://dx.doi.org/10.1086/432712>. – DOI 10.1086/432712
- 3 ANDREWS, S. M. ; WILNER, D. J. ; HUGHES, A. M. ; QI, C. ; DULLEMOND, C. P.: PROTOPLANETARY DISK STRUCTURES IN OPHIUCHUS. II. EXTENSION TO FAINTER SOURCES. In: *The Astrophysical Journal* 723 (2010), oct, Nr. 2, 1241–1254. <http://dx.doi.org/10.1088/0004-637x/723/2/1241>. – DOI 10.1088/0004-637x/723/2/1241
- 4 BASTIAN, U. ; FINKENZELLER, U. ; JASCHEK, C. ; JASCHEK, M. : The definition of T Tauri and Herbig Ae/Be stars. In: *ap* 126 (1983), Okt., S. 438
- 5 BATE, M. R.: On the diversity and statistical properties of protostellar discs. In: *Monthly Notices of the Royal Astronomical Society* 475 (2018), 01, Nr. 4, 5618–5658. <http://dx.doi.org/10.1093/mnras/sty169>. – DOI 10.1093/mnras/sty169. – ISSN 0035–8711
- 6 BECKWITH, S. V. W.: Circumstellar Disks. In: LADA, C. J. (Hrsg.) ; KYLAFIS, N. D. (Hrsg.): *NATO Advanced Science Institutes (ASI) Series C* Bd. 540, 1999 (NATO Advanced Science Institutes (ASI) Series C), S. 579
- 7 BERISTAIN, G. ; EDWARDS, S. ; KWAN, J. : Permitted Iron Emission Lines in the Classical T Tauri Star DR Tauri. In: *The Astrophysical Journal* 499 (1998), jun, Nr. 2, 828–852. <http://dx.doi.org/10.1086/305675>. – DOI 10.1086/305675
- 8 BJORKMAN, J. ; WOOD, K. : Radiative Equilibrium and Temperature Correction in Monte Carlo Radiation Transfer. In: *The Astrophysical Journal* 554 (2001), 06, S.

615–623

- 9 BODENHEIMER, P. H.: *Principles of Star Formation*. Springer, 2011. – ISBN 978–3–642–15062–3
- 10 BRUNNGRÄBER, R. : *Beobachtbarkeit von ausgewählten Strukturen und Staubeigenschaften zirkumstellarer Scheiben in verschiedenen Entwicklungsstadien*. Version: 04 2018. [https://macau.uni-kiel.de/receive/dissertation\\_diss\\_00022969](https://macau.uni-kiel.de/receive/dissertation_diss_00022969)
- 11 COHEN, MARTIN AND EMERSON, J. P. AND BEICHMAN, C. A.: A reexamination of luminosity sources in T Tauri stars. I - Taurus-Auriga. In: *Astrophysical Journal* 339 (1989), S. 455–473
- 12 FERNÁNDEZ-ONTIVEROS, J. A. ; TRISTRAM, K. R. W. ; HÖNIG, S. ; GANDHI, P. ; WEIGELT, G. : Embedded AGN and star formation in the central 80 pc of IC 3639. In: *Astronomy & Astrophysics* 611 (2018), März, S. A46. <http://dx.doi.org/10.1051/0004-6361/201731906> – DOI 10.1051/0004–6361/201731906
- 13 FIXSEN, D. J.: The Temperature of the Cosmic Microwave Background. In: *The Astrophysical Journal* 707 (2009), Nr. 2, 916. <http://stacks.iop.org/0004-637X/707/i=2/a=916>
- 14 GHEZ, A. M. ; NEUGEBAUER, G. ; MATTHEWS, K. : The multiplicity of T Tauri stars in the star forming regions Taurus-Auriga and Ophiuchus-Scorpius: A 2.2 micron speckle imaging survey. In: *The Astronomical Journal* 106 (1993), Nov., S. 2005–2023. <http://dx.doi.org/10.1086/116782> – DOI 10.1086/116782
- 15 GOODMAN, J. W.: *Statistical Optics*. Wiley-Interscience <https://www.amazon.com/Statistical-Optics-Joseph-W-Goodman/dp/0471399167?SubscriptionId=AKIAIOBINVZYXZQZ2U3A&tag=chimborio5-20&linkCode=xm2&camp=2025&creative=165953&creativeASIN=0471399167>. – ISBN 0471399167
- 16 GREAVES, J. S.: Dense gas discs around T Tauri stars. In: *Monthly Notices of the Royal Astronomical Society* 351 (2004), 07, Nr. 4, L99-L104. <http://dx.doi.org/10.1111/j.1365-2966.2004.08066.x>. – DOI 10.1111/j.1365–2966.2004.08066.x. – ISSN 0035–8711
- 17 GREENE, T. P.: Protostars. In: *American Scientist* 89 (2001), S. 316–325
- 18 HARTMANN, L. ; KENYON, S. J.: On the nature of FU Orionis objects. In: *The Astrophysical Journal* 299 (1985), Dez., S. 462–478. <http://dx.doi.org/10.1086/313500>

163713. – DOI 10.1086/163713
- 19** HERBST, W. ; HERBST, D. K. ; GROSSMAN, E. J. ; WEINSTEIN, D. : Catalogue of UVBRI photometry of T Tauri stars and analysis of the causes of their variability. In: *The Astronomical Journal* 108 (1994), Nov., S. 1906–1923. <http://dx.doi.org/10.1086/117204>. – DOI 10.1086/117204
- 20** HESSMAN, F. V. ; GUENTHER, E. W.: The highly veiled T Tauri stars DG Tau, DR Tau, and DI Cep. In: *Astronomy & Astrophysics* 321 (1997), Mai, S. 497–512
- 21** JAMES, J. F.: *A Student's Guide to Fourier Transforms: With Applications in Physics and Engineering (Student's Guides)*. Cambridge University Press <https://www.amazon.com/Students-Guide-Fourier-Transforms-Applications/dp/0521176832?SubscriptionId=AKIAIOBINVZYXZQZ2U3A&tag=chimbori05-20&linkCode=xm2&camp=2025&creative=165953&creativeASIN=0521176832>. – ISBN 0521176832
- 22** KARTTUNEN, H. ; KRÖGER, P. ; OJA, H. ; POUTANEN, M. ; DONNER, K. J.: *Fundamental Astronomy*. 6. Springer, 2017. <http://dx.doi.org/https://doi.org/10.1007/978-3-662-53045-0>. <http://dx.doi.org/https://doi.org/10.1007/978-3-662-53045-0>. – ISBN 978–3–662–53044–3
- 23** KENYON, S. J. ; DOBRZYCKA, D. ; HARTMANN, L. : A new optical extinction law and distance estimate for the Taurus-Auriga molecular cloud. In: *The Astronomical Journal* 108 (1994), Nov., S. 1872–1880. <http://dx.doi.org/10.1086/117200>. – DOI 10.1086/117200
- 24** KENYON, S. J. ; HARTMANN, L. : Pre-Main-Sequence Evolution in the Taurus-Auriga Molecular Cloud. In: *The Astrophysical Journal, Supplement* 101 (1995), Nov., S. 117. <http://dx.doi.org/10.1086/192235>. – DOI 10.1086/192235
- 25** KIRCHSCHLAGER, F. ; WOLF, S. ; KRIVOV, A. V. ; MUTSCHKE, H. ; BRUNNGRÄBER, R. : Constraints on the structure of hot exozodiacal dust belts. In: *Monthly Notices of the Royal Astronomical Society* 467 (2017), Mai, S. 1614–1626. <http://dx.doi.org/10.1093/mnras/stx202>. – DOI 10.1093/mnras/stx202
- 26** LAWSON, P. R. (Hrsg.): *Principles of Long Baseline Stellar Interferometry*. 2000
- 27** LEINERT, C. ; GRASER, U. ; PRZYGODDA, F. ; WATERS, L. ; PERRIN, G. ; JAFFE, W. ; LOPEZ, B. ; BAKKER, E. ; BÖHM, A. ; CHESNEAU, O. ; COTTON, W. ; DAMSTRA, S. ; JONG, J. de ; GLAZENBORG-KLUTTIG, A. ; GRIMM, B. ; HANENBURG, H. ; LAUN,

- W. ; LENZEN, R. ; LIGORI, S. ; MATHAR, R. ; MEISNER, J. ; MOREL, S. ; MORR, W. ; NEUMANN, U. ; PEL, J.-W. ; SCHULLER, P. ; ROHLOFF, R.-R. ; STECKLUM, B. ; STORZ, C. ; LÜHE, O. von d. ; WAGNER, K. : MIDI – the 10  $\mu\text{m}$  instrument on the VLTI. In: *Astrophysics and Space Science* 286 (2003), Nr. 1/2, 73–83. <http://dx.doi.org/10.1023/a:1026158127732>. – DOI 10.1023/a:1026158127732
- 28 LING, S. J. ; SANNY, J. ; MOEBS, B. : *University Physics*. [https://phys.libretexts.org/Bookshelves/University\\_Physics/Book%3A\\_University\\_Physics\\_\(OpenStax\)](https://phys.libretexts.org/Bookshelves/University_Physics/Book%3A_University_Physics_(OpenStax)). Version: 2018
- 29 LOINARD, L. ; TORRES, R. M. ; MIODUSZEWSKI, A. J. ; RODRIGUEZ, L. F. ; GONZALEZ-LOPEZLIRA, R. A. ; LACHAUME, R. ; VAZQUEZ, V. ; GONZALEZ, E. : VLBA Determination of the Distance to Nearby Star-forming Regions. I. The Distance to T Tauri with 0.4% Accuracy. In: *The Astrophysical Journal* 671 (2007), dec, Nr. 1, 546–554. <http://dx.doi.org/10.1086/522493>. – DOI 10.1086/522493
- 30 LORENZETTI, D. ; LARIONOV, V. M. ; GIANNINI, T. ; ARKHAROV, A. A. ; ANTONIUCCI, S. ; NISINI, B. ; PAOLA, A. D.: NEAR-INFRARED SPECTROSCOPIC MONITORING OF EXOR VARIABLES: FIRST RESULTS. 693 (2009), mar, Nr. 2, 1056–1073. <http://dx.doi.org/10.1088/0004-637x/693/2/1056>. – DOI 10.1088/0004-637x/693/2/1056
- 31 LYNDEN-BELL, D. ; PRINGLE, J. E.: The evolution of viscous discs and the origin of the nebular variables. In: *Monthly Notices of the Royal Astronomical Society* 168 (1974), S. 603–637
- 32 MATTER, A. ; LAGARDE, S. ; PETROV, R. G. ; BERIO, P. ; ROBBE-DUBOIS, S. ; LOPEZ, B. ; ANTONELLI, P. ; ALLOUCHE, F. ; CRUZALEBES, P. ; MILLOUR, F. ; BAZIN, G. ; BOURGÈS, L. : MATISSE: specifications and expected performances. In: MALBET, F. (Hrsg.) ; CREECH-EAKMAN, M. J. (Hrsg.) ; TUTHILL, P. G. (Hrsg.): *Optical and Infrared Interferometry and Imaging V*, SPIE
- 33 MENU, J. ; VAN BOEKEL, R. ; HENNING, T. ; LEINERT, C. ; WAELKENS, C. ; WATERS, L. B. F. M.: The structure of disks around intermediate-mass young stars from mid-infrared interferometry. Evidence for a population of group II disks with gaps. In: *Astronomy & Astrophysics* 581 (2015), Sept., S. A107. <http://dx.doi.org/10.1051/0004-6361/201525654>. – DOI 10.1051/0004-6361/201525654
- 34 MILLOUR, F. : *All you ever wanted to know about optical long baseline stellar interferometry, but were too shy to ask your adviser.* <https://hal.archives-ouvertes.fr/>

- fr/hal-00273465. Version: Apr. 2008. – working paper or preprint
- 35** NEUHÄUSER, R. ; ERRMANN, R. ; BERNDT, A. ; MACIEJEWSKI, G. ; TAKAHASHI, H. ; CHEN, W. ; DIMITROV, D. ; PRIBULLA, T. ; NIKOGOSSIAN, E. ; JENSEN, E. ; MARSCHALL, L. ; WU, Z.-Y. ; KELLERER, A. ; WALTER, F. ; BRICEÑO, C. ; CHINI, R. ; FERNANDEZ, M. ; RAETZ, S. ; TORRES, G. ; LATHAM, D. ; QUINN, S. ; NIEDZIELSKI, A. ; BUKOWIECKI, Ł. ; NOWAK, G. ; TOMOV, T. ; TACHIHARA, K. ; HU, S.-L. ; HUNG, L. ; KJURKCHIEVA, D. ; RADEVA, V. ; MIHOV, B. ; SLAVCHEVA-MIHOVA, L. ; BOZHINOVA, I. ; BUDAJ, J. ; VAŇKO, M. ; KUNDRA, E. ; HAMBÁLEK, Ł. ; KRUSHEVSKA, V. ; MOVSESSIAN, T. ; HARUTYUNYAN, H. ; DOWNES, J. ; HERNANDEZ, J. ; HOFFMEISTER, V. ; COHEN, D. ; ABEL, I. ; AHMAD, R. ; CHAPMAN, S. ; ECKERT, S. ; GOODMAN, J. ; GUERARD, A. ; KIM, H. ; KOONTHARANA, A. ; SOKOL, J. ; TRINH, J. ; WANG, Y. ; ZHOU, X. ; REDMER, R. ; KRAMM, U. ; NETTELMANN, N. ; MUGRAUER, M. ; SCHMIDT, J. ; MOUALLA, M. ; GINSKI, C. ; MARKA, C. ; ADAM, C. ; SEELIGER, M. ; BAAR, S. ; ROELL, T. ; SCHMIDT, T. ; TREPL, L. ; EISENBEISS, T. ; FIEDLER, S. ; TETZLAFF, N. ; SCHMIDT, E. ; HOHLE, M. ; KITZE, M. ; CHAKROVA, N. ; GRÄFE, C. ; SCHREYER, K. ; HAMBARYAN, V. ; BROEG, C. ; KOPPENHOEFER, J. ; PANDEY, A. : The Young Exoplanet Transit Initiative (YETI). In: *Astronomische Nachrichten* 332 (2011), jul, Nr. 6, 547–561. <http://dx.doi.org/10.1002/asna.201111573>. – DOI 10.1002/asna.201111573
- 36** OBER, F. ; WOLF, S. ; URIBE, A. ; KLAHR, H. H.: Tracing planet-induced structures in circumstellar disks using molecular lines. In: *Astronomy & Astrophysics* 579 (2015), S. A105. <http://dx.doi.org/http://dx.doi.org/10.1051/0004-6361/201526117>. – DOI <http://dx.doi.org/10.1051/0004-6361/201526117>
- 37** PEEST, C. ; CAMPS, P. ; STALEVSKI, M. ; BAE, M. ; SIEBENMORGEN, R. : Polarization in Monte Carlo radiative transfer and dust scattering polarization signatures of spiral galaxies. In: *Astronomy & Astrophysics* 601 (2017), Mai. <http://dx.doi.org/https://doi.org/10.1051/0004-6361/201630157>. – DOI <https://doi.org/10.1051/0004-6361/201630157>
- 38** PERCY, J. R.: *Understanding Variable Stars*. 2007
- 39** PERCY, J. R. ; GRYC, W. K. ; WONG, J. C. ; HERBST, W. : Self-Correlation Analysis of the Photometric Variability of T Tauri Stars. In: *Publications of the Astronomical Society of the Pacific* 118 (2006), oct, Nr. 848, 1390–1395. <http://dx.doi.org/10.1086/508557>. – DOI 10.1086/508557

- 40** REESE, M. (Hrsg.): *Universe: The Definitive Visual Guide*. DK ADULT, 2005. – ISBN 0756613647
- 41** RICCI, L. ; TESTI, L. ; NATTA, A. ; NERI, R. ; CABRIT, S. ; HERCZEG, G. J.: Dust properties of protoplanetary disks in the Taurus-Auriga star forming region from millimeter wavelengths. In: *Astronomy and Astrophysics* 512 (2010), mar, A15. <http://dx.doi.org/10.1051/0004-6361/200913403>. – DOI 10.1051/0004-6361/200913403
- 42** SALYK, C. ; PONTOPPIDAN, K. M. ; BLAKE, G. A. ; LAHUIS, F. ; DISHOECK, E. F. ; II, N. J. E.: H<sub>2</sub>O and OH Gas in the Terrestrial Planet-forming Zones of Protoplanetary Disks. In: *The Astrophysical Journal* 676 (2008), mar, Nr. 1, L49–L52. <http://dx.doi.org/10.1086/586894>. – DOI 10.1086/586894
- 43** SARGENT, B. A. ; FORREST, W. J. ; TAYRIEN, C. ; MCCLURE, M. K. ; WATSON, D. M. ; SLOAN, G. C. ; LI, A. ; MANOJ, P. ; BOHAC, C. J. ; FURLAN, E. ; KIM, K. H. ; GREEN, J. D.: DUST PROCESSING AND GRAIN GROWTH IN PROTOPLANETARY DISKS IN THE TAURUS-AURIGA STAR-FORMING REGION. 182 (2009), may, Nr. 2, 477–508. <http://dx.doi.org/10.1088/0067-0049/182/2/477>. – DOI 10.1088/0067-0049/182/2/477
- 44** SCHOLZ, A. ; EISLÖFFEL, J. : Rotation and accretion of very low mass objects in the  $\sigma$ Ori cluster. In: *Astronomy & Astrophysics* 419 (2004), apr, Nr. 1, 249–267. <http://dx.doi.org/10.1051/0004-6361:20034022>. – DOI 10.1051/0004-6361:20034022
- 45** SHAKURA, N. ; SUNYAEV, R. : Black holes in binary systems. Observational appearance. In: *Astronomy & Astrophysics* 24 (1973), S. 337–355
- 46** SINGH, R. ; MANI, V. ; VISHWAKARMA, K. : Evaluating Age of Universe by Photometric Analysis of Globular Clusters. 42 (2018), Jul., S. E1.16–26–18
- 47** STROM, KAREN M. AND NEWTON, GOEFFREY AND STROM, STEPHEN E.: A study of the stellar population in the LYND 1641 dark cloud. I - The IRAS catalog sources. In: *Astrophysical Journal Supplement Series* 71 (1989), S. 183–217
- 48** SWAMY, K. : *Physics of Comets*. World Scientific (World Scientific series in astronomy and astrophysics). <https://books.google.ro/books?id=HkZILeY8uk4C>. – ISBN 9789814291118

- 49** VOROBYOV, E. I. ; BASU, S. : VARIABLE PROTOSTELLAR ACCRETION WITH EPISODIC BURSTS. In: *The Astrophysical Journal* 805 (2015), may, Nr. 2, 115. <http://dx.doi.org/10.1088/0004-637x/805/2/115>. – DOI 10.1088/0004-637x/805/2/115
- 50** WEINGARTNER, J. C. ; DRAINE, B. T.: Dust Grain-Size Distributions and Extinction in the Milky Way, Large Magellanic Cloud, and Small Magellanic Cloud. In: *The Astrophysical Journal* 548 (2001), S. 296–309
- 51** WOLF, S. : MC3D-3D continuum radiative transfer, Version 2. In: *Computer Physics Communications* 150 (2003), S. 99–115
- 52** WOLF, S. ; VOSHCHINNIKOV, N. : Mie Scattering by ensembles of particles with very large size parameters. In: *Computer Physics Communications* 162 (2004), S. 113–123
- 53** WOOD, K. ; WHITNEY, B. ; BJORKMAN, J. ; WOLFF, M. : *Introduction to Monte Carlo Radiation Transfer* [www-star.st-and.ac.uk/~kw25/research/montecarlo/book.pdf](http://www-star.st-and.ac.uk/~kw25/research/montecarlo/book.pdf)



# **Selbstständigkeitserklärung**

Ich versichere hiermit, dass ich die vorliegende Arbeit selbstständig verfasst und keine anderen als die angegebenen Quellen und Hilfsmittel benutzt habe.

Rostock, 11.02.2019